Measuring Heat Transfer during Twin Roll Casting of Metals

by

Pedram Mehraram

A thesis
presented to the University of Waterloo
in fulfillment of the
thesis requirement for the degree of
Master of Applied Science
in
Mechanical Engineering

Waterloo, Ontario, Canada, 2010

AUTHOR'S DECLARATION

I hereby declare that I am the sole author of this thesis. This is a true copy of the thesis, including any required final revisions, as accepted by my examiners.

I understand that my thesis may be made electronically available to the public.

Abstract

Accurate knowledge of the heat transfer coefficient during casting (between a molten and/or semi-solid material and the mold) is critical to be able to develop representative mathematical models for casting process such as Twin Roll Casting (TRC). In this project, an experimental apparatus was developed to enable to measurement of the interfacial heat transfer coefficient (HTC) at the interface between a liquid metal as it solidifies against a chill surface.

The experimental apparatus consists of a cylinder and piston surrounded by a heater to melt the metal samples. Pressure can be applied at the top of the piston so that the pressure of the liquid metal at the interface can be varied. The apparatus was instrumented with a number of sensors so that the temperature in both the molten metal and chill surface could be monitored as well as a force sensor so that the interfacial pressure and how it varies during solidification is known. Using the measured temperature time history, the interfacial heat transfer was calculated by using an inverse heat conduction method in conjunction with the known thermo-physical properties of the chill and solidifying metal. The apparatus was tested successfully by using Sn-7.5%Sb-3.5%Cu alloy as the casting metal solidifying against H13 tool steel chill block. In addition, the effect of different values of chill roughness and test metal superheat were investigated on the heat transfer coefficient.

Acknowledgements

I would like to thank a number of people who were influential in my studying as a Master's student at the University of Waterloo. Without their supports, this would not have been possible.

First and foremost, I would like to express my sincere gratitude to my research supervisor, Professor Mary Wells, for her guidance, advice, patience and unique supports throughout the completion of my degree. I had the opportunity to observe and learn an exceptional, complete, and productive approach to research, work, and management, based on focus on quality, respect, and collaboration. As an international student it was a great experience for me to work under her supervision which made it easy for me to adopt with the new environment in Canada. I also want to give special thanks to Mr. Jim Baleshta for his help, suggestions and supports in the different steps of designing and building the experimental apparatus. Jim not only was an experienced design engineer in this project but also was a great friend of me during my studying whom I learnt a lot from him. Without his supports and advises in the past two years, this dissertation would not have been possible.

I wish to thank Professor Kyle Daun for his guidance and suggestions in developing the inverse codes.

I also appreciate the help and supports of Charlie G Boy in machine shop in building the experimental apparatus and Andy Barber for his assistance in my experimens.

Thanks also go to Michael H. Herz, Lab director, John Boldt, Rick Forgett, Fred Bakker, Rob Kraemer, Karl Janzen, Jorge Cruz in the machine shop, Norval Wilhelm in the materials laboratory, Richard Gordon and Eckhard Budziarek in the manufacturing lab, Tom Gawel in the high pressure lab for supporting me during design, building and testing the experimental apparatus.

I also would like to express my thanks to Timothy W. Skszek in Magna, Bob Reinhart in the ThermCraft Company, John M. Lindstrom in Conax Technologies, Rick Dole in Omega Engineering, Pascal Charest and Gregor Babic in Promatek Research Centre for their consultation in different aspects of design and providing necessary materials to build the experimental apparatus.

This work was supported by MagNET (NSERC Magnesium Network). I want to acknowledge the financial support provided by MagNET.

Last but not least, I would like to thank my parents, Zohreh and Mohammad, who have always encouraged me in all my endeavors. My success in achieving my goals is a direct result of your confidence in me. Thank you.

This thesis is dedicated to my parents and Laili for their love, endless support, and encouragement.

Table of Contents

List of Tables

List of Figures

Chapter 1 Introduction

There is much interest in the automobile industry to manufacture parts from magnesium alloys because the weight of the vehicle can be reduced [1]. To date, the use of magnesium in cars has been limited to die castings. Additional weight savings in cars can be attained if magnesium sheet were available at a reasonable cost and with the correct properties. Conventionally, magnesium alloys used in sheet applications, have been produced via conventional processing routes whereby Direct Chill (DC) cast ingots are hot and warm rolled to final sheet products. Using this technology, slabs of magnesium are cast with typical dimensions of 0.3m thick by 1m in cross-section and 2m long. These slabs are then homogenized at high temperatures (i.e. 480°C) for several hours followed by hot rolling on a reversing mill to 5-6 mm thick [2]. The next step is usually to anneal the sheet (typically at 340°C) before each pass in a final finish rolling mill. Typical reductions in the finishing mill are limited to 5-20% which causes many rolling passes and annealing treatments in-between. An alternate processing route which could considerably lower the cost of producing magnesium sheet is to investigate thin strip casting technologies, such as Twin Roll Casting (TRC). Using this technology, enables magnesium alloy strip to be produced directly from the melt with a thickness of 4-8mm, thereby eliminating the need for the costly stages of homogenization, hot rolling, and most of the passes in the final finishing mill. Also from a metallurgical viewpoint, near-rapid solidification achieved through twin-roll casting can allow for the design of new alloys which take advantage of the increasing amount of solute in solid solution, enhanced precipitation nucleation within the matrix and finer distribution of precipitates [2]. A key aspect to the success of this process is to have a thorough scientific understanding of the influence of TRC process parameters (e.g. roll velocity, product thickness, roll material and surface texture) on the evolution of the solidification process and microstructure. In Canada, the ministry of Natural Resources materials laboratory, CANMET, has recently commissioned a laboratory twin roll caster for magnesium.

Although twin roll casters have been used for almost 50 years in the aluminum industry, twin roll casting of magnesium is relatively new. As shown in Figure 1-1, in twin roll casting, molten metal is fed onto water-cooled rolls, where it solidifies as it is rolled. Solidification of the molten metal starts at the point of first metal-roll contact and is completed before the kissing point (point of least roll separation) of the two rollers. A key aspect to the successful

development of twin roll casting of magnesium is the quantitative understanding of the heat transfer which occurs between the rolls.

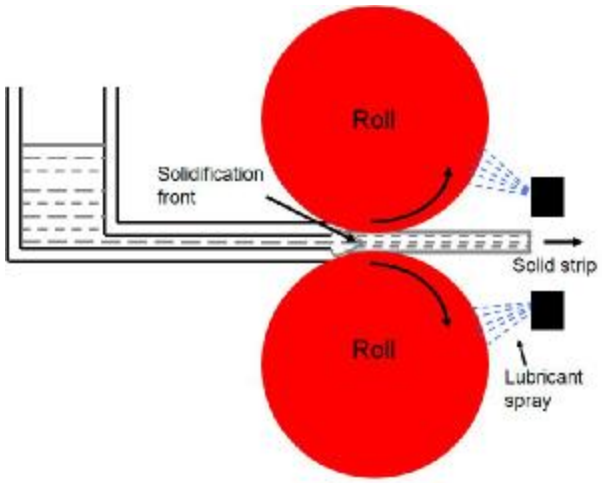

Figure 1-1 Schematic of the horizontal twin roll casting process.

The heat flux from the molten metal to the chill or rolls is controlled by the thermal contact resistance which is identified as the heat transfer coefficient or HTC. This parameter is influenced by many things including: the roughness of the chill/roll surface, superheat of the casting metal and applied pressure on the molten metal.

1.1 Objectives

The objective of this project is to design and build a test apparatus capable of providing knowledge about the heat transfer that occurs between a liquid metal and chill block (roll) during solidification. The effects of parameters such as chill surface roughness and molten metal superheat will also be investigated. The heat transfer coefficient at the interface between the molten metal and chill block will be determined using an Inverse Heat Conduction (IHC) technique based on measurements of the temperature time history in both the molten (cast) part and chill block.

The data obtained from the test apparatus can be used to develop a comprehensive understanding of the heat transfer at the metal mold interface during casting for a range of casting materials and chill or mold materials.

Chapter 2 Literature Review

2.1 Heat Transfer Coefficient during Casting

The heat-transfer coefficient at the metal/mold or metal/roll interface is a very important factor in predicting the solidification rate and final grain structure.

There are different parameters which make modeling heat flux and heat transfer coefficient difficult. One of the most important parameters in modeling of heat transfer coefficient is analyzing the air gap formation and properties of the air gap at the interface of the chill and metal. Considering the different techniques of casting and the dependence of the interface heat transfer on casting geometry, it is can be said that there are so many parameters in the casting process that the experimentally determined heat transfer coefficients can only be employed as a guide in solidification modeling [3]. For this reason, there is a need to investigate the effects of different factors on the heat transfer coefficients at the metal-mold interface individually [4,5].

The mechanisms of metal-mold heat transfer have been detailed by Ho and Pehlke [6,7]. As soon as the molten metal contacts the mold surface or roll surface, a metal-surface interface will be formed.

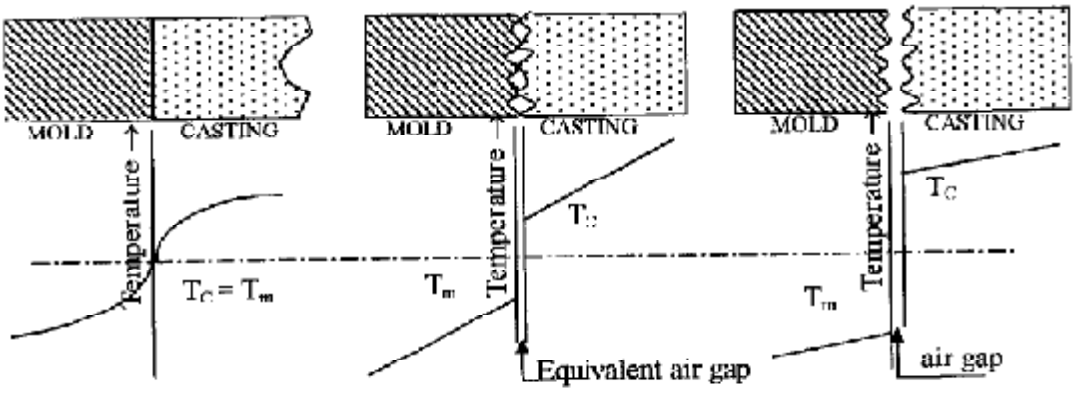

a) Perfect contact b) Some contact c) No contact

Figure 2-1 Casting-Mold Interface Temperature Profiles [8].

However, because of imperfect contact between the surface and solidified metal at the metal/surface interface, this boundary can become the greatest resistance to the heat flow [9]. The contact between the metal and mold or roll surface, as illustrated in Figure 2-1 can be perfect contact, partial contact, or no contact, as in the case where an air gap can form. In the perfect

contact case (Figure 2.1a), there is no discontinuity in temperature profile between the metal/mold interface. Imperfect contact between the metal and the mold can be divided to two parts: the perfect part and the air gap part. Also the presence of oxide films and mold coatings at the metal mold interface can lead to imperfect contact between the mold and the metal. The resistance at the metal/mold boundary, R_T, or more often the heat transfer coefficient h, can be expressed mathematically as:

$$h = \frac{1}{R_T} = \frac{q}{\Delta T} \qquad (2.1)$$

Where h is the heat transfer coefficient $W/(m^2.K)$, q is the heat flux at the interface (W/m^2) and ΔT is the temperature difference across the interface in Kelvin (K).

The heat transfer coefficient values depend mainly on the size and formation of air gap [10].During solidification of the metal, the heat flow rate will change during different stages. In the first stage molten metal is in complete contact with the mold and a small resistance to heat flow can be seen. After that a thin layer of the metal solidifies and because of shrinkage of the material during solidification, small air gap forms between the mold and the solidifying metal. Air gap formation causes an increase in the resistance to the heat flow and decreases the value of the heat transfer coefficient. After solidification of the metal at the metal-mold interface, a complete air gap will be formed. Since heat flow at metal/mold interface occurs by conduction, the forming of an air gap at the interface (with a much lower thermal conductivity than metal) causes a great increase in the heat flow resistance and the heat transfer coefficient will decrease substantially [9,10,11,12,13].

Ho and Pehlke [7], defined these stages of air gap formation and changing in the heat transfer coefficient value at the metal-mold interface as:

- conforming contact,
- non conforming contact, and
- clearance gap.

2.2 Quantifying Heat Transfer

It is difficult or impossible to measure the heat flux and heat transfer coefficient directly. For this reason, inverse methods commonly are employed to estimate these values. These methods can be used to infer a parameter, in case where the parameter is difficult or impossible

to measure directly. Thermal properties of materials or interfacial heat transfer are among the information related to modeling of the materials processing which can be revealed by inverse methods. In castings, the inverse heat conduction problem is applicable in the modeling and calculation of the heat flux or heat transfer coefficient at the metal/mold interface. To employ this method for determination of interfacial heat transfer some information, like the temperature distribution values at one or more points inside the body, need to be obtained [3]. J.V. Beck has developed several inverse solution methods to employ in casting processes [14,15,16,17].

Inverse problems most often do not satisfy Hadamard's requirements of well-posedness: they might not have a solution in the strict sense, solutions might not be unique and/or might not depend continuously on the data. Hence their mathematical analysis is subtle and these problems are described as ill-posed [3].

Li and Wells [18], carried out studies to investigate the effect of thermocouple properties and location during quench operations. By employing a 2-D numerical model it is found that disturbances in the thermal field can lead to predicted higher heat transfer coefficient values when large temperature gradients exist. To solve this problem, the thermocouple location and properties were introduced into the numerical method and a compensation technique developed.

Other authors have investigated of sensitivity of the inverse methods to different parameters like the thermocouple position, noise in the thermocouple reading, thermocouple bias, mold thickness, and mold thermal properties [19,20,21].

2.3 The Influence of Parameters on Heat Transfer

Much research has been conducted to find and measure the effect of different parameters on the heat transfer coefficient at the metal/mold interface during casting of a metal. These works show the heat transfer coefficient values can be influenced by the following factors: air gap formation, forming and thickness of surface coating [22,23,24,25], orientation of casting surface [7,26,27,28,29,30], chill/mold material [7,26,29,31], casting size [25,29,32,33,34], tension of liquid surface [35], superheat [26,31,36,37,38] and chill surface roughness [22,31,36,39,40].

2.3.1 Air Gap Formation

Ho and Pehlke [41], were some of the first researchers to study in detail the heat transfer in casting at the metal/mold interface. They did this using a permanent mold aluminum casting and utilizing Beck's method to solve the nonlinear IHC to model the metal-mold interfacial heat transfer. The experiments were carried out by temperature measurement in top-chilled and bottom chilled castings of both pure aluminum and a Cu-5 wt.% Al casting. They reported that heat flux decreases significantly during the early stages of solidification. They also concluded that the heat transfer is dependent on the interfacial gap size. In later works, they estimated the contact conductance in Al-13 wt.% Si castings by interfacial gap size measurement. The results were consistent with their previous work [42].

El-Mahallawy and Taha [37,43] carried out some HTC research for commercially pure Al, Al-Si alloys, and Al-Cu alloys in which air gap formation was investigated which is shown in Figure 2-2.

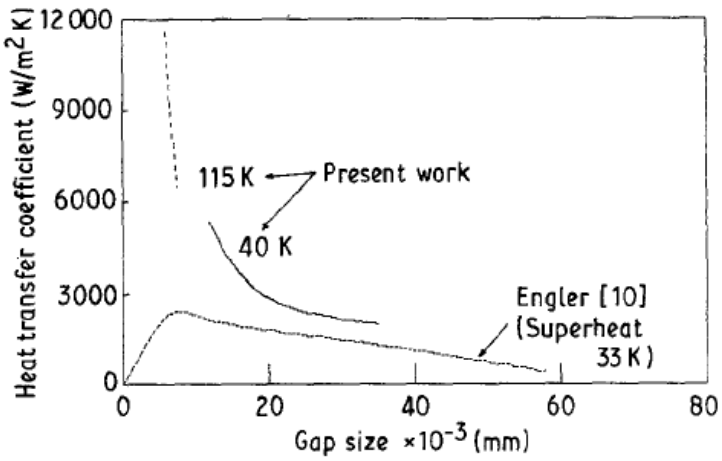

Figure 2-2 Effect of gap size on heat transfer coefficient [37].

Higher HTC values and smaller gap sizes were obtained with higher superheats by Taha et al., in Al and Al-4.5 wt.% Cu cylindrical castings of 12.5 mm diameter and length of either 95 or 230 mm in a vertical end-chill apparatus. Later, the air gap formation and interfacial heat transfer were computed using a numerical model which takes into consideration metal and mold shrinkage and expansion, gas film formation, and the metallostatic pressure [43].

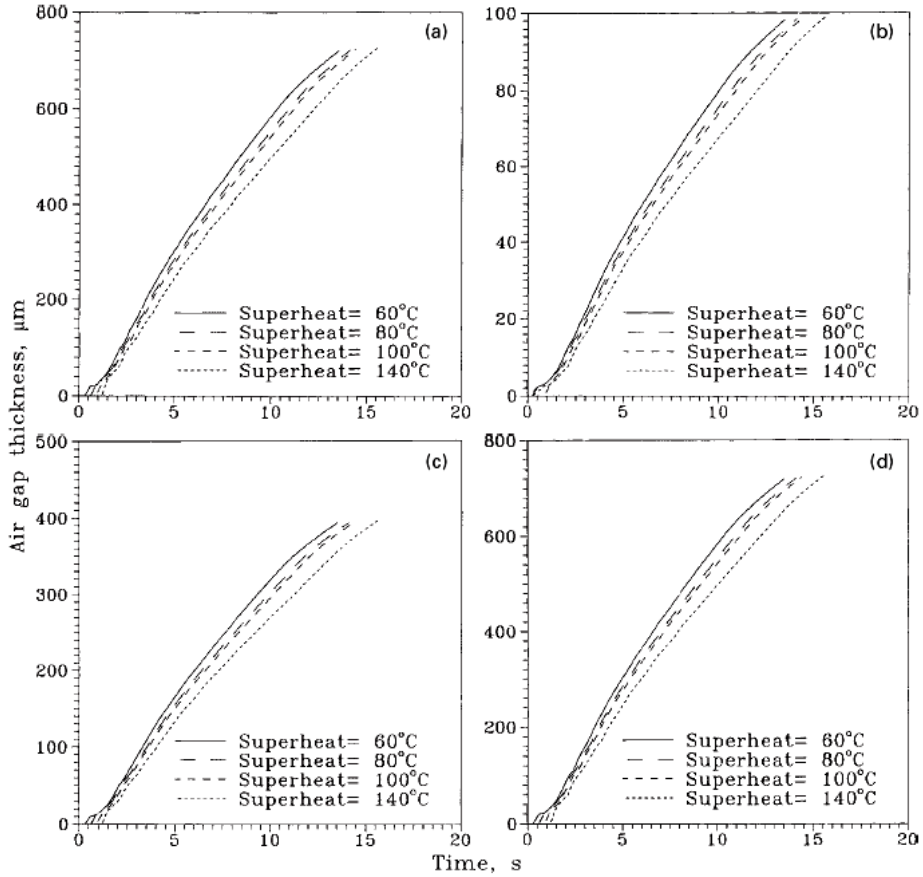

Figure 2-3 Air gap vs. time for pure Al with different degrees of superheat [43].

Trovant and Argyropoulos employed experiments and modeling to apply a temperature boundary condition coupling strategy for modeling of a casting processes [12,44]. In their study, they used pure aluminum and aluminum alloys A356 and A206 solidifying in graphite and copper molds. As expected, the HTC was related to the size of the gap formation, mold surface roughness, conductivity of the gas in the gap, and the thermophysical properties of the metal and mold. They concluded that the air gap formation is the most significant variable in terms of the HTC. Figure 2-4 shows a comparison between conventional and coupled models for the aluminum-copper system and Figure 2-5 illustrates the calculated heat transfer coefficient and air gap predictions for pure aluminum cast in a sand mold.

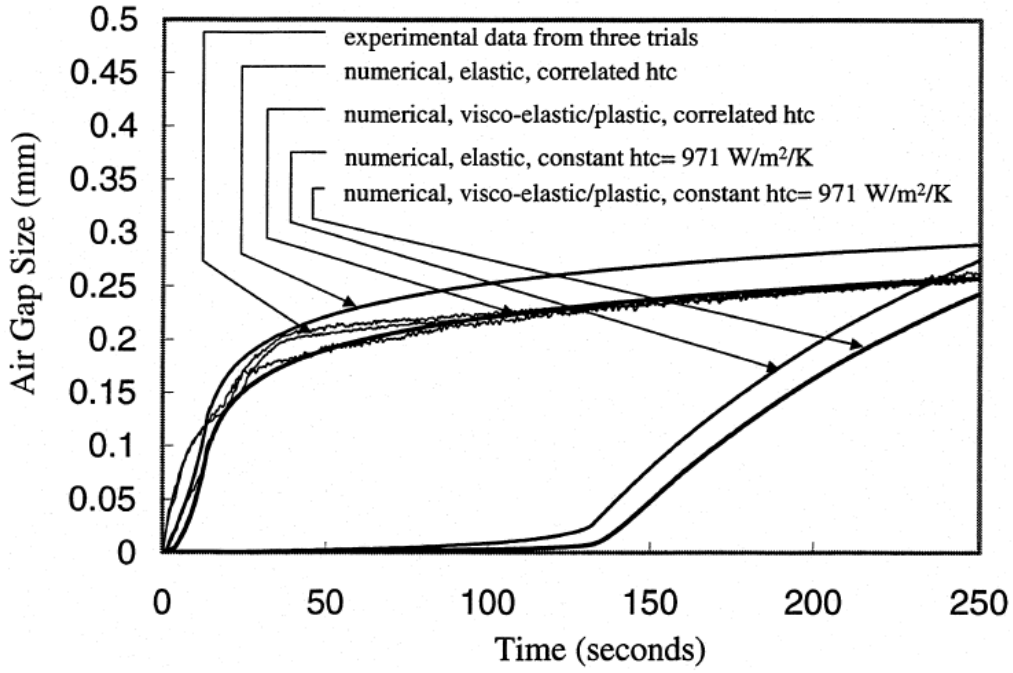

Figure 2-4 Comparison between conventional and coupled models for the aluminum-copper system [12].

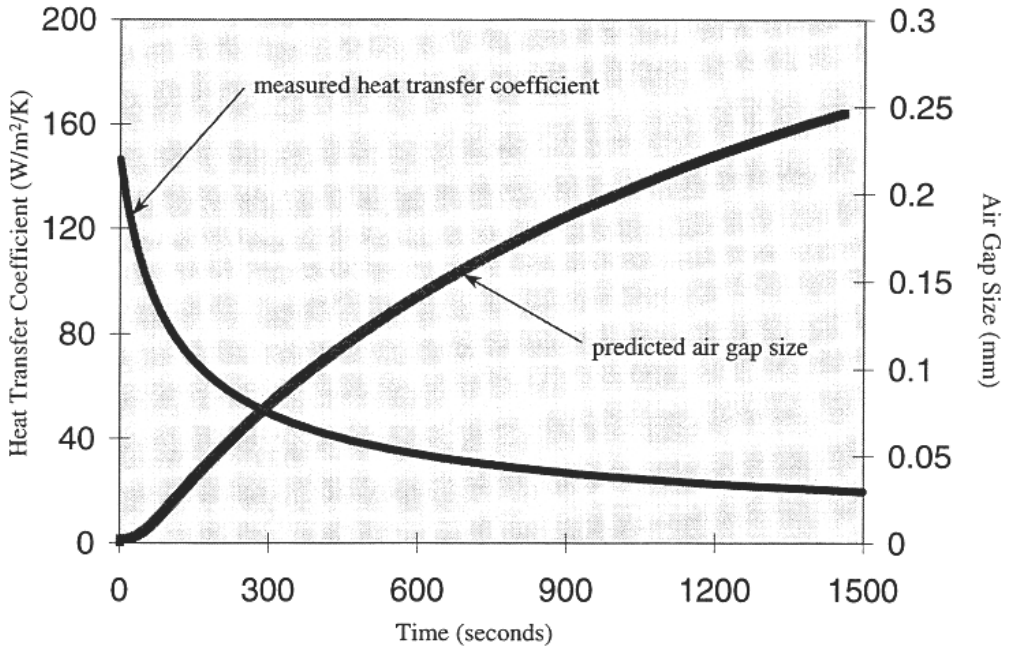

Figure 2-5 Experimental heat transfer coefficient and numerical air gap predictions for pure aluminum cast in a sand mold [12].

Lukens et al. investigated the effect different sands and riser heights have on contact conductance for horizontal cylindrical castings of aluminum alloy A356 [45]. The heat flux was calculated using an inverse method [14] and the interfacial gap was measured. Thermal contact was found to be excellent at the bottom of the mold, but at the top, gap width was reported to be twice as large as at the side. The amount of the formed air gap is greater in the green sand molds. This was recognized to be related to moisture and lower rigidity of the green sand molds.

2.3.2 Mold Parameters

2.3.2.1 Mold Material

The chill or the mold material is another factor that affects the heat transfer coefficient values [7,26,29,31]. The HTC for A356 aluminum alloy during solidification was investigated for different mold material, mold coating material, and coating thickness [46].

Santos et al. studied the effect of chill material, chill thickness, and melt superheat in vertical chill casting experiments with different aluminum alloy compositions [47]. The chill materials were steel and copper. They reported that the HTC could be expressed as a power function of time defined by the general form HTC = $C_i(t)^{-n}$ where the HTC is expressed in W/m².K, t is time (s), and C_i and n are constants depending on alloy composition, chill material, and superheat. The HTC values increased by increasing the chill diffusivity value and decreasing chill thickness.

Muojekwu et al. [31] carried out some experiments by utilizing different types of water-cooled chills including: copper, brass, carbon steel and cast-iron for Al-Si alloys. It is shown that the heat transfer coefficient values are dependent to the thermal diffusivity of the chill and there is a direct relationship between the thermal diffusivity of the chill material and the heat transfer coefficient values. Between the mentioned materials, copper, as it has the least thermal resistance, provided the greater heat extraction rate shown in Figure 2-6. Similar effects of the chill materials are reported in other research works [4,7,39,40,48,49].

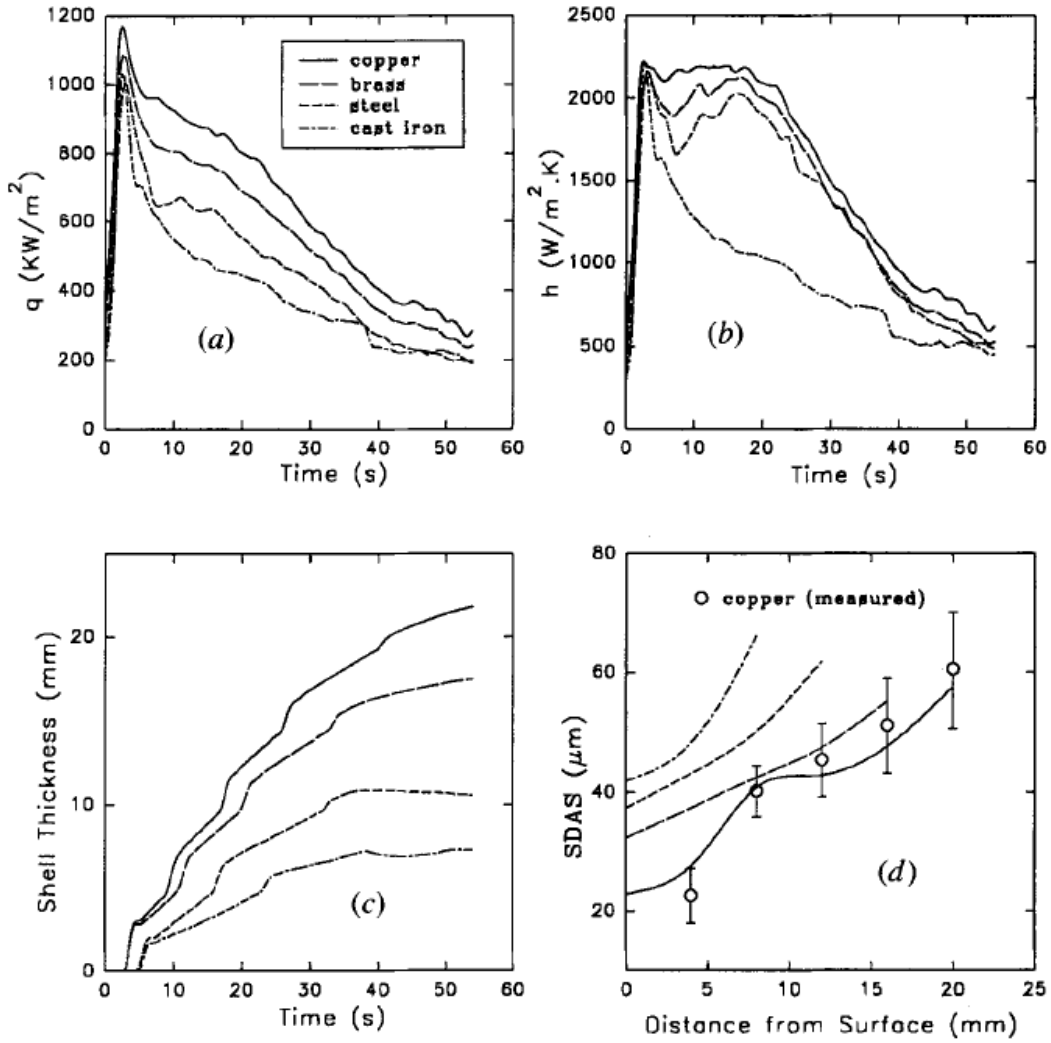

Figure 2-6 Effect of chill material on (a) interfacial heat flux. (b) heat-transfer coefficient. (c) shell thickness profile, and (d) SDAS for A1-7 pct Si (superheat = 30 C°)[31].

2.3.2.2 Mold Surface Roughness

Chill surface roughness is another parameter which affects HTC values [5,31,22,50,51]. Muojekwu et al. [31] studied the effect surface roughness on heat transfer coefficient values. They concluded that heat transfer coefficient values are higher for smoother surfaces. They reported that increasing the surface roughness from 0.018μm to 0.30μm resulted in a 12.6 pct decrease in heat flux and a 17.1 pct decrease in heat transfer coefficient values.

Schmidt et al.[22] investigated the effect of different mold roughness conditions on heat transfer coefficient values. Similar to other work, they found that the heat transfer coefficient values can be doubled when the mold is polished. Chiesa [50] conducted an experiment by

casting A356 aluminum alloy against a cast iron mold and applying surface roughness from 1.0 μm to 25 μm. They also concluded that higher roughness values resulted in lower heat transfer values.

Assar [51] studied similar experiment with pure zinc. Pure zinc was poured at a superheat of 80 K into four cylindrical steel molds of inner diameter 55 mm, wall thickness 10 mm, and height 56 mm which were preheated to a temperature of 473 K before pouring. These molds were machined on a centre lathe such that the inner cylindrical surface had R_a value of 0.043, 0.173, 0.303, or 0.866 mm, shown in Figure 2-7. It is reported that by decreasing mold surface roughness, heat transfer coefficient values were increased. He also mentioned that there was some trend between surface roughness and heat transfer coefficient shown in Figure 2-8.

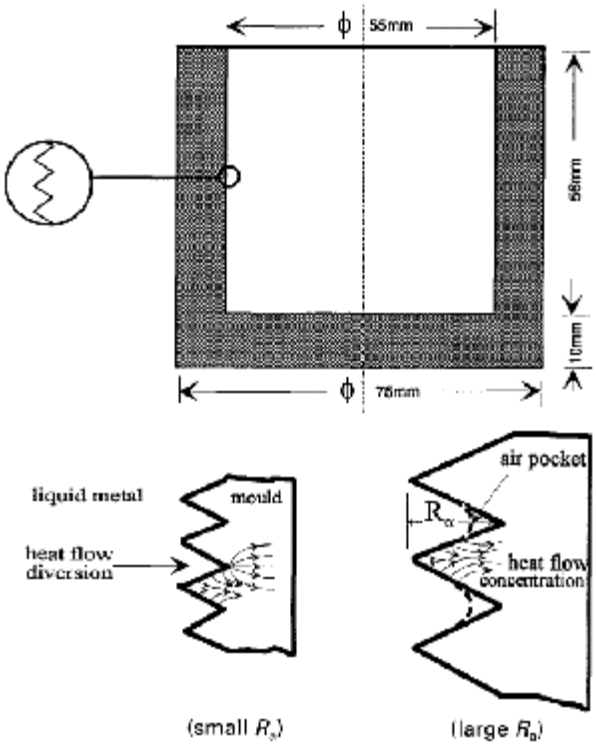

Figure 2-7 Steel mold dimensions and surface condition[51].

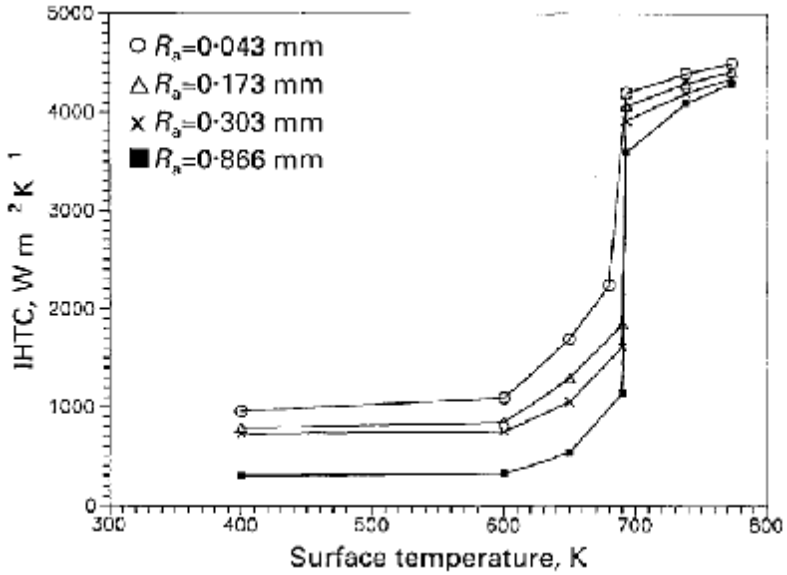

Figure 2-8 Variation of heat transfer coefficient (HTC) with surface temperature for four different values of Ra [51].

2.3.2.3 Mold Surface Coatings

Heat transfer can be increased or decreased by the presence and thickness of surface coating. Schmidt et al.[22] tested the effect of mold coating on heat transfer coefficient for aluminum-silicon alloys. In their experiment a thick layer of ceramic powder was employed. By using the coating, the measured heat transfer coefficient values were smaller than what were anticipated. They explained in their research that using a layer of ceramic powder as coating of the mold can lead to formation of an air gap layer between the mold and the solidifying metal. Schmidt et al.[22], compared the heat transfer coefficient at the metal/mold interface with and without coatings and concluded that the heat transfer coefficient values of uncoated molds were larger than that for the coated molds.

Isaac et al.[25] investigated the effect of using different thickness of coating layer on heat transfer coefficient values. It was shown that the heat transfer coefficient value can be affected by coating thickness. As expected, by increasing coating thickness, the heat transfer coefficient value was decreased. Michel et al. investigated the effect of coating on the heat transfer at the metal-mold interface for Al-Si alloys in steel molds [52]. They reported that the maximum HTC was achieved by employing graphite coating or no coating and the HTC of the chill with

refractory-based coatings was higher than HTC of the chill with vermiculite coating. The effect of coating thickness was investigated in cylindrical castings of aluminum alloy A356 by Venkataramani and Ravindran [53]. Coating thicknesses of 1.0 mm to 2.5 mm were employed. The HTC was found to range from 200 to 18,000 W/m².K for 1.0 mm coatings and from 200 to 1000 W/m².K for 2.5 mm coatings.

Narayan Prabhu et al. studied the effect of mold coating on heat transfer at the casting-mold interface of Al-Cu-Si. They utilized graphite or alumina-based coatings in their research project [54]. As shown in Figure 2-9, they reported higher heat transfer coefficients for graphite coated molds. The heat flux peak was found in the process for thinner casting thickness which is shown in Figure 2-10.

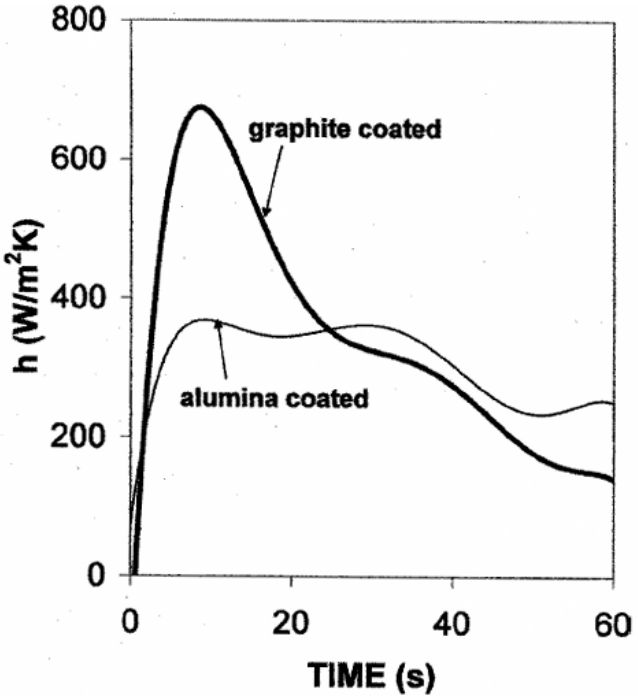

Figure 2-9 Heat transfer coefficients estimated for 10 mm thick molds [54].

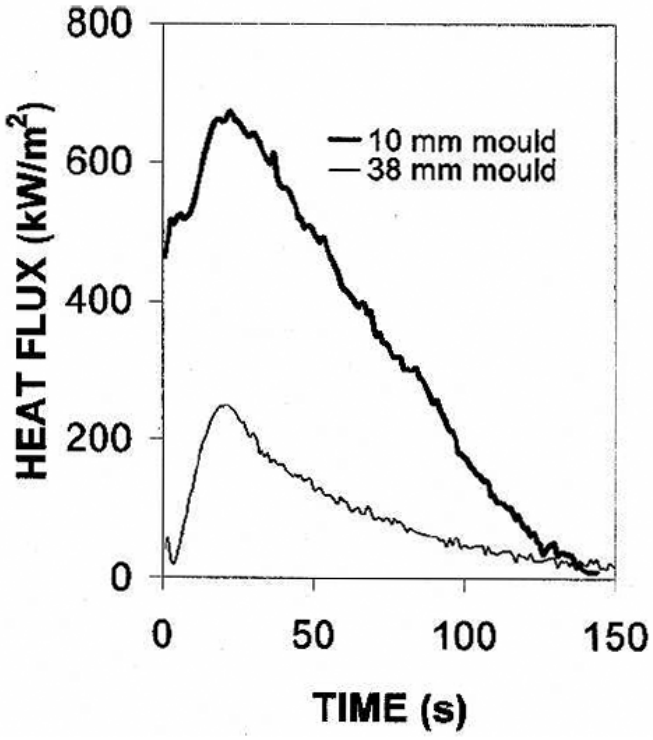

Figure 2-10 Estimated heat flux transients for 12 mm thick casting solidifying in alumina coated molds[54].

2.3.2.4 Pressure at the Interface

Pressure and casting size (height) are other important factors affecting the heat transfer coefficient [24,29,32,34,49].

Krishnan et al. [29] employed different vertical casting heights. It was found that the predicted heat transfer coefficient was directly dependant to the height of the casting. Taha et al. [34] carried out a similar investigation by using pure aluminum and aluminum-copper alloy against copper, steel and dry sand molds. It is concluded that for the same superheat value, increasing the length of the casting height, the value of the heat transfer coefficient will be increased.

Nishida and Matsubara [24] carried out a series of tests to investigate the effect of applied pressure on the heat transfer coefficient at the metal-mold interface. As shown in Figure 2-11, a vertical cylindrical shaped mold was used to cast aluminum. Different values of pressure were applied via a punch inside of the cylinder. By measuring heat flow from sides of the cylinder, the values of the heat transfer coefficient were calculated. It is shown that heat transfer coefficient was significantly increased, when pressure was applied.

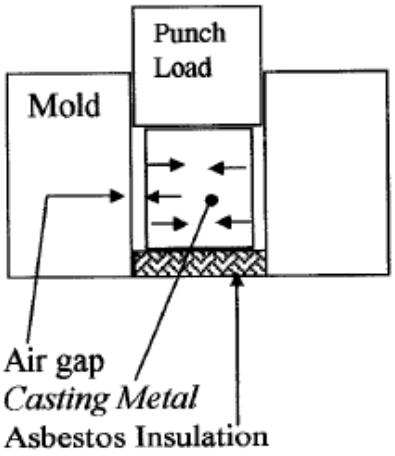

Figure 2-11 Typical Pressure Mold apparatus [24].

Cho and Hong used Al-4.5% Cu aluminum alloy to investigate the HTC for a squeeze casting process [55]. They predicted HTC values of 1,000 W/m²K before applying pressure which rapidly increased the HTC to around 4,700 W/m²K at a pressure of 50 MPa.

Carroll et al. [56] studied the effect of interfacial pressure on the HTC in casting of aluminum alloy with steel molds. They reported an increase of HTC with increasing pressure at the interface

The only work conducted for magnesium alloys was by Weng, Kuo, Wu, and Hwang [57]. In this study they investigated HTC between liquid and semisolid AZ91D magnesium alloy and a SKD-61 steel mold at different pressures. They conducted the experiment with a cylinder that was chilled at one end by a water-cooled steel chill. For the high pressure semisolid experiments, the maximum HTC reached just over 7 kW/m^{2}K for casting pressures of 4.9 and 9.8 MPa and around 13 kW/m^{2}K for a casting pressure of 14.7 MPa.

Sekhar et al. [58] conducted a research project to investigate the effect of pressure on metal-die heat transfer coefficient during solidification of Al - Si eutectic alloy against an H-13 die. As shown in Figure 2-12, they employed 4 thermocouples located at different distances from the metal-die interface. Thermocouples are located in the cold top die half which extracts heat from the cylindrical specimen as the specimen is pressurized. It was found that application of a pressure of 196 MPa increases the heat transfer coefficient from about 3.4 to 52.5 kW/m²K, illustrated in Figure 2-13. The effects of different die coatings on the heat transfer coefficient were also determined.

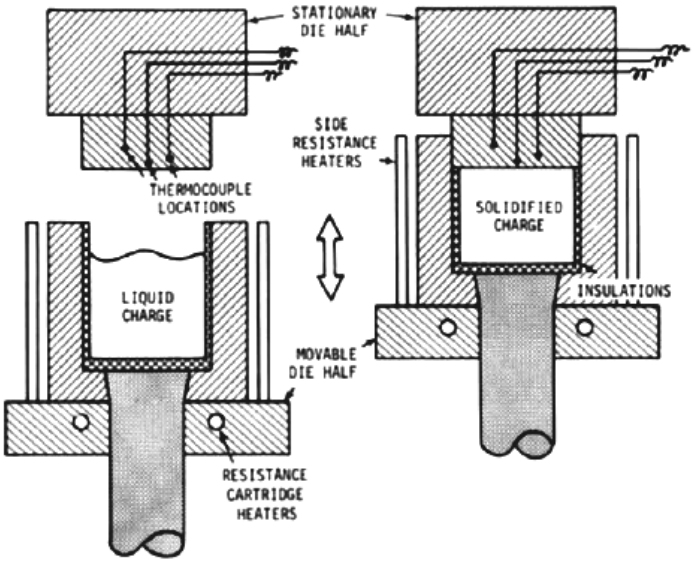

Figure 2-12 A schematic illustration of the dies used in thermal behavior studies [58].

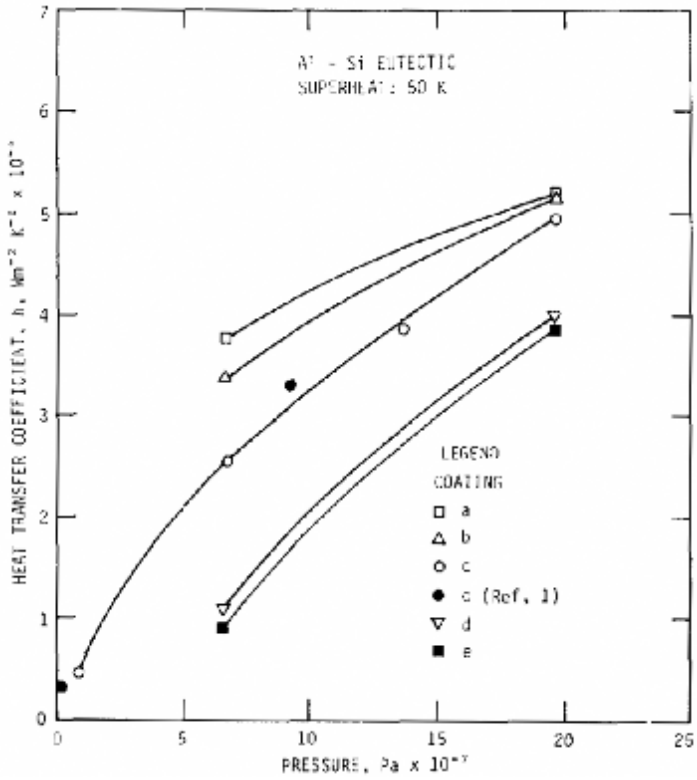

Figure 2-13 The effect of applied pressure and die coating on the heat transfer coefficient at the metal-die interface [58].

2.3.3 Cast Metal Parameters

2.3.3.1 Cast Orientation

Another parameter that can affect the heat transfer coefficient values is casting surface orientation. Krishman et al. [29], did a series of experiments with several aluminum alloys to calculate the heat transfer coefficient during unidirectional heat flow. As it can be seen in Figure 2-14, two different orientations of chills against solidifying metal were used: (a) top vertical arrangement (b) bottom arrangement. It is reported that the bottom chill resulted in higher heat transfer coefficient values as compared with the top chill arrangement as the bottom chill is in more intimate contact with the metal due to gravity. Ho and Pehlke [7], reported similar results by casting pure aluminum and aluminum- copper alloys against a vertically arranged copper chill. Figure 2-14(a) and (b) shows experiments of Ho and Pehlke [7] and Krishman et al. [29].

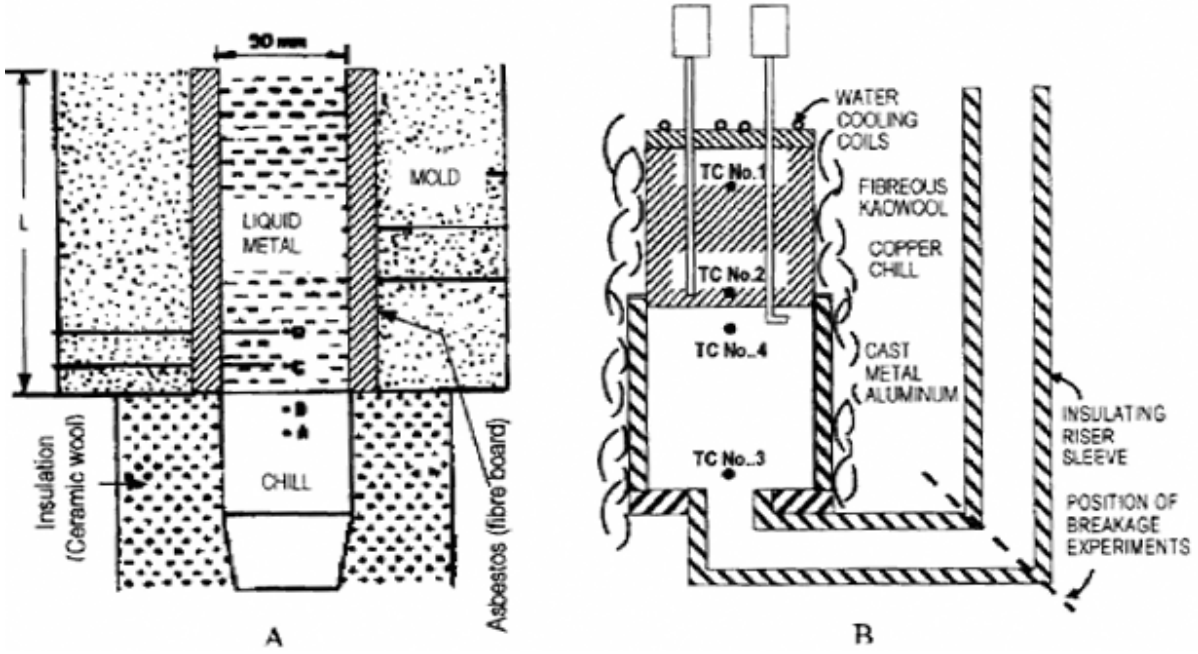

Figure 2-14 (A) Casting setup for constant metallostatic head experiment [29].

(B) Casting setup for receding head experiment [7].

2.3.3.2 Cast Superheat

In the casting process, it is necessary to apply some amount of superheat to fill any mold cavity. The effect of superheat on heat flux and heat transfer coefficient at the interface of metal and mold has been investigated [31,59,43,37].

Muojekwu et al. [31] studied the effect of secondary arm spacing and surface roughness on heat transfer coefficient values. The experiments were done by utilizing the different types of the chills namely: copper; brass; carbon steel, and; cast iron. They concluded that heat flux and heat transfer coefficient values were increased by increasing superheat that the increased superheat caused an increase in interfacial contact because:

1) There is reduced viscosity at high temperatures, and

2) High superheat doesn't support the preliminary formation of a thick solidified shell, which forms an air gap between the solidifying molten metal and the chill interface.

Furthermore, greater superheat would cause a greater initial driving force for heat flow across the interface.

Taha et al. [43] studied the effect of chill material and cast superheat of the heat transfer coefficient for an Al-Cu alloy casting. It is reported from their research work that for a sand and copper chill, the heat transfer coefficient increased with increased metal superheat.

Gafur et al. [59] conducted a research project to study the effects of superheat on HTC of casting of commercially pure aluminum. Faster initial increase in the chill surface temperature was achieved by higher superheats. Chill thickness effects were observed only after the heat from the solidifying metal had sufficient time to diffuse to the bulk of the chill material. Though the effect of chill thickness on the HTC was not significant, higher superheats resulted in higher heat transfer coefficients, as illustrated in Figure 2-15 and Figure 2-16.

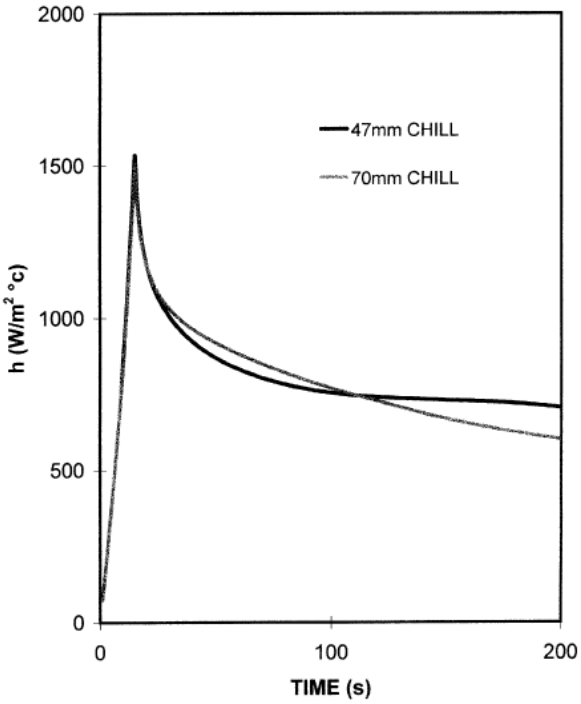

Figure 2-15 Effect of chill thickness on heat transfer coefficient for a pouring temperature of 730 Cº [59].

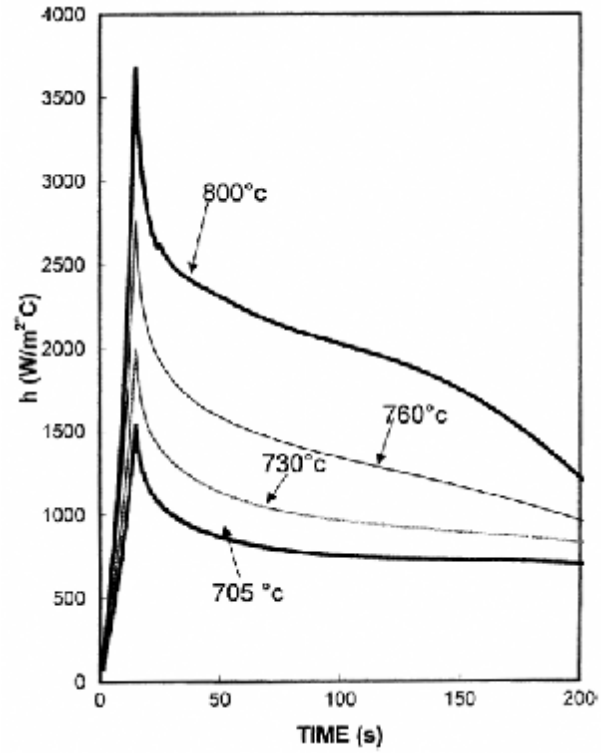

Figure 2-16 Effect of superheat on heat transfer coefficient for 47mm chill [59].

2.4 Heat Transfer during TRC

Heat transfer during the Twin Roll Casting (TRC) process for low–carbon steels was studied by Guthrie and Tavares [60,61,62]. In their study they used a pilot caster with a roll radius of 0.30 m, producing steel strips with thicknesses ranging from 4 to 7 mm, at relatively low casting speeds in the range of 4 to 12 m/min. Calculated heat flux variation during vertical twin roll casting is shown in Figure 2-17.

By employing installed thermocouples inside of a pilot twin-roll caster rolls, heat fluxes at one of the roll-strip interfaces were modeled. In the experiments, the roll separating force was kept approximately constant at 20kN. Temperature data was acquired at a frequency of 10 HZ during the entire casting process. The recorded temperatures by thermocouples then used to model the interfacial heat flux by an inverse heat transfer solution. By employing a Lagrangian coordinate system, moving with the same speed of the rolls and thermocouples, the heat conduction equation was reduced to the one-dimensional equation. The recorded temperatures of the outer thermocouples from the roll surface were used as boundary conditions while the measured temperature profile values by the thermocouples closer to the roll surface were used as the fitting parameter for calculating the interfacial heat fluxes values. Figure 2-19 shows temperature-time data recorded by TCs and Figure 2-20 shows the typical variation of the predicted heat fluxes during one of the experiments. The peaks in the heat fluxes correspond to those periods of contact between that part of the roll containing a set of embedded thermocouples and the solidifying metal.

In this process because of heat transfer from rolls to the casting material, solidification begins at the first contact point of the rollers and the casting metal. Meanwhile, because of the shrinkage of the solidified shell, a thin air gap layer forms between the rollers and the casting metal. Presence of this thin air gap layer causes two modes of heat transfer:

a) Conduction at the interface of the solidified shell and the roll.
b) Convection and radiation in where the air is trapped between the shell and roll which causes a low heat flux value from the solidified metal to the rolls as shown in Figure 2-17 (region 1).

By increasing the temperature of the rolls, expansion of the rolls occurs which causes an increase in metallostatic pressure and the pressure on the solidified shell increases. Because of this increased pressure, the thin air gap would be reduced or eliminated which, as it is shown in

Figure 2-17 region 2, causes more contact area between the rolls and the solidified metal and higher heat flux. Finally the solidified shell starts to shrink which lead to less contact area between the rolls and the solidifying metal and consequently, less heat flux that is shown in Figure 2-17 region 3.

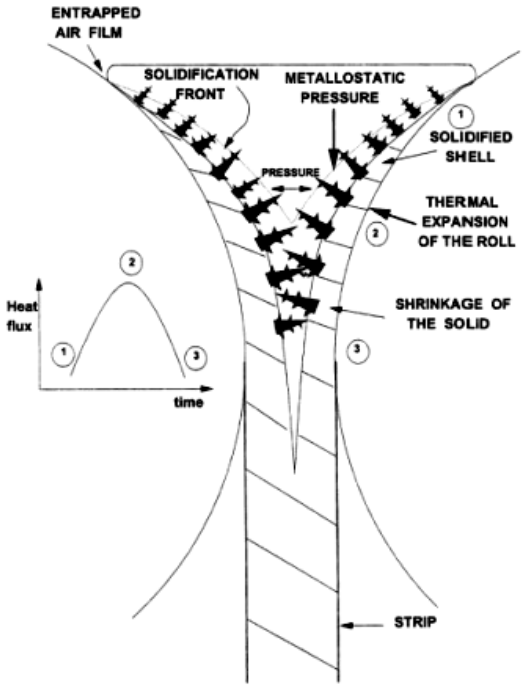

Figure 2-17 Mechanism used to specify variation in heat flux [61].

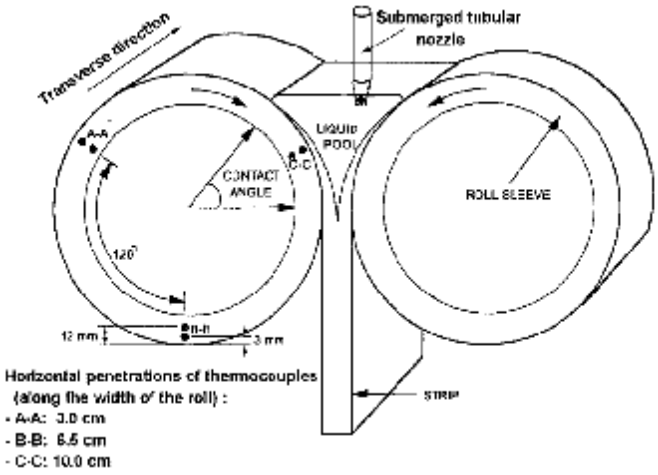

Figure 2-18 Equipped rolls with thermocouples used for steel TRC to evaluate HTC [61].

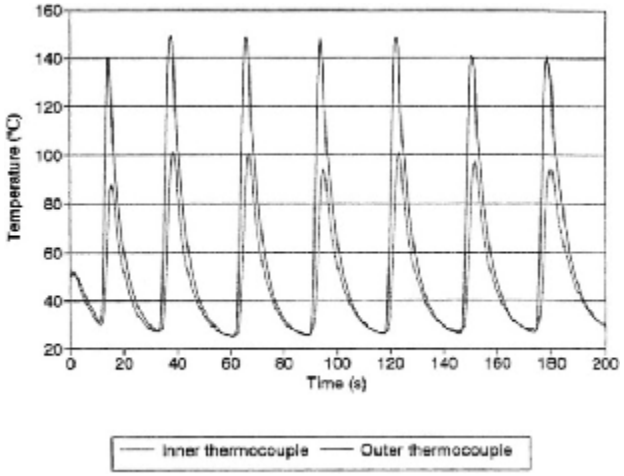

Figure 2-19 Temperature-time data recorded by thermocouples.

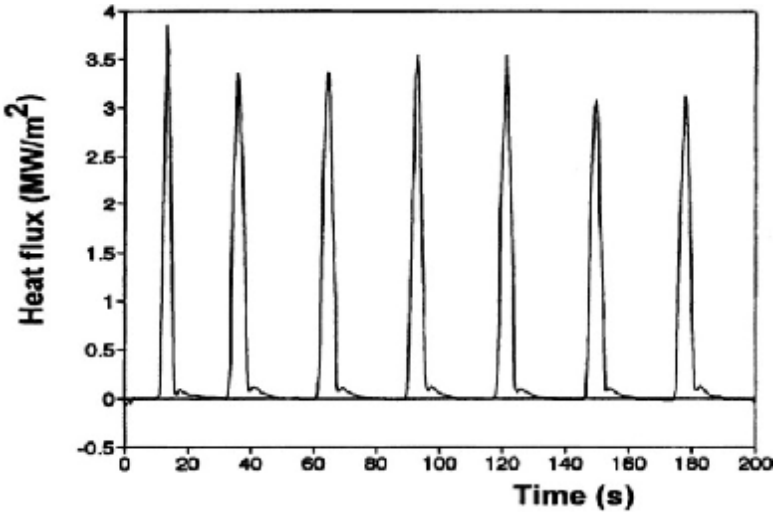

Figure 2-20 Corresponding heat flux calculated by inverse method [61].

Hlady et al. [63] conducted research work to investigate the heat-transfer coefficient (HTC) in the roll gap during the hot rolling of AA5xxx aluminum alloys. They employed some thermocouples attached to the surface and inside the test samples. The heat-transfer coefficient was modeled by recording temperature history and employing an implicit finite-difference model at different strain rates, and pressures. They reported heat transfer coefficient values of 200 to 450 kW/m^2°C. Also they developed an equation to define the HTC as a function of the ratio of the rolling pressure to the flow stress at the surface of the work piece. Figure 2-21 shows the effect of mean rolling pressure on the HTC in the roll gap.

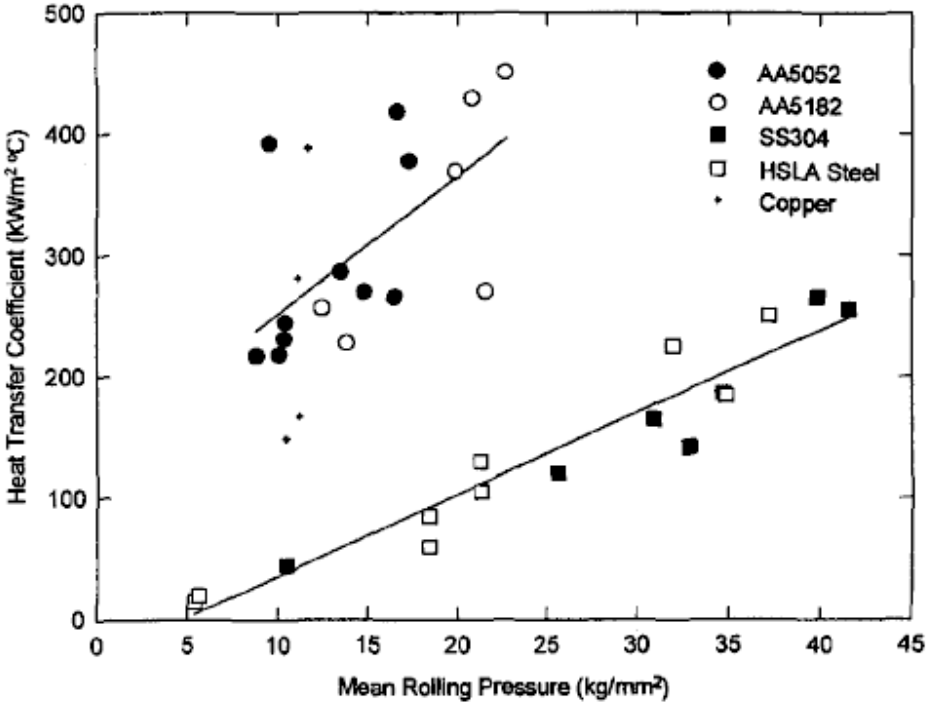

Figure 2-21 Influence of mean rolling pressure on the HTC in the roll gap [63].

2.5 Summary

Many researchers have investigated the heat transfer coefficients for a variety of casting techniques. Some of the parameters that are known to affect the HTC during casting at the metal/mold interface include: thermo physical properties of the casting material and mold; mold surface roughness; melt superheat; and pressure at the mold/metal interface. Designing and building an apparatus to test the effect of all parameters such as chill/roll material, chill surface roughness and coating, superheat and pressure, especially for the light metals such magnesium which is difficult to cast, is essential.

Chapter 3 Experimental Procedure

A test apparatus was built to measure the interface heat transfer coefficient between liquid metal and a chill in order to get quantitative information on the HTC during Twin Roll Casting (TRC). The apparatus was developed such that the temperature history in both the melt (casting) and chill (mold) could be measured at known locations. This chapter explains the design of the experimental apparatus as well as the sensors used during the experiment. Finally, a description of a typical experimental procedure is given.

3.1 Casting Heat Transfer Simulator

The overall design of the experimental apparatus (casting heat transfer simulator) is shown in Figure 3-1 below. This experimental apparatus was designed to allow different parameters such as: the chill material and test metal; the roughness and texture of the chill; the superheat of the test metal; and the pressure at the interface to be investigated to observe how the heat flux and HTC are affected. As shown in Figure 3-1 and Figure 3-2, the apparatus consists of five main parts; namely: the heater assembly; pressure assembly; chill apparatus; frame and the top and bottom plates. The test metal to be melted is placed in an open ended H13 tool steel cylindrical vertical chamber surrounded by heaters. A piston is inserted in the chamber from above sealing the top from the environment. The head of the piston contains spring rings to ensure the seal is tight and will minimize the leakage of molten metal around the sides of the piston when pressure is applied at the interface. The bottom of the cylinder is sealed by the chill block. The test metal rests on the water chilled block and it is the heat transfer at this interface (between the chill block and test metal) which will be assessed.

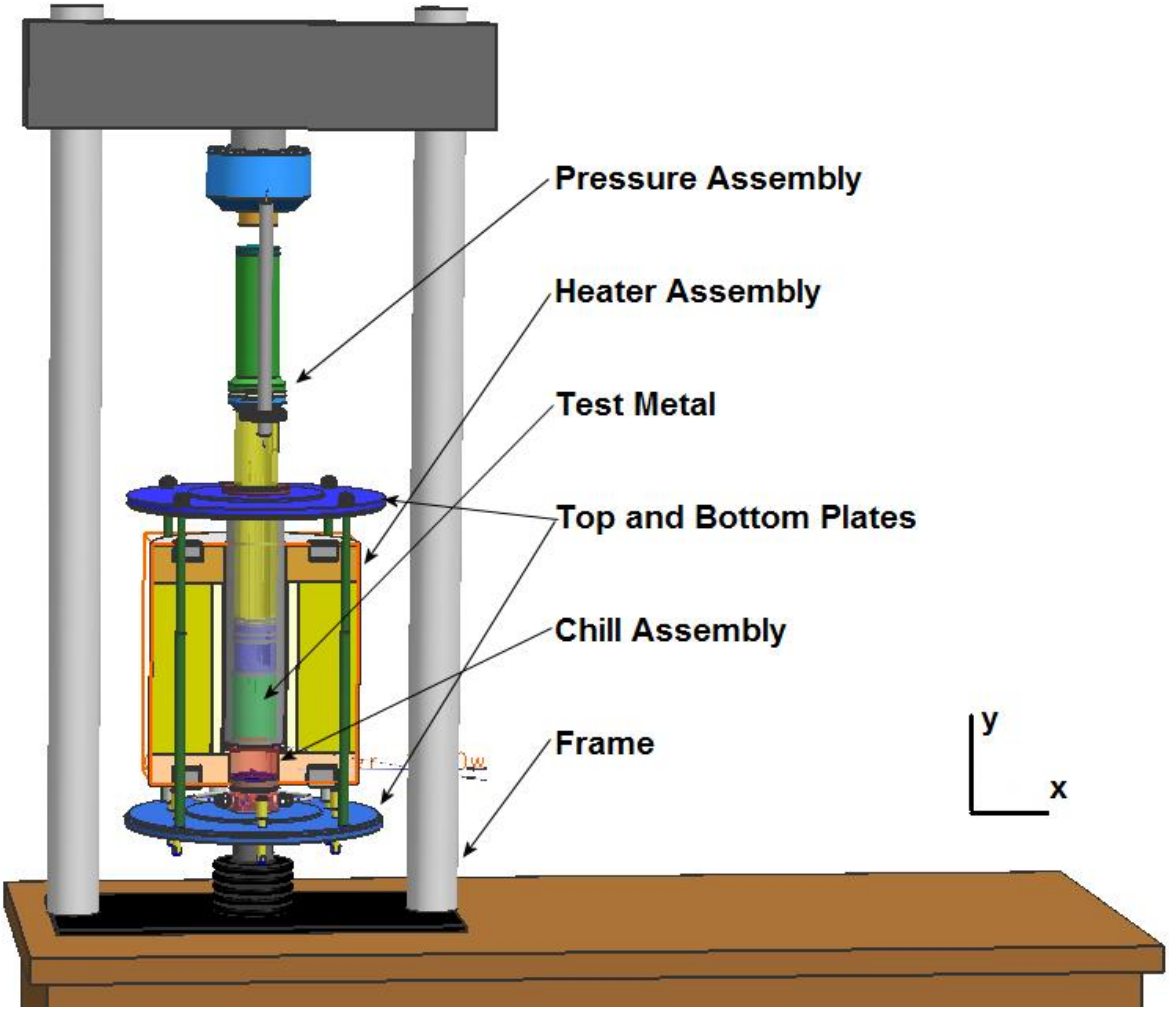

Figure 3-1 Schematic overview of experimental apparatus.

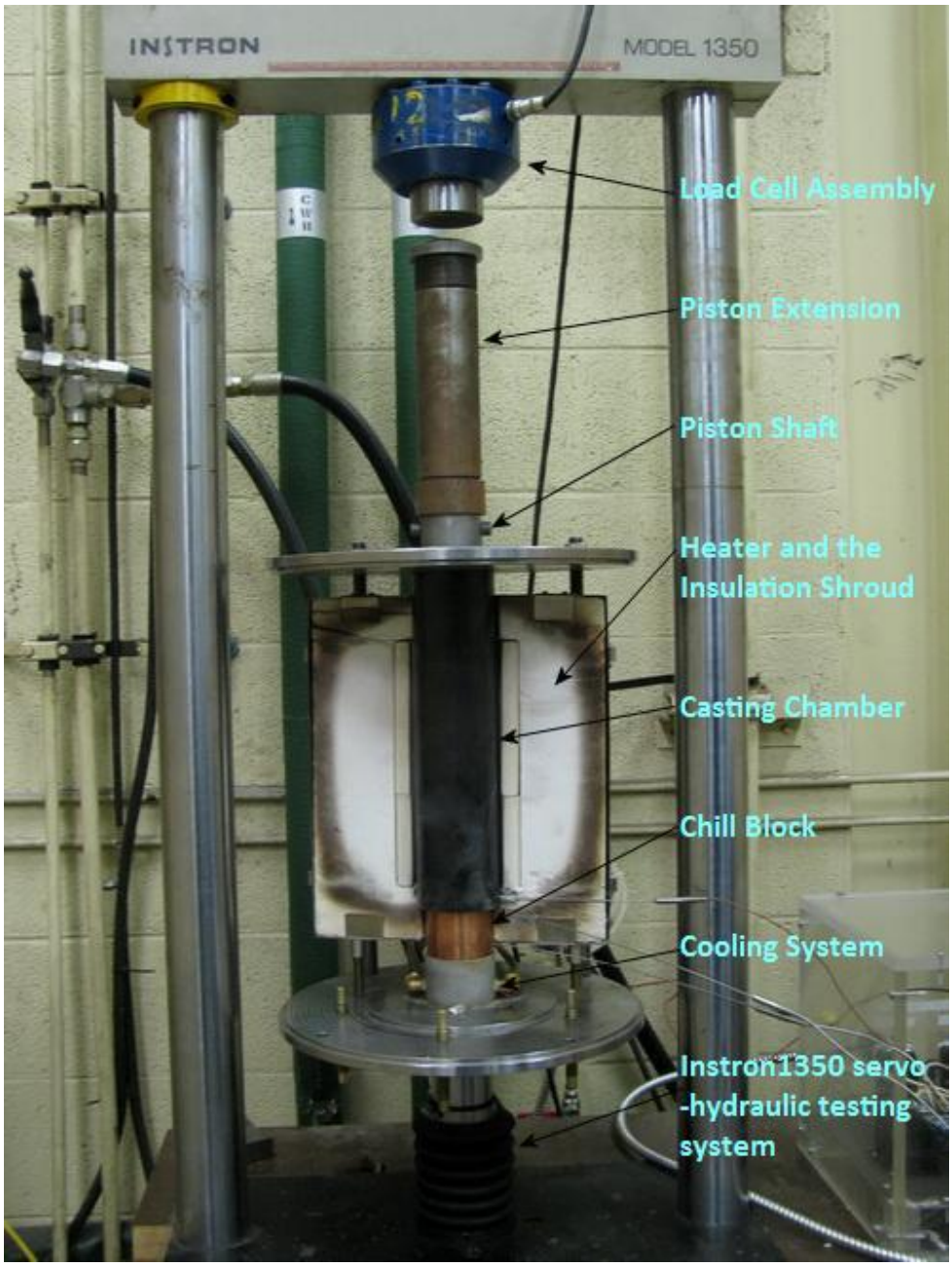

Figure 3-2 Experimental apparatus.

Insulation surrounds the entire assembly to ensure the majority of the heat flow occurs in the y-direction (vertical) from the liquid metal into the chill block. The frame consists of a top and bottom plate held together by four rods. As the four rods are tightened, the bottom plate presses firmly against the chill from the bottom, and the top plate presses against the chamber from the top. This ensures the assembly will survive the high pressure of the experiment and

liquid metal leakage will not occur. This apparatus is placed on a high-pressure Instron frame equipped with a load cell. The apparatus is instrumented with seven thermocouples. Two thermocouples are placed inside the chill, four are placed on the surface of the piston head to measure the temperature of the solidifying material, and one thermocouple is placed against the outside surface of the chamber.

Before the experiment starts, the heaters are used until the desired metal test temperature is reached and equilibrated. Once this has occurred, the water circulation will be started to cool the chill block. During the experiment, the base upon which the furnace assembly rests is slowly pushed upwards by a hydraulic arm. As the apparatus moves up, the stationary piston rod is forced into the cylinder to build up pressure in the chamber. The back end of the piston is pressed against an insulated load cell.

The data acquisition system, which the thermocouples are connected to, has a sampling rate of 10 Hz and outputs the results to a text file. After the experiment, the thermocouple data (temperature-time history at a known location) was analyzed to determine the heat flux at the interface between the chill block and test metal.

3.1.1 Frame

The frame of the Casting Heat Transfer Simulator consists of a top and bottom plate held together by four rods. As the four rods are tightened during a test, the bottom plate presses firmly against the chill assembly, and the top plate presses against the chamber from the top. This ensures the casting assembly will survive the high pressure of the experiment and minimize liquid metal leakage in the chill block chill. The rods are 542mm long with diameter of 16 mm. The diameter of the plates is 250mm with thickness of 25 mm made from mild steel. Figure 3-3 shows detailed dimensions of the frame and the sketches of the top and bottom plates and four rods.

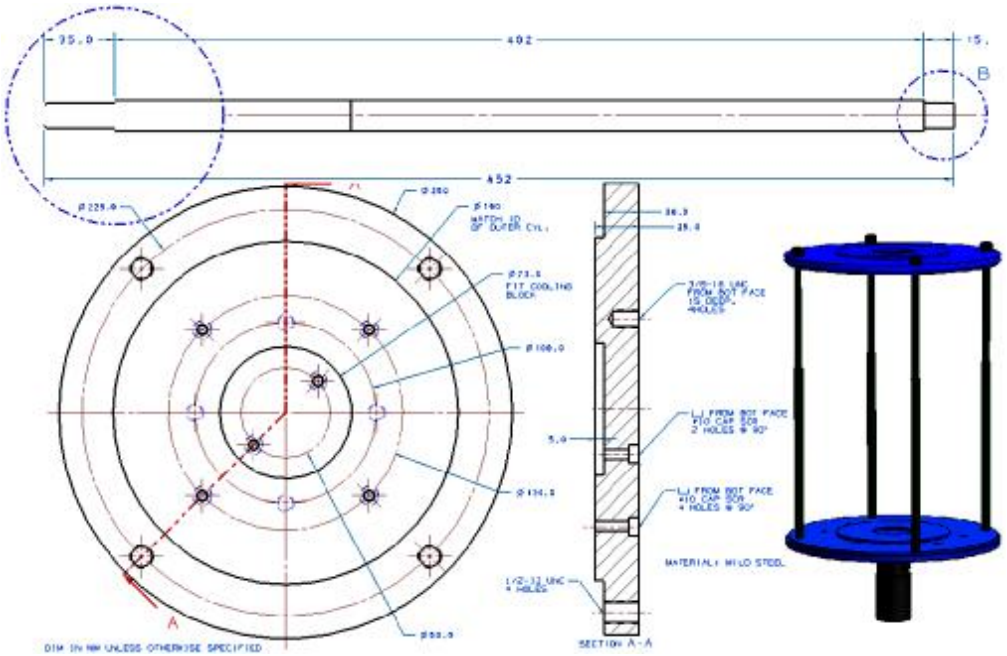

Figure 3-3 Schematic of top/bottom plate.

3.1.2 Chill Assembly

The chill assembly was designed to ensure sufficient heat could be removed from the molten metal and was instrumented with two thermocouples to ensure accurate temperature time history at two known locations during a test. This assembly consists of two main parts:

- Cooling System
- Chill Block

3.1.2.1 Cooling System

The cooling system consists of two distinct parts, namely: the main water cooled section and a cover which is in contact with the chill block. Both parts were made from aluminum and joined together using laser welding. To build the cooling system, as shown in Figure 3-4, circular water channels were machined inside an aluminum block such that two holes were used for the inlet water and one hole for outlet water. The water is provided to the chill through copper tubes. The diameter of the cooler is 73mm and it has a height of 50mm. Figure 3-4 shows the sketches of the main part and Figure 3-5 illustrates dimensioned drawings of the cover. Additional sketches of these parts are provided in Appendix B.

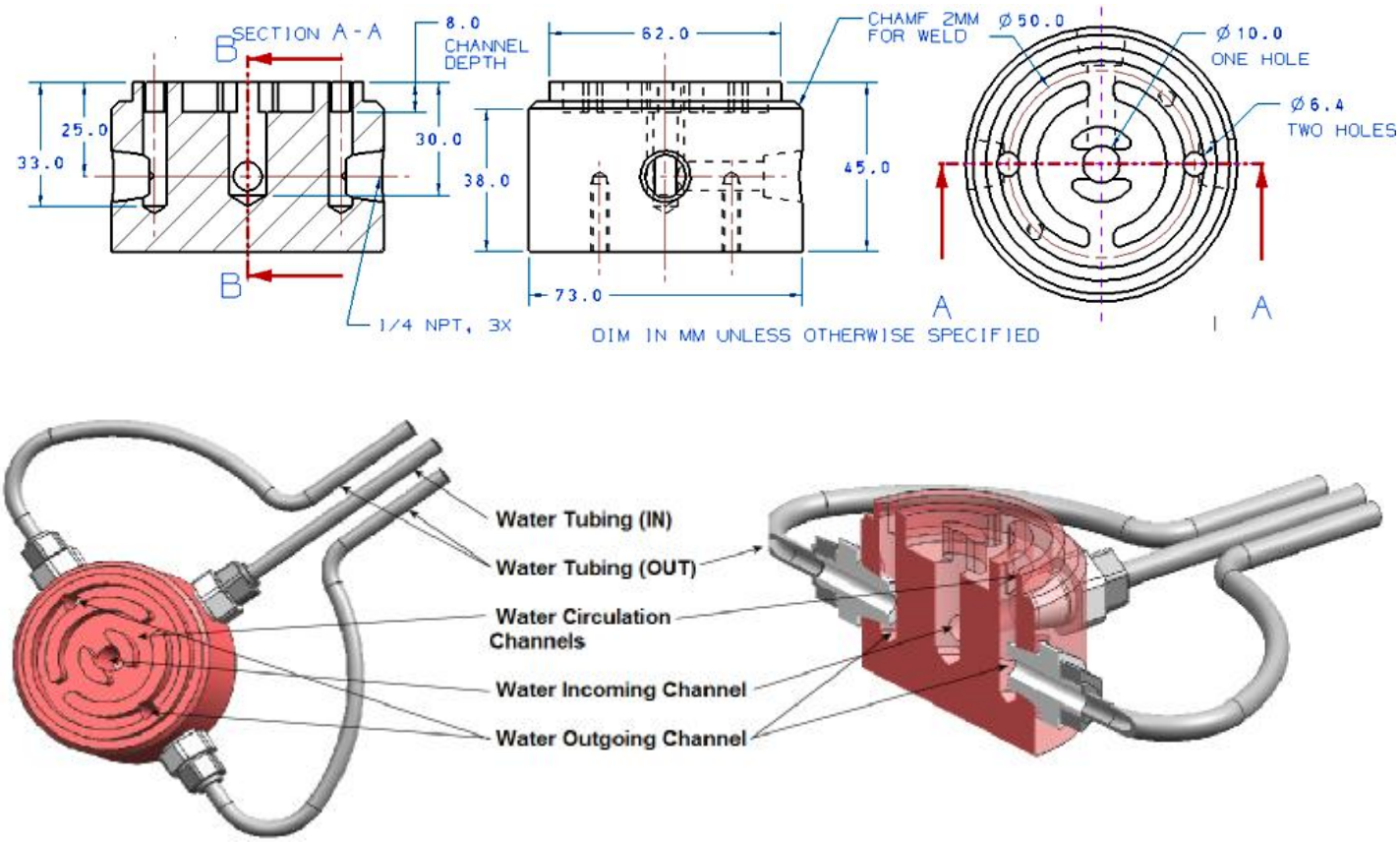

Figure 3-4 Cooler Details showing a) Detailed CAD drawings of the dimensions (in mm) and b) NX works schematic.

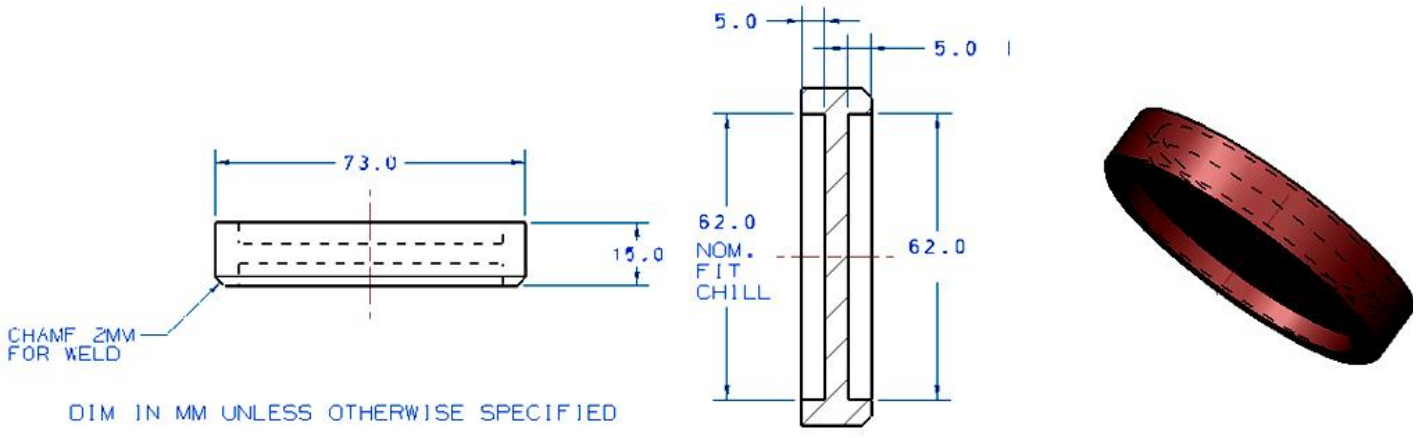

Figure 3-5 Cooler cover details and dimensions (in mm).

The cooler assembly is shown in Figure 3-6 showing the assembled cooling system with the cooler, cover and copper tubing for the water.

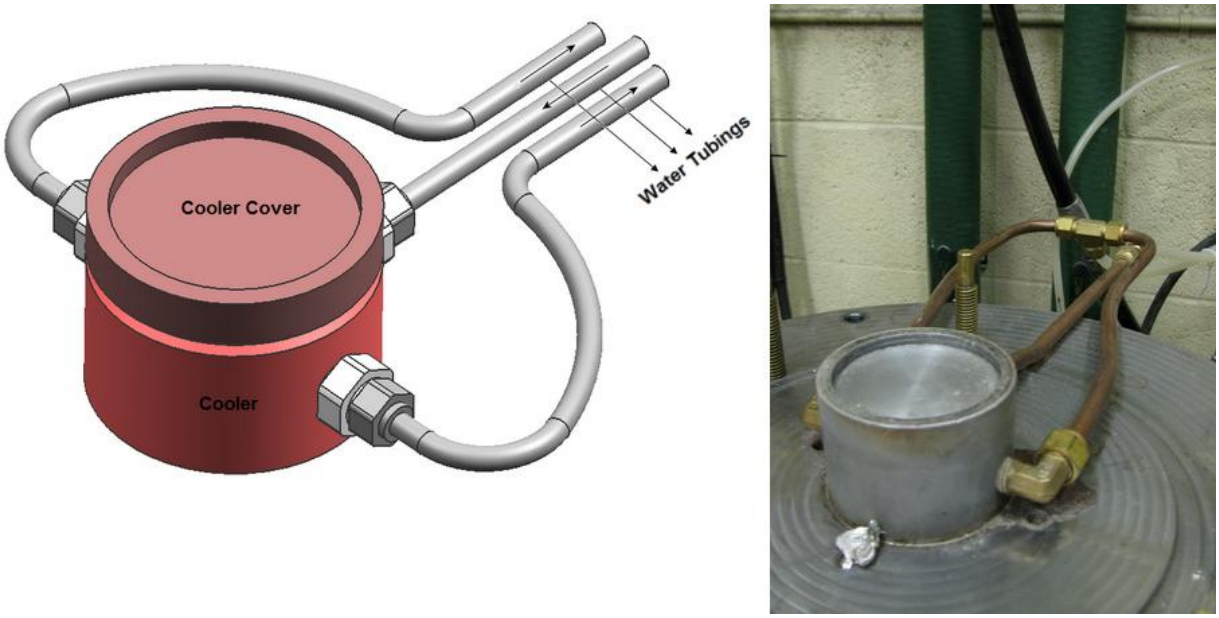

Figure 3-6 Cooler Assembly.

3.1.2.2 Chill Block

The chill block is the block which sits on top of the chill assembly cover and is in contact with the liquid metal during a test. Figure 3-7 shows its architecture and dimensions. In this research, the chill block was made from a H13 tool steel which thermophysical properties are given in Table 3-1.

Table 3-1 Thermophysical properties of the H13 used for the chill block.

Metal Mold	Thermal Conductivity (W/m.K)	Density (kg/m^3)	Specific Heat Capacity (J/kg.K)
H13 Tool Steel[64]	24.5	7800	460

To produce the chill blocks, all specimens were machined into a cylinder with dimensions of 64mm diameter and 60 mm height. Two flat-bottomed holes were drilled inside

the chill block so that it could be instrumented internally with T/C's. A 1.7 mm diameter hole was drilled to the centre of the chill at heights of 2mm and 45mm below the interface between the chill block and test metal. The hole for the upper had to be drilled at an angle because of the reduced diameter close to the top as shown in Figure 3-6. Appendix B provides additional details on the holes drilled and placement of the TC's in the chill block.

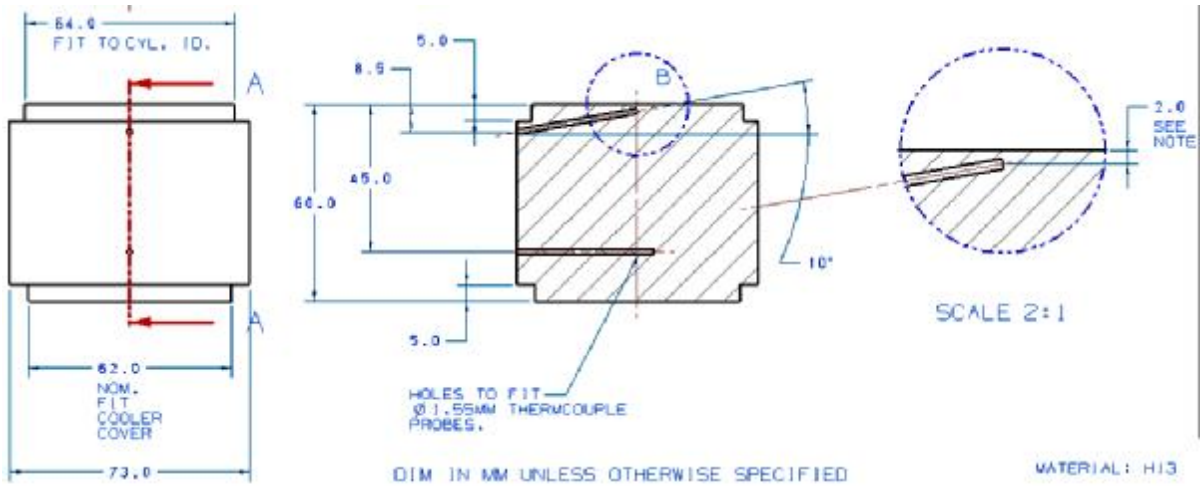

Figure 3-7 Chill block dimensions (in mm).

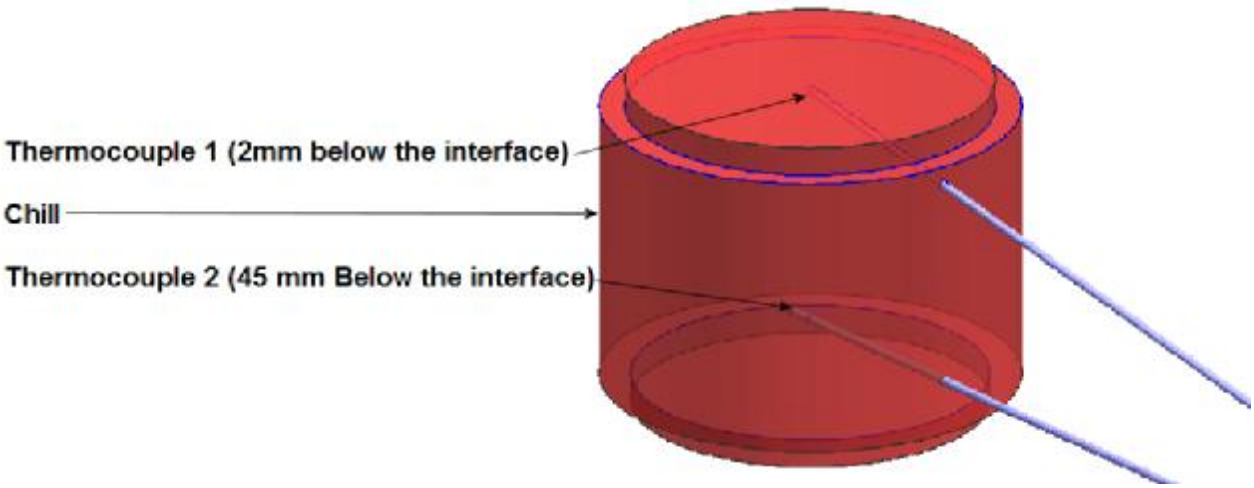

Figure 3-8 Chill details.

Details in Appendix A provide calculations which indicate that the end of the hole where the TC tip will be placed is a distance of 2.01 to 2.05mm from the interface. Accurate knowledge of this location is critical to ensure that the IHC calculations for the heat flux are representative.

To study the effect of roughness on the heat transfer characteristics between the chill and melt, a particular surface roughness was imposed on the top of the chill block which was in contact with the test metal prior to the start of a test using a lathe. Surface roughness ranging from 0.1μm to 43μm (peak to valley roughness) were tested. Figure 3-9 shows the surface of the chill block in contact with the cast metal section of the mold with the two different surface textures/roughness applied.

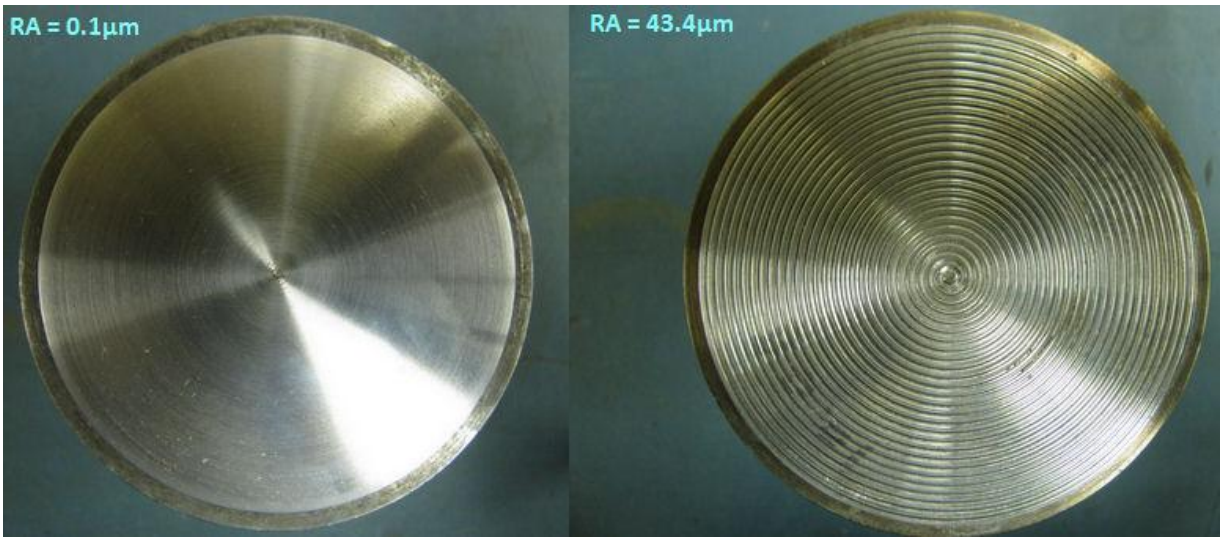

Figure 3-9 Surface of the chill blocks.

The surface roughness of the specimens was evaluated by employing a Surtronic3+ which is shown in Figure 3-10. This device is a portable, self contained instrument for the measurement of surface texture.

Figure 3-10 Surtronic3+.

3.1.3 Test Metal

The test metal used in this project was a tin alloy called Babbitt alloy (Sn-7.5%Sb3.5%Cu). For each test sequence, a solid cylinder with a diameter of 64mm and height of 100mm was machined from the alloy. Four holes with a diameter of 1.7mm at the correct radial position with respect to the location of the TC's were also drilled. Figure 3-11 shows the dimension of the test metal and the position of the thermocouple holes in it.

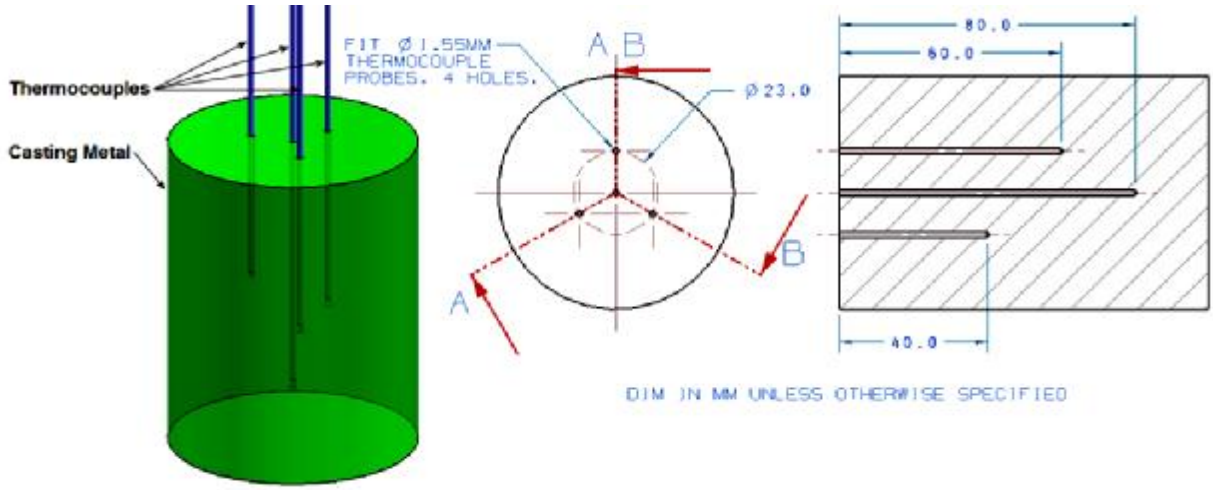

Figure 3-11 Test metal dimensions and details.

The solidification range and the fraction of each phase at different temperatures were calculated using the FactSage thermodynamic software for this alloy and is shown in Figure 3-12.

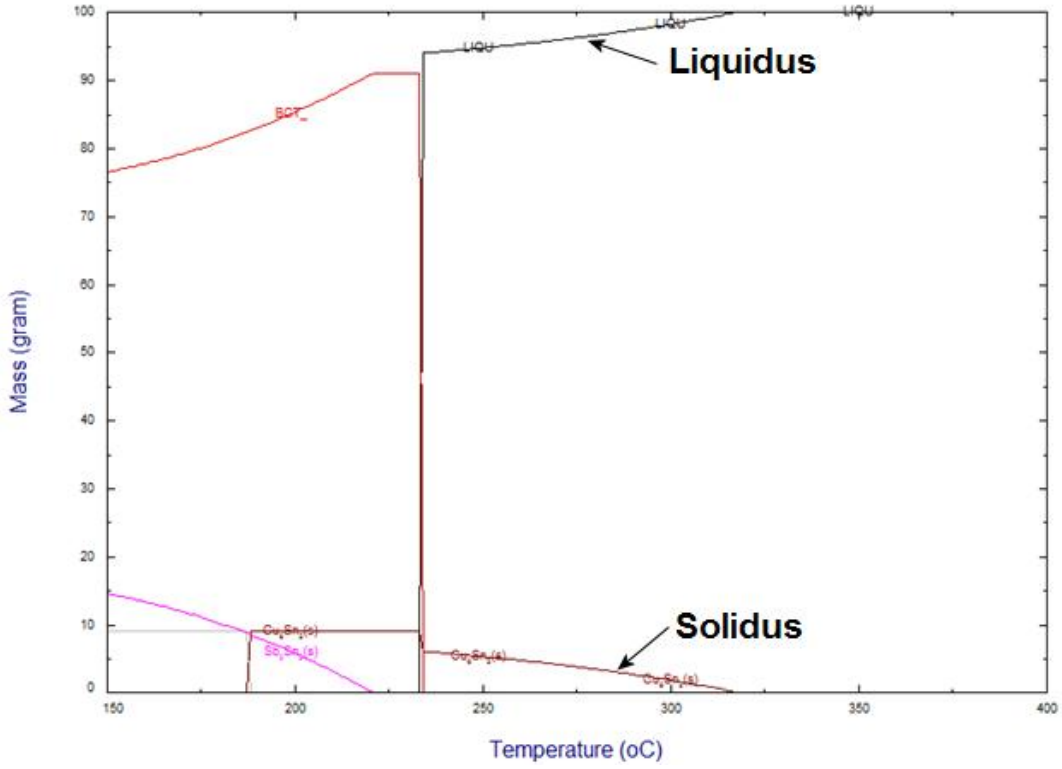

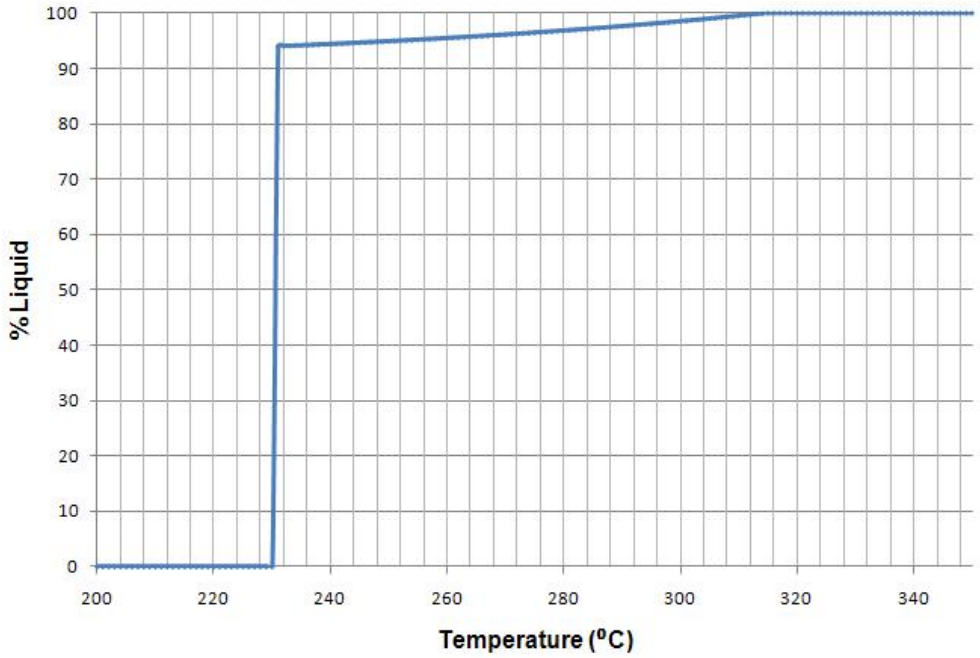

Figure 3-12 Solidification range of Sn-7.5%Sb-3.5%Cu alloy.

3.1.3.1 Thermohysical properties of Sn-7.5%Sb-3.5%Cu[1]

Generally, it can be written:

$\lambda(T)= \lambda_{elec}(T)+\lambda_{ph}(T)$

where λ, λ_{elec} and λ_{ph} are respectively, the total, the electronic, and the lattice thermal conductivity. The interdependence of λ_{elec} and λ_{ph} is difficult to formulate, but it has been shown that, for metals (liquid and solid phases) at temperatures higher than the Debye temperature, the lattice contribution is around 1% of the total thermal conductivity. Thus, the thermal conduction is mainly due to transport of electrons. Consequently, the modified Wiedemann-Franz rule relating thermal and electrical (σ) conductivity can be used with confidence to predict the thermal conductivities of metal alloys. The Wiedemann-Franz relation is described in Appendix C.

Estimation of thermal conductivity is based on the measurement of electrical conductivity of Sb-Sn and Cu-Sb-Sn Sn-based alloys and using a rule of mixtures [65] was calculated as shown in Figure 3-13.

[1] Provided by Dr. Aimen Gheribi, Ecole Polytechnique de Montreal

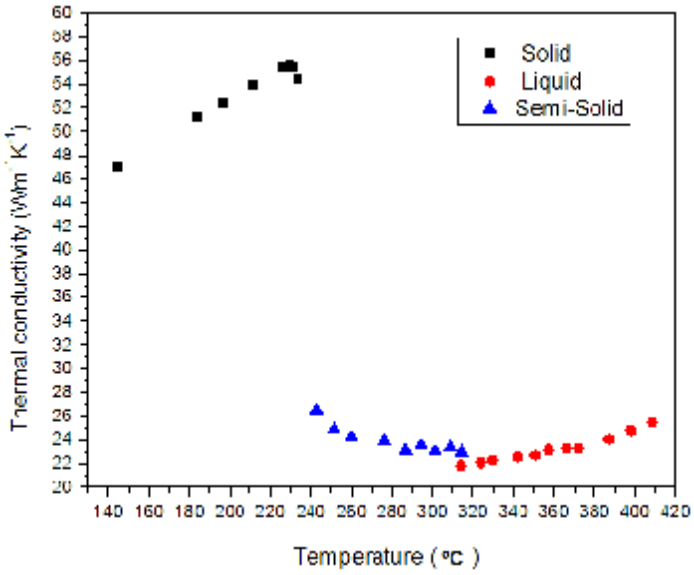

Figure 3-13 Estimation of thermal conductivity of Sn-7.5%Sb-3.5%Cu.

3.1.4 Heater Assembly

This assembly consists of two semi cylindrical shaped ceramic heaters, high temperature fiber insulation packages, heater and the insulation shroud and heater assembly stands as well as a cylinder that acted as the testing chamber in which the solid test metal was first placed and then heated until it was molten. Figure 3-14 shows the heater assembly with all of its parts.

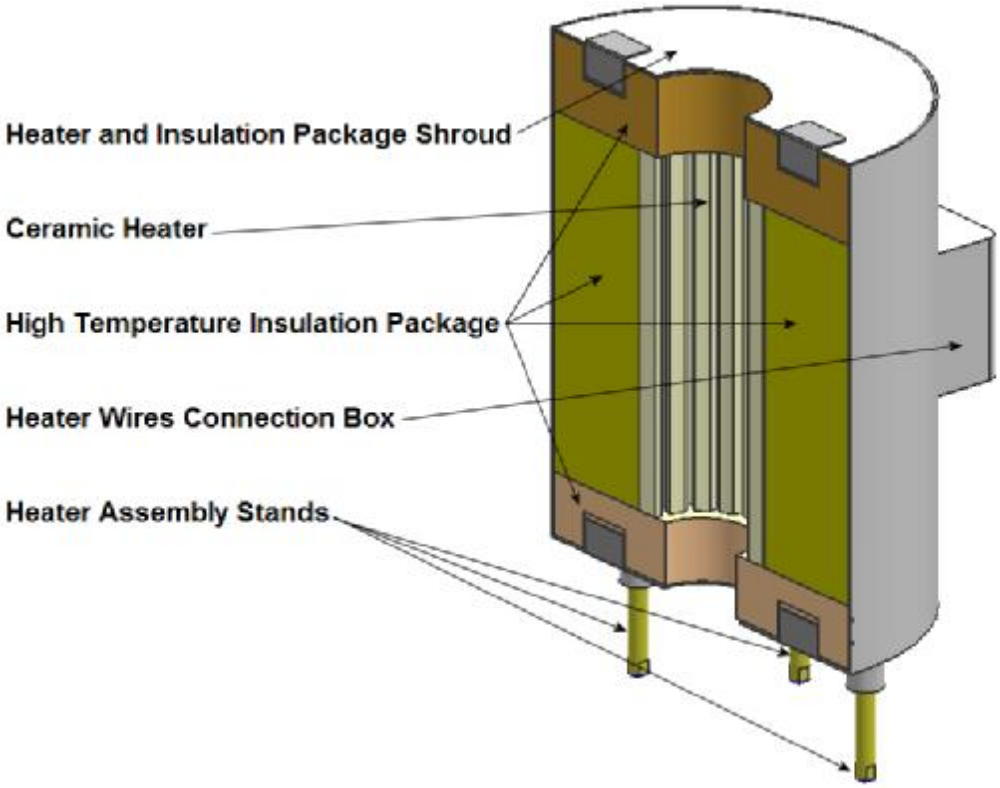

Figure 3-14 Heater assembly details.

3.1.4.1 Casting Chamber

Melting the metal and applying pressure by the piston will be done inside a casting chamber. The parts is a cylindrical shaped part with height of 352mm and O.D of 80 mm and I.D of 65mm. The part is made from H13 tool steel and it is heat treated to increase the hardness of the part to 53RC. Dimensions and sketches of the casting chamber are provided in Appendix B. The clearance between the piston and the inner diameter of the chamber was 0.051 mm to ensure there was no leakage during operation of the liquid metal up the side of the piston.

3.1.4.2 Ceramic Heaters and Insulation Package

To melt the test metal, two special semi cylindrical ceramic heaters were designed and ordered from ThermCarft Inc. located in Winston-Salem, USA. The dimensions of the heaters are 95mm I.D. X 250mm long with power of 1375 Watts and an input of 208V. Inside the heaters, Iron-Chrome-Aluminum wire was helically wound and placed in a grooved ceramic refractory holder. The coil was embedded with thermal conductive cement, to prevent it from growing out at the grooves due to thermal expansion when heated. The heaters are insulated by

employing high temperature Fibercraft insulation packages. This insulation mates well with Thermcraft High Temperature Electric Heaters. Three insulation packages were ordered and matched to insulate the heaters and the casting chamber to ensure that the heat flow in the test chamber and chill block would only occur in the y-direction (i.e. 1D). The dimensions are given as follows:

304.8mm O.D. x 14mm long insulation package which consists 127mm I.D. x 104.8mm O.D. x 355.6mm Long with vestibules on both ends which one vestibule is 57.15mm tick. The other vestibule is 44.45mm thick with a 73mm I.D thru hole.

There is a thermocouple embedded inside one of the semi cylindrical heaters which is shown in appendix B. The thermocouple is connected to a heater temperature controller. The heaters are also connected to the temperature controller box which turns the heaters on and off based on the set-point.

3.1.4.3 Heater and the Insulation Shroud

To keep the heaters and insulator package, a shroud in two halves, with 3 stands for each of them, was designed and built from aluminum alloy sheets and brass. The two halves are joined together for a test using two spring locks on either side. By employing the stands, It is possible adjust the height of the heaters (hot zone in the test chamber).

3.1.5 Pressure Assembly

To apply pressure on the sample and measure the temperature distribution values inside the molten metal, a piston piece was designed. The piston piece is a combination of four parts and two assemblies, namely: piston shaft, sealing piston, bushing, piston extension, LVDT assemblies and load cell assemblies.

3.1.5.1 Piston Shaft

The piston shaft is a connection from the load cell extension to the sealing piston and it delivers pressure from the piston shaft to the load cell. It is a 325mm long shaft with a diameter of 64mm, made from H13 tool steel. Figure 3-15 shows a sketch of the piston shaft.

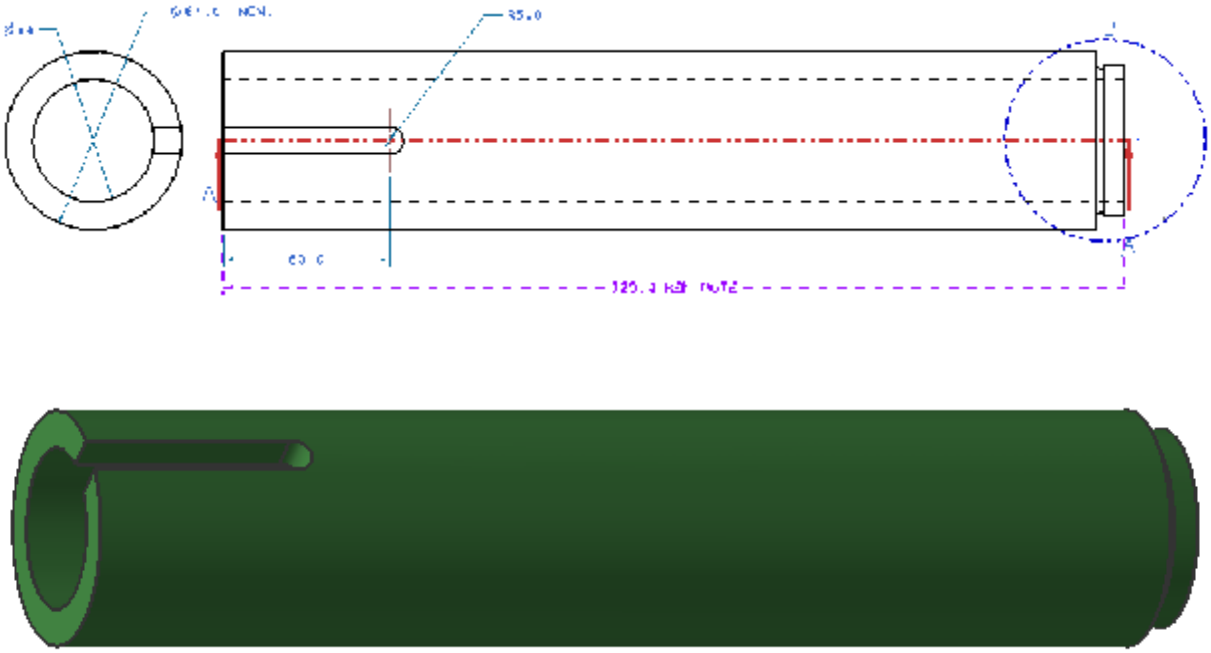

Figure 3-15 Piston shaft dimensions.

3.1.5.2 Sealing Piston

The sealing piston is a cylindrical shaped part with a height of 30mm and diameter of 64mm made from H13 tool steel. This part is used to seal the piston against the molten metal inside the cylinder when applying pressure by employing 3 piston rings and a clearance of 0.0508 mm between the piston and the cylinder. Figure 3-16 illustrates its architecture.

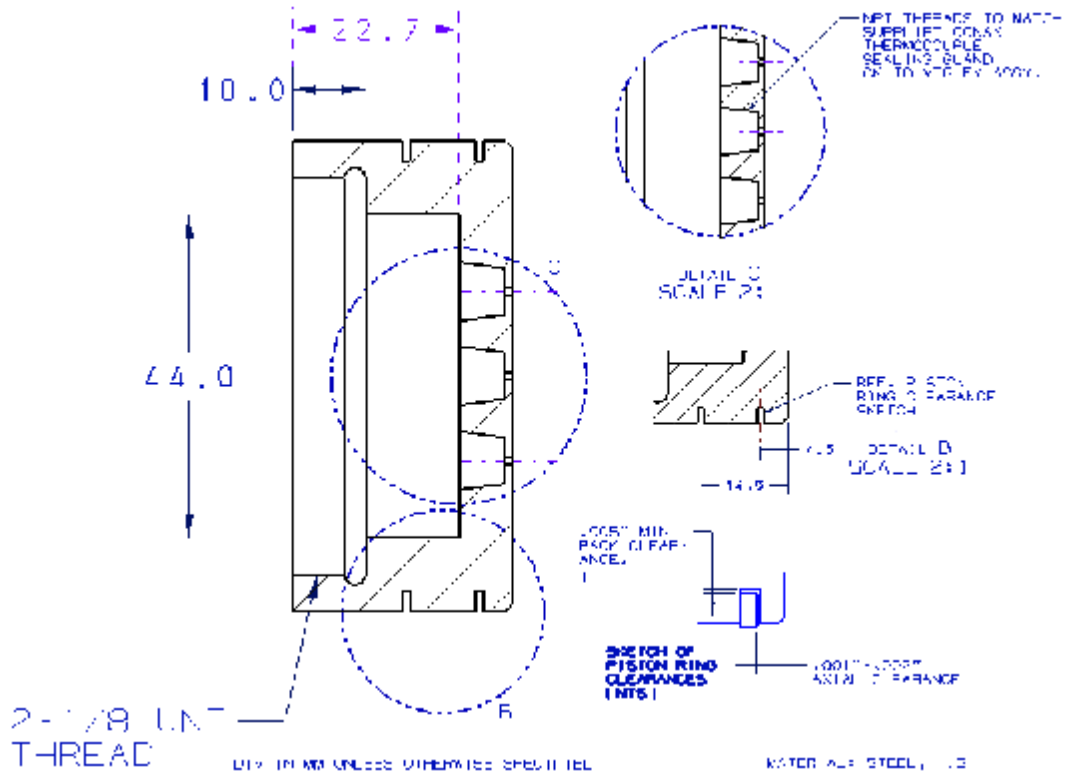

Figure 3-16 Sealing Piston dimensions.

Three sets of Wiseco alloy steel, ferrox coated, chrome faced rings were used to prevent the molten metal from leaking up the sides of the piston when applying pressure at the interface. The rings are installed in two grooves at the side of the sealing piston. Also 4 packing glands were installed inside the sealing piston to keep the thermocouples at the desired position under high pressure and temperature during each experimental test. One of these thermocouples was used to estimate the metal temperature at the interface of the metal and chill, two of the other TC's were used to measure the spatial distribution of the temperature in the test chamber and the fourth one was a backup thermocouple for future use. Figure 3-17 shows the sealing piston with the packing glands, thermocouples and the piston rings.

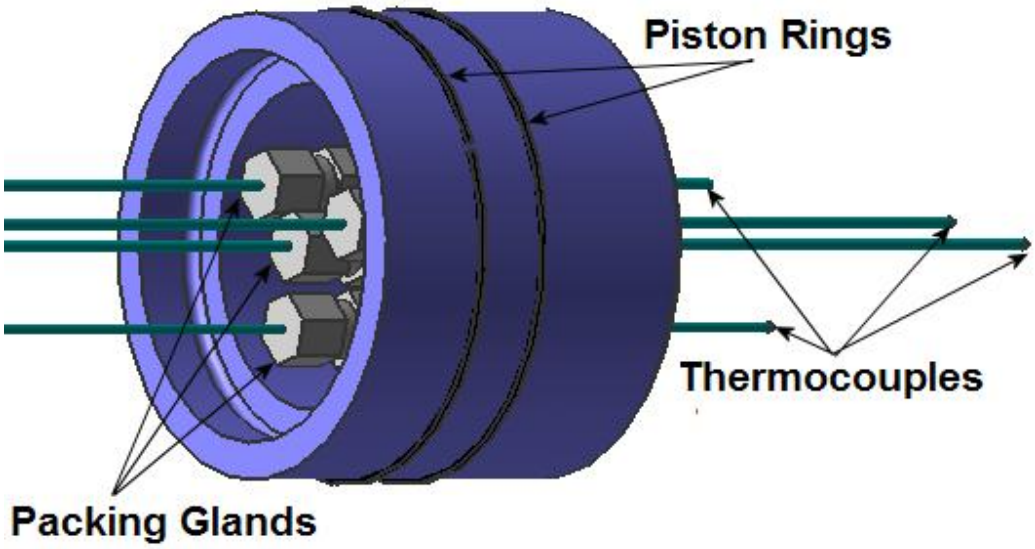

Figure 3-17 Sealing piston details.

Conax Packing Glands (PG) were used in this apparatus and they provide pressure/vacuum sealing for the thermocouples. Figure 3-18 shows different parts of a packing gland.

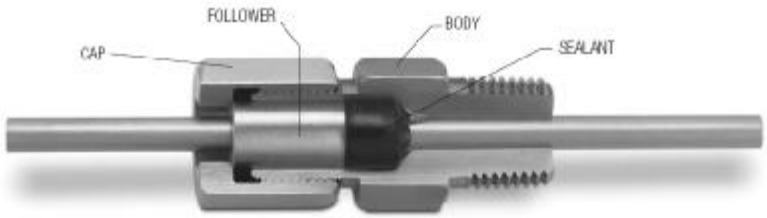

Figure 3-18 PG Packing Gland [66].

For this project, a packing gland with the bore size of 1.5mm was selected. The sealant was chosen to be Lava which is designed to work in high temperatures (-300° F to +1600° F (-185° C to +870° C)).

3.1.5.3 Bushing

The bushing part is a ring shaped part made from brass with an I.D. of 64 mm and O.D. of 100 mm. This part was mounted on the top plate to ensure that the piston shaft was positioned exactly in the middle of the cylinder and prevent any radial movement of the piston assembly, when applying pressure. Figure 3-19 illustrates dimensions and a view of the bushing part.

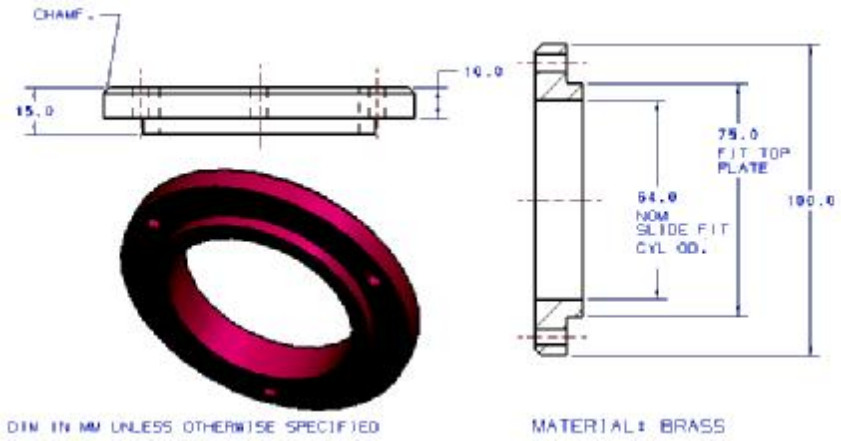

Figure 3-19 Bushing dimensions and details.

3.1.5.4 LVDT Assembly

To measure the displacement of the apparatus and to calibrate the position of the TC's at the start of the experiment, a DC operated LVDT was used. Figure 3-20 shows a complete view of the LVDT assembly and bushing.

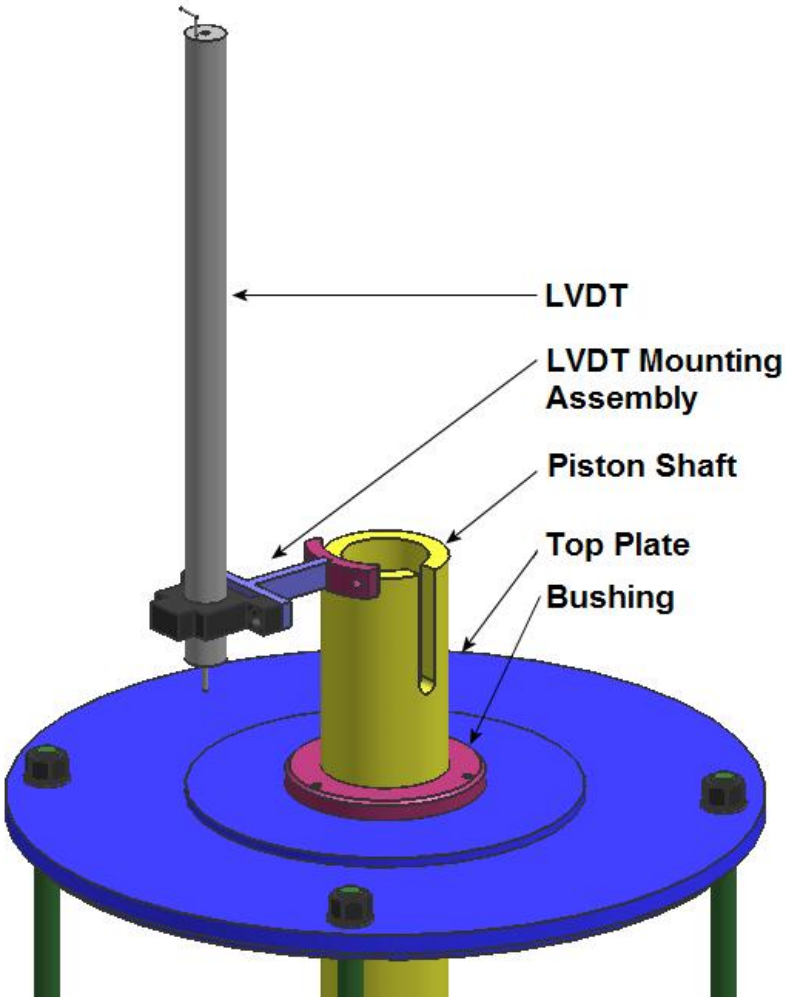

Figure 3-20 LVDT assembly and bushing details.

3.1.5.4.1 LVDT

Linear variable differential transformers (LVDT) are used to measure displacement. The LVDT is connected to the piston shaft by the LVDT mounting assembly which consists of an insulation material to prevent the heat to damage the LVDT and a holder which connects the LVDT to the piston shaft. The sensor of the LVDT is in contact with top plate and as the top plate is fixed, by applying pressure and moving the piston assembly, the LVDT will record the displacement of the piston shaft.

To measure the displacement of the piston during testing, a DC operated LVDT, DC-750-1250006 was used.

3.1.5.4.2 Piston Extension and Load Cell Assembly

To prevent heat going into load cell, a piston extension assembly was designed and built. As shown in Figure 3-21, the extension assembly consists of lower and upper extensions, made from H13 tool steel and a ceramic disk which is used as an insulator to minimize heat flow from the piston shaft to the load cell. The load cell is installed on the hydraulic universal testing machine upper head frame and it is in contact with the piston extension via an extension cap.

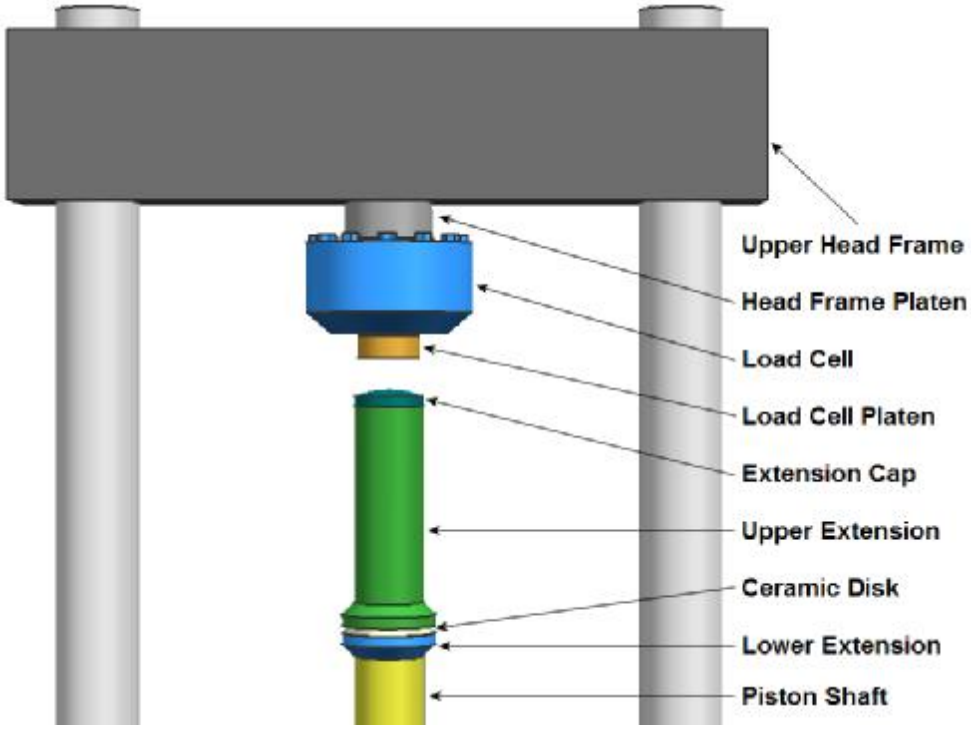

Figure 3-21 Piston extension and load cell assembly.

To measure the applied force, a load cell was employed. In this study the 1020AF interface load cell, shown in Figure 3-22 was employed. This device is a fatigue rated load cell with 300% overload protection, an extremely low moment sensitivity of 0.1%/in, low zero float (toggle) and a high fatigue life. The load cell, after calibration, was connected to the MTS 407 controller to read and analyze the load cell signals. More details about the load cell is provided in Appendix D.

Figure 3-22 Interface Load Cell 1020AF.

3.2 Load Assembly

To apply pressure, an Instron 1350 servo-hydraulic testing system with MTS 407 analog controller and equipped with a 12 kN load cell were employed These equipments are described in details in Appendix D.

3.3 Data Acquisition Equipment

To gather thermocouple, LVDT and the load cell data, a data acquisition system was used.

Figure 3-23 NI SCXI-1000 equipped with SCXI-1303, 32 Channel Terminal.

In this study a SCXI-1303 Terminal, a SCXI-1102 T.C. Amplifier and a SCXI-1000 Chassis were used, shown in Figure 3-23 NI SCXI-1000 equipped with SCXI-1303, 32 Channel Terminal. The chassis provide power, controls the SCXI bus and houses the modules. Terminal blocks provide a quick and suitable way to connect I/O signals to the system. The plug-in DAQ device was employed to gather the signals from the SCXI system into the PC.

The final part of the SCXI system is its software. In this study, LabVIEW software is used. LabView (Laboratory Virtual Instrumentation Engineering Workbench) is a platform and development environment for a visual programming language from National Instruments which uses icons instead of text to develop applications. It employs data flow programming similar to a flowchart to create an application and is used as an interface between the computer and SCXI system.

3.4 Thermocouples

One of the challenges in designing the experimental apparatus is to account for the response of the TC's. For each TC, a thermal time constant exists which is the initial thermocouple temperature to reach a value of 63.2% of the steady state condition of the actual temperature. The size of the thermocouple assembly and thermocouple wires are important factors affecting the thermal time constant [10].

The thermocouples used in this study have a thermal time constant of less than 1 second. The type-K (Chromel-Alumel) grounded thermocouples with rugged junction were used to measure the temperature history in the chill and test metal. The TC's were sheathed in Nickel-Chrome Based Super Omega Clad with ultra high temperature mineral insulated with excellent long term stability at high temperature for use up to 1335 ºC with excellent resistance against oxidation, carburization and chlorination resistance. The length of thermocouples was 30cm with a diameter of 1.5mm. Figure 3-24 shows a sketch of the test thermocouple.

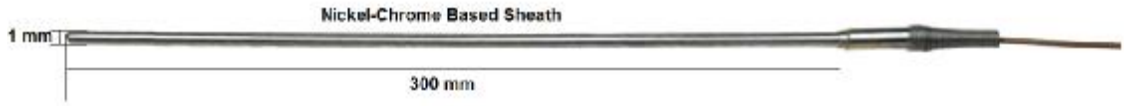

Figure 3-24- Chromel Alumel K-type thermocouple.

3.5 Experimental Procedure

In order to test the effect of different parameters, the following procedural steps were executed for each experiment:

1. The chill block was inserted on the cooler assembly.
2. Two thermocouples were installed in to the chill.
3. The test metal is placed into the casting chamber against the chill block. A high temperature parting agent is applied on the inner sides of the test chamber to ensure that the test metal can be easily removed after a test.
4. Heaters are placed around the casting chamber and their height adjusted as required.
5. Tightening of the four rods on the main lower plate.
6. Placement of the upper plate on the casting chamber and tightening the upper rod nuts.
7. Installation of the thermocouples inside the piston and tightening the packing glands.
8. Connection of the piston to the load cell.
9. Turning on the heaters and setting the heater controller to reach the desired temperature.
10. Turning on the pressure setup and setting the desired displacement to put the piston thermocouples in place.
11. Turing on the water circulation to adjust the temperature of the chill assembly
12. Attaching thermocouples, LVDT and load cell to the PC via the data acquisition system and start of the LabView software.
13. After the test metal has reached the desired test temperature, moving the setup to put the piston thermocouples in place.
14. Turning off the heaters and starting the software to measure the temperature distributions.
15. To test the effect of the pressure on the heat transfer coefficient values, steps 18 and 19 should be followed.
16. Installing the pressure shaft on the piston and installing the pressure connection on the load cell.
17. The pressure can be applied at this step and the LVDT will measure the displacement of the piston and the thermocouples.
18. After solidification of the metal, heaters are turned on again to re-melt the material and remove the piston and the thermocouples from the metal.
19. The recorded temperature time histories are analyzed using an Inverse Transfer Procedure described in Chapter 4.

Chapter 4 Inverse Heat Conduction Model

In order to calculate the associated heat flux and heat transfer coefficient for each test performed, it was necessary to develop a one-dimensional Finite Difference (FD) mathematical model capable of solving the governing heat conduction equation associated with the inverse heat flux analysis. This method assumes an initial heat flux at the surface of the sample and then compares the predicted temperature distribution within the sample to that which was measured by the thermocouples. The heat fluxes are then adjusted and the analysis run again to determine the new temperature profile. This process is performed iteratively until the difference between the predicted and measured temperatures meet the accuracy requirement (1°C).

4.1 Formulation of the Inverse Problem

To analyze the experimental results and calculate parameters such as heat flux, surface temperatures, and heat transfer coefficients at the metal-chill interface, shown in Figure 4-1, an inverse heat conduction (IHC) code was developed. The IHC problem is much more difficult to solve than a direct heat conduction problem. One of the reasons for this is because this type of problem is extremely sensitive to measurement errors and the use of small time steps frequently introduces instabilities in the solution of the IHC problem unless regularization are employed.

The procedure used was developed by employing a numerical solution to calculate the temperature profiles and the heat flux entering the chill. As shown in Figure 4-1, two thermocouples, Thermocouple 1 (TC1) and Thermocouple 2 (TC2), were used to measure the temperature profiles inside the chill block for further analysis using the IHC code. Also, to calculate the surface temperature of the metal cast section, Thermocouple 3 (TC3) was used. By having the measured temperature history of Thermocouple 3 (TC3) and the heat flux at the metal/chill interface, calculation of the surface temperature of the casting and hence heat transfer coefficient (HTC) and the metal/chill interface is possible.

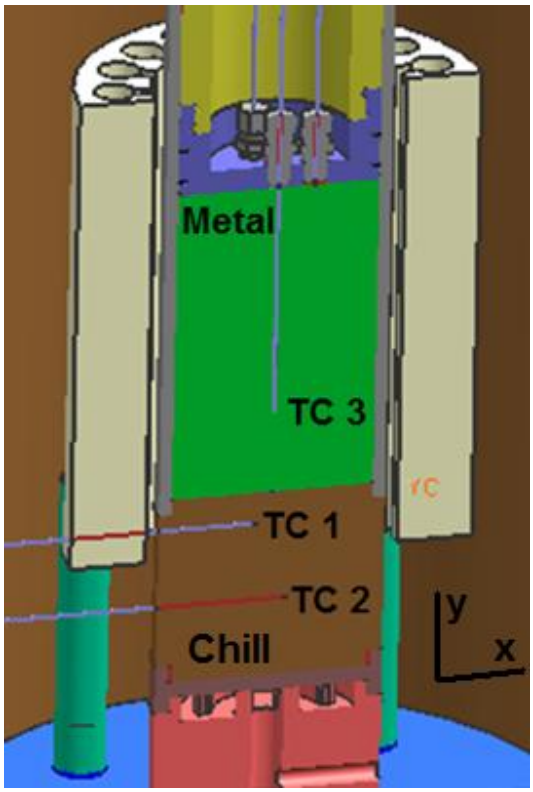

Figure 4-1 X-sectional view of the experimental apparatus showing relative thermocouple locations as well as metal and chill parts.

4.2 Development of 1-D Heat Conduction Model

4.2.1 Basic Heat Transfer Problem

To analyze the heat transfer which occurs in the chill material which is exposed to the hot liquid metal, a one-dimensional thermal heat transfer analysis was viewed sufficient as the majority of the heat was conducted through the chill in the y-direction towards the metal and chill at the interface as shown schematically in Figure 4-1. Since the thermocouples were located in the middle of the chill and the cylinder was well insulated, we did not consider heat flow across the width of the sample in the x-direction. The governing partial differential equation (PDE) for heat conduction in one dimension is:

$$\frac{1}{\alpha}\frac{\partial T}{\partial t} = \frac{\partial^2 T}{\partial y^2} \tag{4.1}$$

Where $\alpha = \frac{k}{\rho C_p}$ is the thermal diffusivity of the solid $(\frac{m^2}{s})$, T is temperature (K), t is time (s), C_p is specific heat (J/kg.K), k is thermal conductivity (W/m.K), ρ is density (kg/m³), and y is in the vertical direction. The governing equation shown in Equation 4.1 is subject to the following initial condition and BC's outlined below.

Assuming that the test metal starts at a uniform temperature T_0, the initial condition is:

$$T(y) = T_0 \tag{4.2}$$

4.2.2 Boundary Conditions

Referring to Figure 4-2, at y = 0, (the interface of the test metal and the chill), the boundary condition (BC1) was defined as shown in equation (4.3) and at y = - 45mm, boundary condition (BC2) was defined as equation (4.4) which is a known temperature history recorded by thermocouple 2 (TC2).

$$-k \frac{\partial T}{\partial y} = q(0, t) \tag{4.3}$$

$$T(y = -45mm, t) = TC2 \tag{4.4}$$

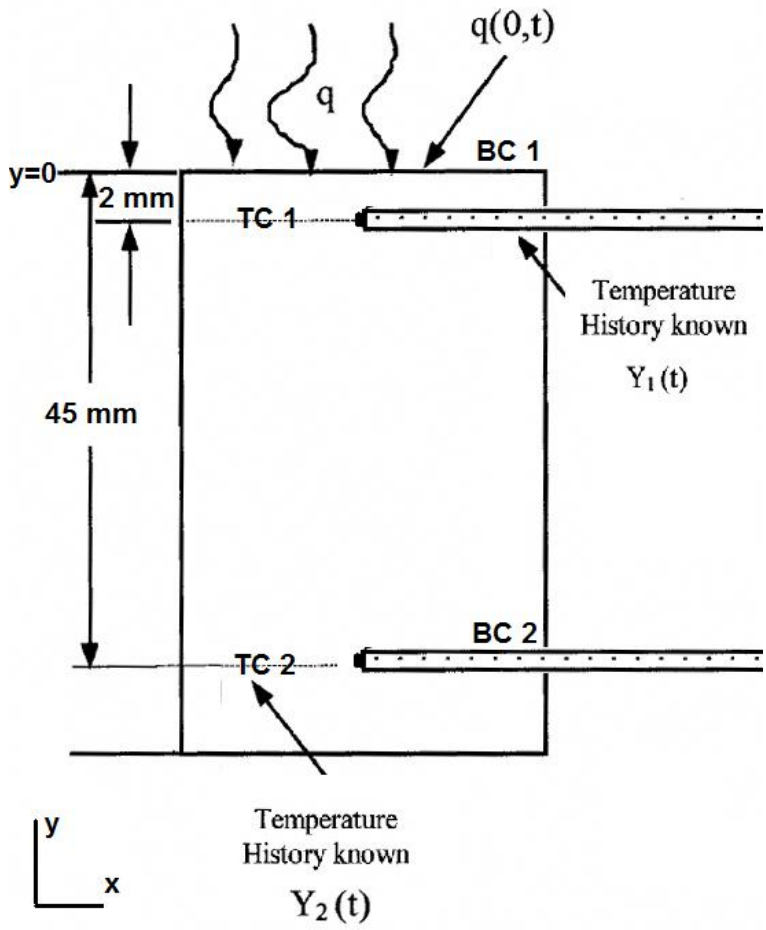

Figure 4-2 Schematic of the chill showing boundary conditions used in the model.

As shown schematically in Figure 4-3, in the test metal at y=0 boundary condition (BC1) was defined as equation (4.3) and at y=2 mm, boundary condition (BC2), is given by equation (4.5) and is the known temperature history recorded by thermocouple 3 (TC3).

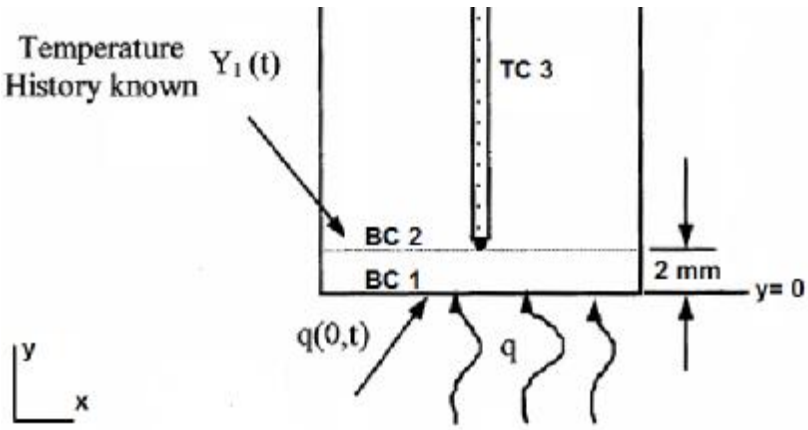

Figure 4-3 Schematic of the test metal showing boundary conditions used in model.

$$T(y = 2mm, t) = TC3 \tag{4.5}$$

where q is heat flux at the interface between the chill/metal. Also TC1 and TC3 are the temperature histories, measured by Thermocouple 1 (TC1) and Thermocouple 3 (TC3) inside the chill and test metal.

To solve Equation (4.1), an implicit Finite Difference (FD) numerical technique was used However, to estimate the initial value for the heat flux at the start of the program for the implicit code, an explicit code was developed which is described in section 4.3.3.

To utilize the implicit FD method, a domain from the interface of the metal-chill to thermocouple 2 (TC2) was divided into a number of elements as shown in Figure 4-4 in which interior nodes are shown by "l" and the exterior node is shown by "k".

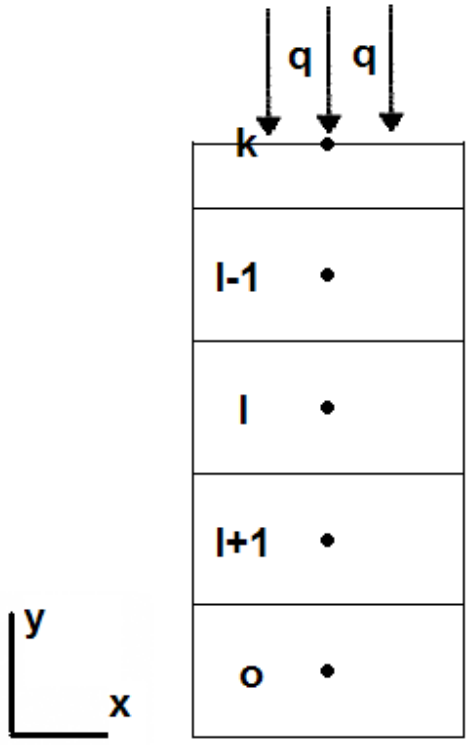

Figure 4-4 Finite Difference descritization of the chill.

By utilizing the boundary conditions for the problem, Equation (4.6) can be developed.

$$\frac{1}{\alpha}\frac{T_l^{t+1}-T_l^t}{\Delta t}=\frac{T_{l+1}^{t+1}+T_{l-1}^{t+1}-2T_l^{t+1}}{(\Delta y)^2} \tag{4.6}$$

where the subscript *l* shows spatial location and superscript *t* refers to the time step.

Also using the heat flux boundary condition (4.3)(4.1) in Equation (4.6), the surface node "k" can be described by Equation (4.7).

$$\rho\frac{\Delta y}{2}C_p\frac{T_0^{t+1}-T_0^t}{\Delta t}=k\frac{T_1^{t+1}+T_0^{t+1}}{(\Delta y)^2}+q_0 \tag{4.7}$$

By utilizing Equation (4.6) and (4.7) and having q at node "K" and temperature history at node "O", recorded by thermocouple 2 (TC2), as the boundary conditions of the problem, the temperature distribution inside the medium was calculated.

4.2.3 Comparison of FD Model Predictions to an Analytical Solution

Verification of the one-dimensional heat transfer FD model was done by comparing the model solution to an analytical solution for a semi-infinite solid with a uniform initial temperature, T_i which is suddenly exposed to a constant surface heat flux q_0. A parametric study was performed to find the best values of the time step and element size in the FD method.

Equation (4.8) shows the analytical solution for the temperature distribution profile of the domain by applying a constant value of heat flux [15].

$$T(y,t)=2q_0\frac{(\frac{\alpha t}{\pi})^{0.5}}{k}\exp\left(\frac{-y^2}{4\alpha t}\right)-\frac{q_0 y}{k}\operatorname{erfc}\left(\frac{y}{2\sqrt{\alpha t}}\right)+T_0 \tag{4.8}$$

Where q_0 is the constant value of heat flux (W/m^2), y is the location in the chill (m), t is time (s), k is thermal conductivity (W/m.K) and T_0 is the initial temperature of the chill (K). Figure 4-5 shows the predicted temperature distribution using the analytical solution and a constant surface heat flux of 200 kW/m^2 and material properties for a H13 steel, given in Chapter 3.

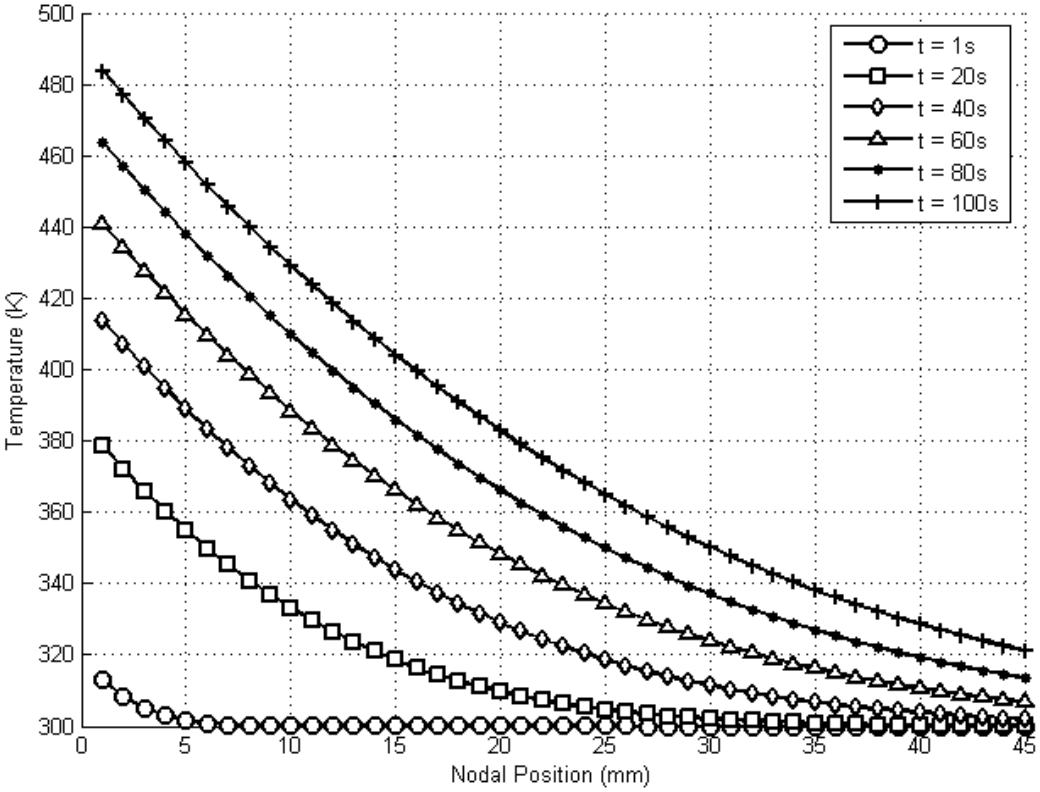

Figure 4-5 Predicted temperature distribution using the analytical solution given in equation (4.8) and a constant surface heat flux of 200 kW/m^2

A sensitivity study was performed to determine the effect of different element size and time step on the predicted results using the implicit FD code. Figure 4-6 (a) shows the results of the sensitivity study by employing different time step values (t = 0.01s, 0.1s, 1s, 5s, and 10 s) while $\Delta y = 0.5mm$.

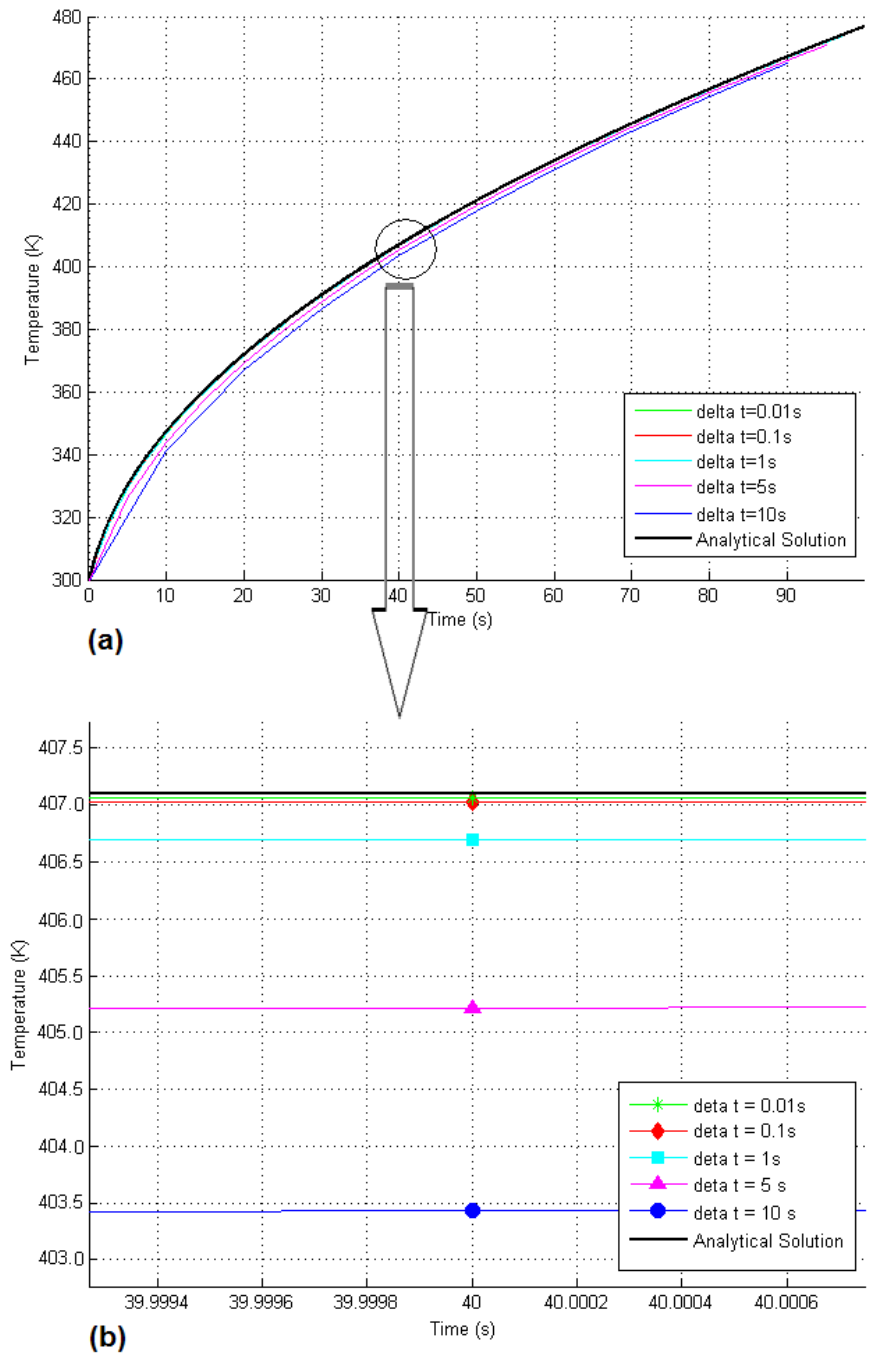

Figure 4-6 (a) Numerical Vs. Analytical solution at 2mm below the chill and metal interface for Δy = 0.5mm.. (b) A blow-up at t=40s.

Figure 4-6 (b) shows the comparison of analytical solution values and numerical solution values at t= 40s which illustrates that after decreasing the time step value to less than 0.1s, the temperature estimation by the inverse code is accurate to within 0.001°C (0.1%).

Table 4-1 shows a comparison between the results of the analytical solution and the finite difference model results after a time period of 100 seconds.

Table 4-1 Comparison of analytical solution and FD solution results at 2mm below the interface (Error %).

q=200 kW/m², Δy=0.5mm					
Time(s)	Δt=10s	Δt=5s	Δt=1s	Δt=0.1s	Δt=0.01s
10	13.63157319	6.124323	1.096791	0.114979	0.019404
20	8.307791549	3.820561	0.726119	0.079599	0.015839
30	6.135139563	2.90724	0.56597	0.064295	0.014595
40	4.975635193	2.395236	0.472727	0.055527	0.0141
50	4.236333066	2.059316	0.410674	0.05002	0.014153
60	3.713300704	1.817778	0.366123	0.046695	0.01489
70	3.316925378	1.63288	0.332535	0.059583	0.016483
80	3.001251972	1.484616	0.306362	0.060378	0.019022
90	2.740303315	1.361475	0.285515	0.06291	0.022503
100	2.51841557	1.25647	0.268681	0.048799	0.026855

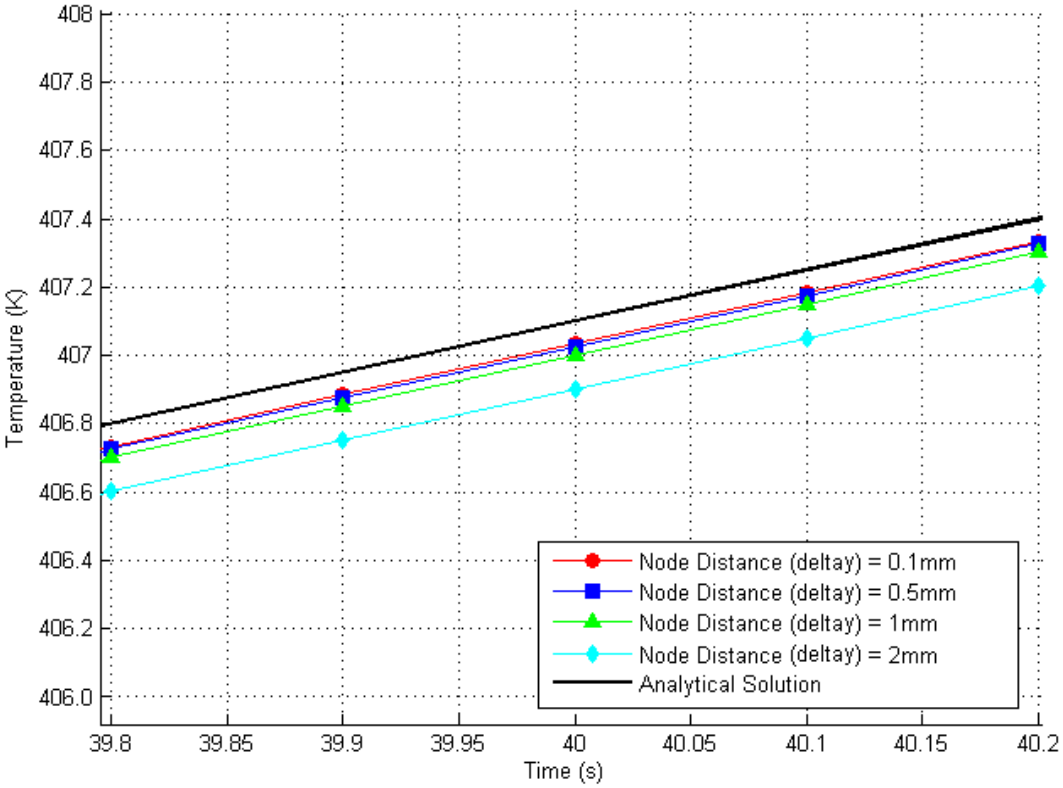

Figure 4-7 Numerical Vs. Analytical Solution at 2mm below the chill and metal Interface at t=40s for $\Delta t = 0.1$.

Figure 4-7 shows a comparison of analytical solution values and numerical solution values at t= 40s, which illustrates that by decreasing the nodal distance (Δy) value to less than 0.5 mm, the temperature estimation by the implicit FD code is within 0.1% percentage of that predicted by the analytical solution.

Table 4-2 Analytical solution and FD numerical solution results at 2mm blow the interface (Error %).

q=200 kW/m2, Δy=0.1s				
Time(s)	Δy=0.1mm	Δy=0.5mm	Δy=1mm	Δy=2mm
10	0.1106348	0.11497909	0.12857555	0.26961391
20	0.07670132	0.07959888	0.08866075	0.18215283
30	0.06203386	0.06429538	0.07136379	0.14415092
40	0.05359574	0.05552665	0.06151521	0.12285796
50	0.04812925	0.05001971	0.05564443	0.11164147
60	0.04443423	0.04669497	0.05281684	0.1093603
70	0.0419645	0.05958267	0.05276948	0.11588393
80	0.04042394	0.06037758	0.05533692	0.1308322
90	0.03962354	0.06291011	0.06029864	0.15341027
100	0.03942568	0.04879883	0.06737175	0.18255609

Table 4-2 shows a comparison between the results of the analytical solution and the FD numerical solution.

From the presented information, it can be concluded that by choosing $\Delta x \leq 0.5\text{mm}$ and $\Delta t \leq 0.1\text{s}$ the heat transfer calculations in the implicit FD code are of the highest level of accuracy.

4.3 Mathematical Techniques Used in IHC

4.3.1 Inverse Heat Transfer Analysis

The heat flux and the HTC at the interface between the metal and chill block were calculated using an inverse analysis technique. Using this technique, an initial heat flux is assumed at the interface and the finite difference method is used to calculate the resulting temperature distribution in the chill. After the calculated temperature distribution is obtained, it is compared with the temperature distribution measured in the chill and hence heat fluxes are adjusted iteratively so that the difference between the measured and calculated temperatures at each thermocouple position is minimized. The difference between the measured and calculated temperatures at TC1 at the current time step was evaluated and minimized by using the quadratic fit line search method as described below. Then the calculated temperature will be used as the initial temperature for the next time step and the corresponding surface heat fluxes will be used as the starting heat fluxes for the next time step.

After employing the initial estimation of the heat flux, the temperature profiles at location y_1, the position of thermocouple 1 (TC1), were modeled (T_{m1}). The estimated heat flux at each time step was evaluated by utilizing a least square method to compare the modeled temperatures with the measured temperatures which is shown by equation (4.9) and minimizing it by using the quadratic fit line search method.

$$F(q) = \sum_{i=1}^{r} (T_{m1t} - TC1_t)^2 \tag{4.9}$$

$Tm1_t$ and $TC1_t$ are the modeled and calculated temperatures at the location of thermocouple 1 (TC1). r is the future number of temperature measurements in the inverse heat conduction process. The value r is an integer between 1, 2, 3, or 4. In this study r=4 was employed.

At each iteration of the time step, a new value for the heat flux is estimated and utilized to calculate a new set of modeled temperatures. By employing the least square function and comparison of the measured temperatures with the modeled temperatures, the new value of the least square function was calculated. This process was repeated until the minimum value of the function for each time step was found.

4.3.2 Quadratic Fit Line Search Method

To accelerate minimization of equation (4.9), a quadratic line search method was employed. At each time step, plotting the least square function versus the values of the estimated heat flux shows parabolic behavior. To employ this method, three different heat flux values were used to calculate the values of the least square function; Assume that $(\lambda_1, \lambda_2, \lambda_3)$ are the first estimates of heat flux at the beginning of the each time step. Because of the parabolic behavior of the least square function, $f(\lambda) = a\lambda^2 + b\lambda + c$ and by having the $\lambda_1, \lambda_2, \lambda_3$ the unique minimum of this function is :

$$\hat{\lambda} = \frac{(\lambda_2^2 - \lambda_3^2)f(\lambda_1) + (\lambda_3^2 - \lambda_1^2)f(\lambda_2) + (\lambda_1^2 - \lambda_2^2)f(\lambda_3)}{2[(\lambda_2 - \lambda_3)f(\lambda_1) + (\lambda_3 - \lambda_1)f(\lambda_2) + (\lambda_1 - \lambda_2)f(\lambda_3)]} \tag{4.10}$$

After calculating $\widehat{\lambda}$, to update the new values of the heat flux estimations, the following procedure was followed:

If $\hat{\lambda} > \lambda_2$ and f ($\widehat{\lambda}$) > $f(\lambda_2)$ the new values of the estimated heat fluxes are ($\lambda_1, \lambda_2, \hat{\lambda}$).

If $\hat{\lambda} > \lambda_2$ and f ($\widehat{\lambda}$) < $f(\lambda_2)$ the new values of the estimated heat fluxes are ($\lambda_2, \hat{\lambda}, \lambda_3$).

If $\hat{\lambda} > \lambda_2$ and f ($\widehat{\lambda}$) = f(λ_2) the new values of the estimated heat fluxes are either of the above:

If $\hat{\lambda} < \lambda_2$ similar to above but If $\hat{\lambda} = \lambda_2$, the quadratic search method has failed to produce a new point, in this case:

If $\lambda_3 - \lambda_1 \leq \epsilon$ = positive tolerance then λ_2 should be selected as the best point, which in this study is 50, and finally:

$$\text{If } \lambda_3 - \lambda_1 > \epsilon, \hat{\lambda} = \begin{cases} \lambda_2 + \frac{\epsilon}{2} \text{ if } \lambda_2 - \lambda_1 < \lambda_3 - \lambda_2 \\ \lambda_2 - \frac{\epsilon}{2} \text{ if } \lambda_2 - \lambda_1 > \lambda_3 - \lambda_2 \end{cases}$$

At the end of this procedure, f ($\widehat{\lambda}$) should be computed and all the above steps should be repeated until max | $\hat{\lambda} - \lambda_2$| becomes smaller than 1 °C.

At the end of the IHC technique, the best heat flux estimation at each time step, which minimums the least square function, was used to estimate the metal surface temperature (T_{MS}).

4.3.3 Procedure to Estimate First Heat Flux Value

To estimate the first values of the heat flux and enter it as the first value of heat flux, a computer code was developed.

This procedure is applied on the same domain, illustrated by Figure 4-2 and Figure 4-3. By employing an explicit method and the least square function method, it estimates the first value of the heat flux.

In this procedure, the future temperature of each node is calculated by using the current temperature of the nodes and employing equation (4.11) which is the explicit finite difference approximation of the one dimensional problem.

$$\frac{T_{l+1}^{t} - 2T_{l}^{t} + T_{l-1}^{t}}{(\Delta y)^2} = \frac{1}{\alpha}\frac{T_{l}^{t+1} + T_{l}^{t}}{\Delta t} \qquad (4.11)$$

where t, is time step, l is the position of the interior nodes, Δy is the nodal spacing, and α is the thermal diffusivity ($\frac{m^2}{s}$) of the chill material.

By solving equation (4.11) for an interior node at location l and time step t+1, temperature of the node, T_l^{t+1} , will be calculated by :

$$T_l^{t+1} = \frac{\alpha \Delta t}{(\Delta y)^2}(T_{l+1}^t + T_{l-1}^t) + T_l^t\left(1 - 2\alpha\frac{\Delta t}{(\Delta y)^2}\right) \quad (4.12)$$

and for the interface node, k,

$$T_k^{t+1} = T_k^t - \frac{2\alpha \Delta t}{(\Delta y)^2}(T_{k+1}^t - T_{k-1}^t) + \left(2q\frac{\Delta t}{(\Delta y \rho c)}\right) \quad (4.13)$$

Where ρ is density (kg/m³) of the material, Δy is the domain node's spacing (mm), Δt is time interval (s), c is the heat capacity (J/kg.K) of the material and α is the thermal diffusivity $(\frac{m^2}{s})$ of the material.

To stabilize the explicit finite difference method,F_0 , the Fourier number should be less or equal to 0.5 which $F_0$is defined as : $F_0 = \alpha \Delta t/(\Delta y)^2$

For the fixed value of $\Delta y = 0.5mm$, a suitable value of Δt was chosen to ensure stability.

Similar to the previous implicit FD method described, the measured temperature profiles by Thermocouple 1(TC1) were used as matching parameter to minimize the least square method and estimate the best value of the heat flux, while, the measured values by Thermocouple 2 (TC2) were employed as a boundary condition.

In this method, the least square function method and an iterative procedure was employed by utilizing the Taylor series expansion at each time step.

$$T_{n+i}^{r+1} \approx T_{n+i}^r + \frac{\partial T_{n+i}^{t+1}}{\partial q_{lm}^{t+1}}(q_m^{r+1} - q_m^r) \quad (4.14)$$

where r is the iteration step and $\frac{\partial T_{n+i}^{t+1}}{\partial q_{lm}^{t+1}}$ is the sensitivity coefficient calculated as:

$$\phi_i^r = \frac{T_{n+i}\left(q_m^r(1+\varepsilon)\right) - T_{n+i}(q_m^r)}{\varepsilon q_m^r} \quad (4.15)$$

$T_{n+i}\left(q_m^r(1+\varepsilon)\right)$ is the estimated temperature profile by applying q= $q_m^r(1+\varepsilon)$ and $T_{n+i}(q_m^r)$ is the estimated temperature profile by applying q= q_m^r in the finite difference procedure. The ε is a small value, taken as 0.01, in the iterating process. Minimizing the least square function, at each time step, achieved by calculation the derivative of F(q) with respect to q and equalize it to zero which gives

$$-2\sum_{i=1}^{r}(Y_{n+i}-T_{n+i})\frac{\partial T_{n+i}}{\partial q}=0 \tag{4.16}$$

where, Y_{n+i} is the modeled temperature values at each time step and T_{n+i} is the measured temperature values by the Thermocouple 1(TC1).

Finally, ∂q was calculated by introducing equation (4.9) to equation (4.13).

$$\partial q_m^{r+1}=\frac{\sum_{i=1}^{r}(Y_{n+i}-T_{n+i})\phi_i^r}{\sum_{i=1}^{r}(\phi_i^r)^2} \tag{4.17}$$

At each time step, the new heat flux value is estimated by adding ∂q of the current iteration to the previous estimated of heat flux value.

$$q_m^{r+1}=q_m^r+\partial q_m^{r+1} \tag{4.18}$$

This process will be repeated until

$$\frac{\partial q_m^{r+1}}{q_m^r}\leq 0.005 \tag{4.19}$$

After calculating the best value of the heat flux at each time step, q_m^r , which is satisfy the convergence criterion, is used as the best heat flux for the next time step m+1. Convergence criteria of 0.005 is a common value for this method [36].

4.3.4 Heat Transfer Coefficient

To calculate the heat transfer coefficient, the heat flux and the chill surface temperatures were employed. It is assumed that the heat flux entering the chill from the interface of the casting and the chill is identical to the heat flux exiting the casting part to the chill part via their

interface. This method is suggested by Ho and Pehlke [41], as well as Muojekwu et al. [31]. For this reason, the estimated values of the heat flux, calculated by the IHC technique, were used to model the heat transfer and interface surface temperature of the metal at the interface by utilizing the estimated heat fluxes and applying these at the boundary using the implicit FD method in the forward problem. The relationship between the heat flux, measured temperatures at the position of the Thermocouple 3 (TC3), and conductivity of the metal is described by

$$q = -k \frac{(T_{surface} - TC3)}{y_3} \tag{4.20}$$

where q is the heat flux entering to the chill from the melt or cast side (W/m²), k is conductivity of the metal (W/m.K), x_3 is distance between surface and TC3 (m), and $T_{surface}$ is the surface temperature of the interface of the metal and chill at the casting side (K). By having the heat flux, and the surface temperatures of the metal and chill block, the heat transfer coefficient can be calculated by equation (4.21).

$$h = \frac{q}{(T_c - T_m)} \tag{4.21}$$

where h is the heat transfer coefficient (W/m²K), q is the heat flux (W/m²), T_c is the surface temperature of the cast side (K), and T_m is the surface temperature of the chill part (K).

4.3.5 IHC Procedure

By employing the mentioned methods and formulations, a numerical code was developed to calculate the heat transfer coefficient. This code utilizes the temperature profile distribution obtained from the three thermocouples inside the chill and the metal part. Figure 4-8 schematically represents the algorithm of the inverse heat conduction procedure used to run the inverse code.

In the first step, the thermo-physical properties of the chill, casting alloy and the measured temperature distribution profiles by TC1 and TC2 were introduced to the explicit code to find a proper heat flux estimation. After finding the proper estimation for the first value of heat flux, control volume size, time step, temperature distribution profiles, convergence criteria and total number of time steps were set to the main inverse code. In the next step, the measured temperature profiles by TC1 and TC2 from the current time step were entered into the code. In

the next time steps, the temperature profile was estimated from the previous time step's temperature profile and heat flux.

At each time step, by employing the calculated heat flux of the previous time step, a new temperature distribution profile was calculated and compared with the experimental values for TC1. The least square function was calculated by equation (4.9) and by employing the Quadratic Fit Line Search Method a new optimal value for the heat flux was calculated and these steps were repeated until the convergence criteria was met. After finding the best value for the heat flux at each time step, the temperature distribution of the chill, by employing the heat flux value, was calculated and saved in to the output file. This process was repeated for all time steps.

To calculate the heat transfer coefficient, the chill surface temperature was taken from the previous steps as the value of the node 1 at the surface. The value for the casting surface temperature is determined by employing equation (4.20) and using experimental results of TC3. Finally, by having heat flux, chill surface temperature and casting surface temperature for each time step, the heat transfer coefficient is calculated using equation (4.21).

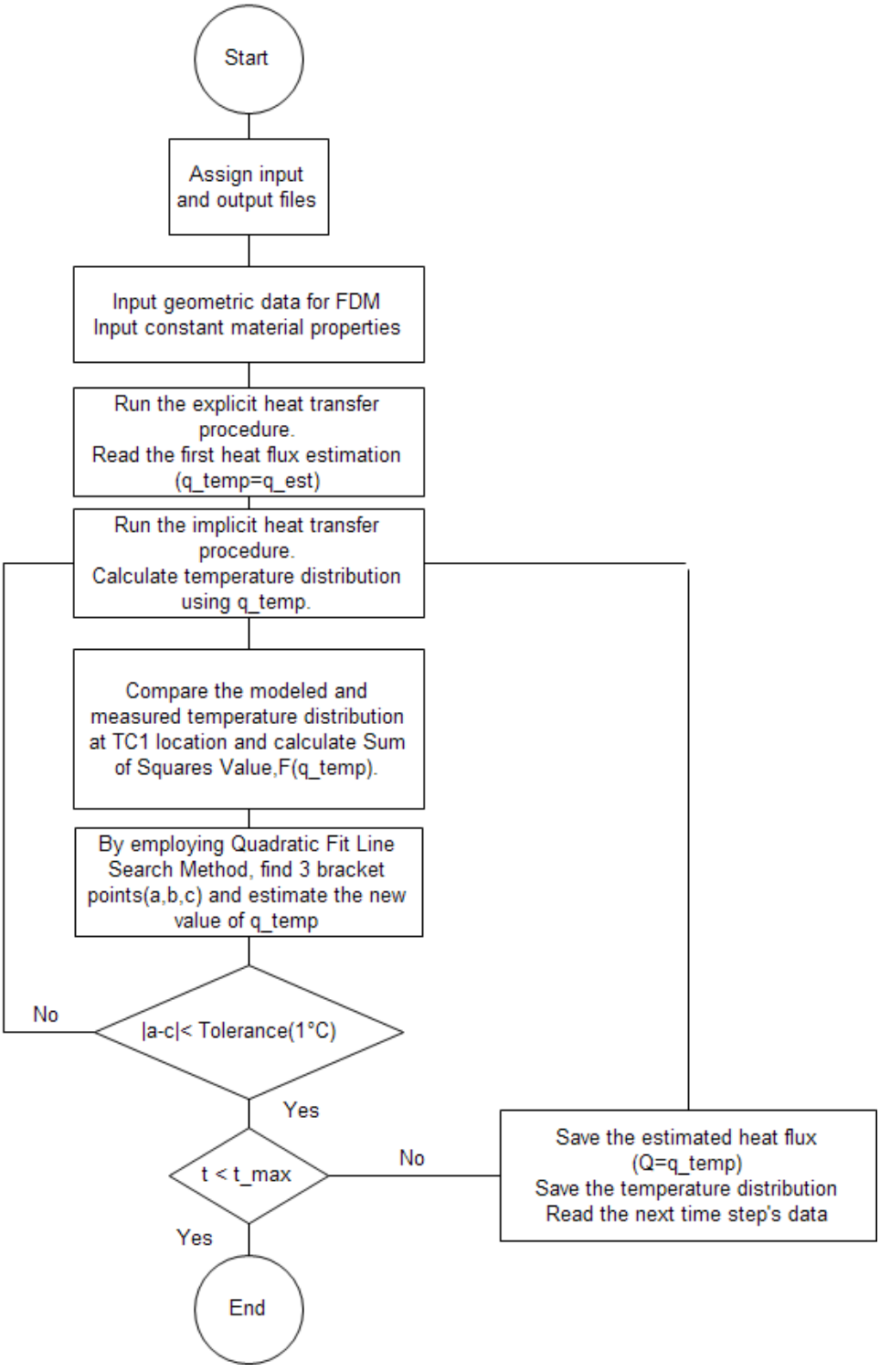

Figure 4-8 Flowchart indicating how the Inverse Heat Conduction Model works.

4.4 Validation of IHC Method

Before analyzing the results of the inverse code, it was essential to check the integrity of the IHC method. To validate the code's result, the commercial software package FEMLAB was utilized.

FEMLAB (Finite Element Modeling Laboratory) is an advanced software package for the modeling and simulation of any physical process described by partial differential equations. To validate the code results, the geometry and properties of the chill block were defined using the software. To do the validation, it was assumed that the chill starts at room temperature (300K). A known heat flux history was applied to the surface of the chill and the temperature time history at a known hypothetical TC location was recorded. The computer generated temperature time history was then entered into the IHC code and the results of the predicted heat flux were compared to that applied initially in FEMLAB. Figure 4-9 show the applied heat flux history that was used in FEMLAB.

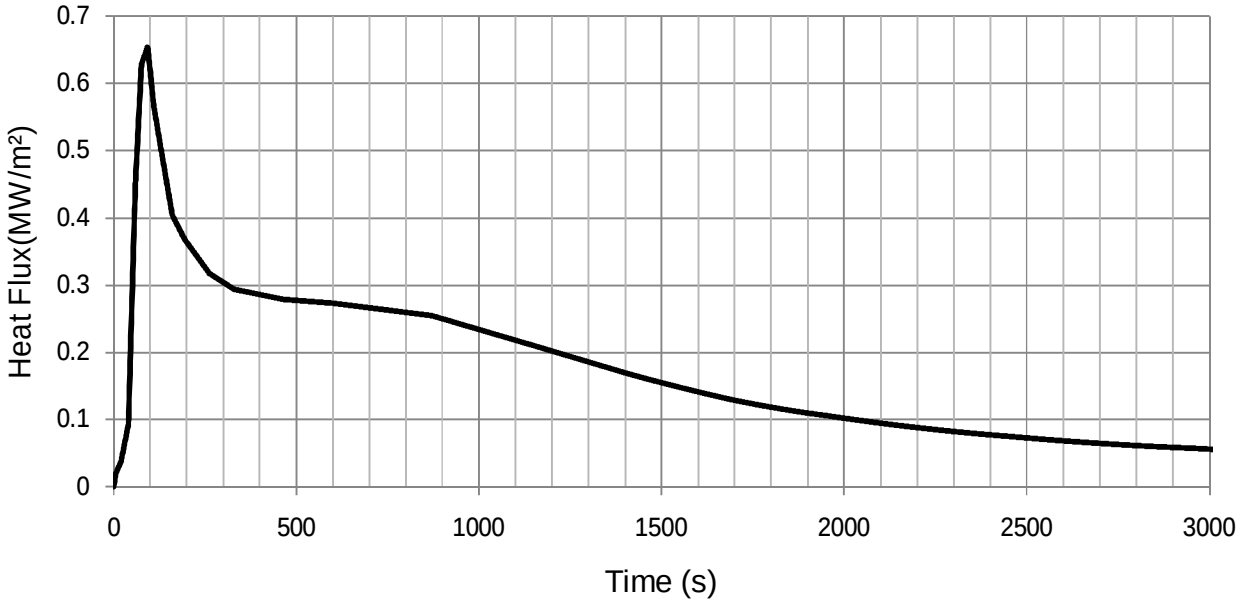

Figure 4-9 Applied heat flux history on the surface of the chill block in FEMLAB.

By applying the heat flux values, shown in Figure 4-9, and simulation of process, the FEMLAB predicted temperature time history at locations of (2mm) TC1 and (45mm) TC2 from the chill surface which are shown in Figure 4-10.

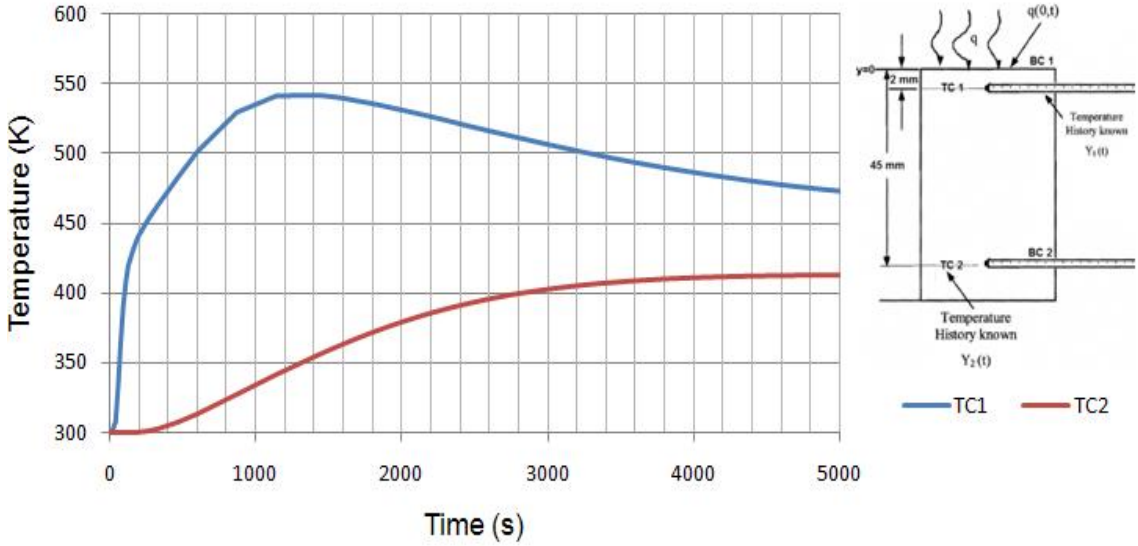

Figure 4-10 The FEMLAB predicted temperature time history at 2 mm (TC1) and 45 mm (TC2) below the interface of the chill.

Figure 4-11 shows a comparison between the applied heat flux history in FEMLAB compared to that predicted using the IHC model by employing the FEMLAB predicted temperature time history. As can be seen they match very well and provide some certainty that the IHC model will be able to accurately reproduce the heat transfer and the melt chill interface.

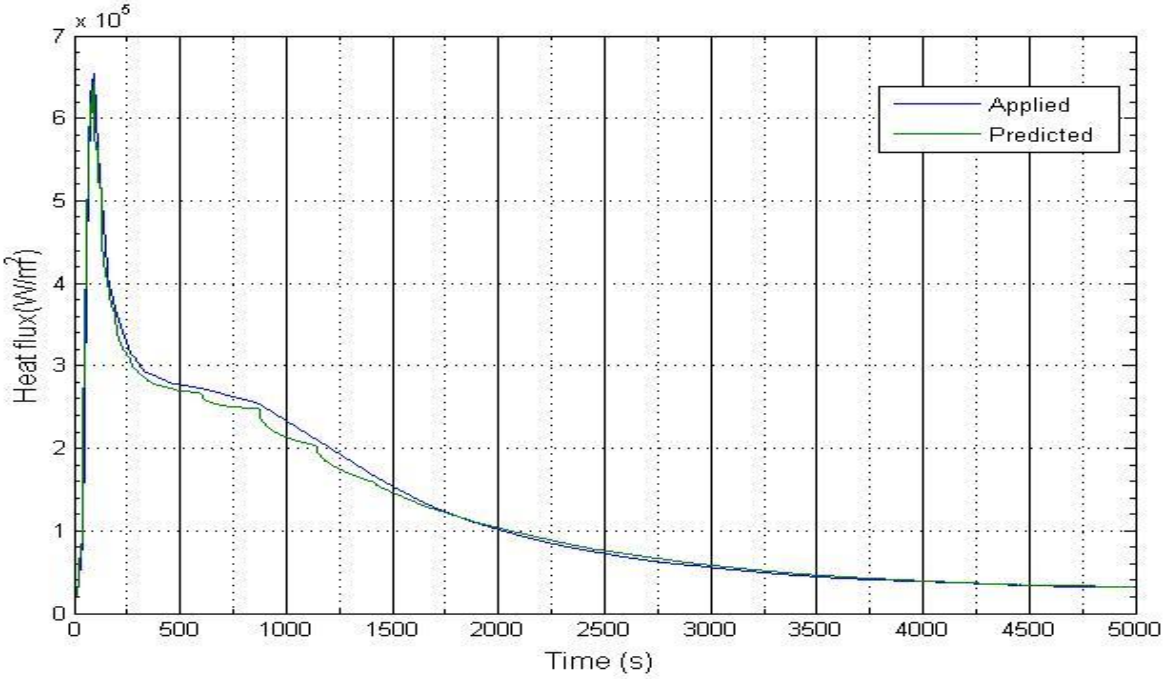

Figure 4-11 Comparison of the applied heat flux values on FEMLAB and the estimated heat flux values by the inverse code.

Chapter 5 Results and Discussion

In this chapter, the experimental results as well as a discussion of the analysis and results from this study are provided.

5.1 Evaluation of Test or Experimental Apparatus

Preliminary tests using the experimental apparatus were performed to ensure that the assumption in the IHC model that heat transfer occurs predominantly in the y-direction from the test metal to the chill block was assessed. This was done by examining the temperature histories measured at three radial locations in the test chamber and chill block. Figure 5-1 shows a top view of the spatial position of the thermocouples positioned within the test apparatus, 2 mm above the metal/mold interface. The distance between TC A and TC C/TC B was 23 mm.

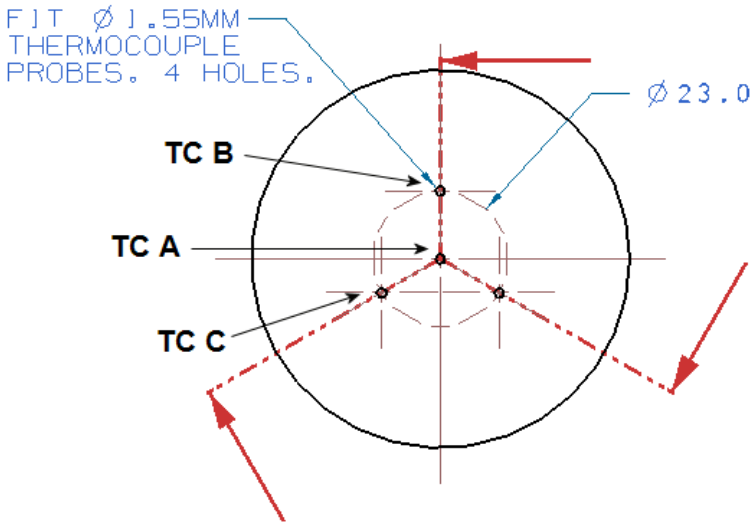

Figure 5-1 Top view showing the array of thermocouples in the test chamber.

As shown in Figure 5-2, measured temperatures at these three locations were within 98.7 % of each other.

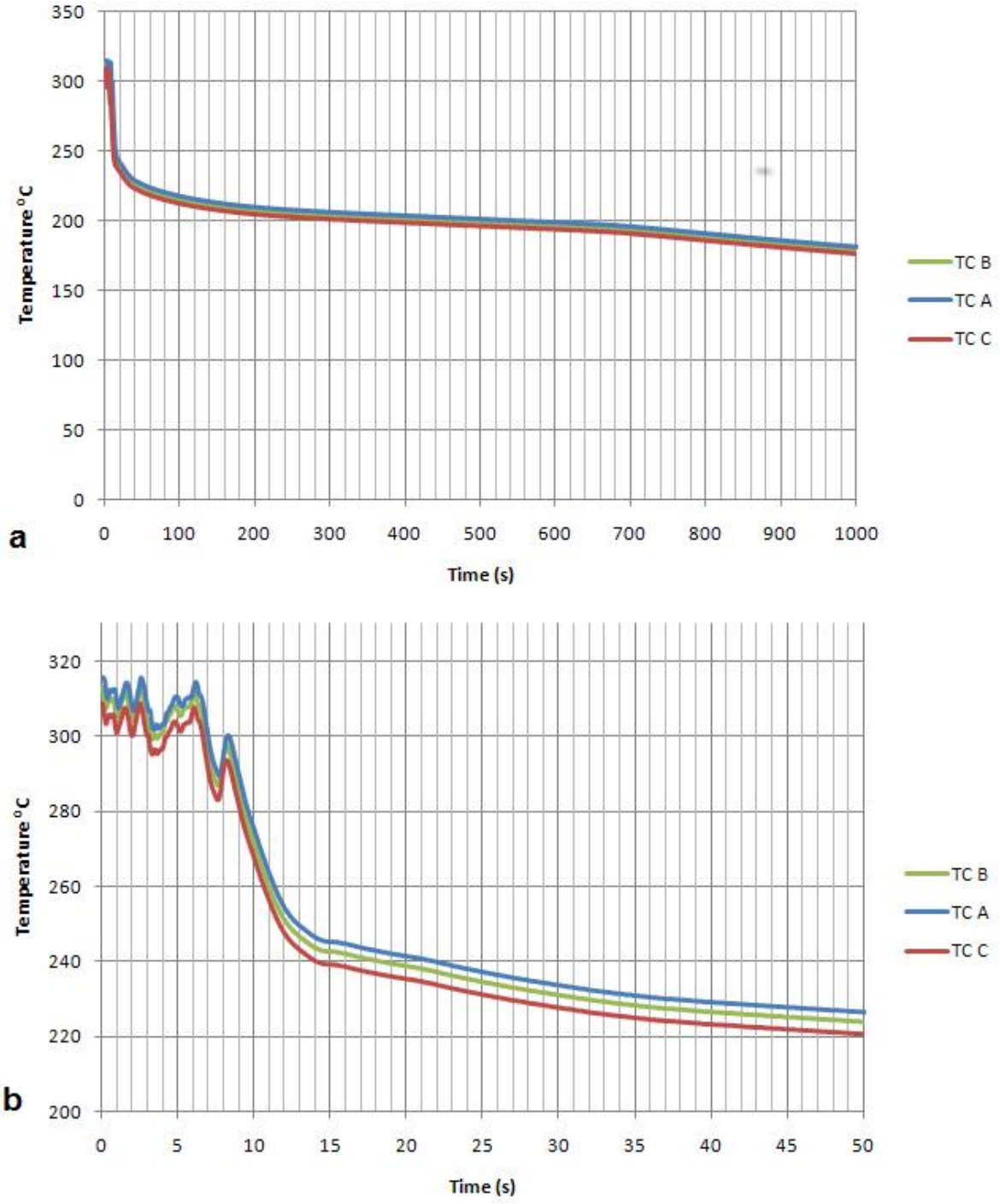

Figure 5-2 Temperature variation of the three thermocouples inside the test material showing a) the entire test period and b) a blow-up to 50 s.

5.2 Measured Temperatures

5.2.1 Chill Block

Typical recorded temperature histories in the chill and the test metal are shown in Figure 5-3 and Figure 5-4. The chill temperature measurements were made using TC1 (2mm below the interface) and TC2 (45 mm from the interface) while the measured temperature history inside the test metal corresponds TC3 (2 mm above the interface).

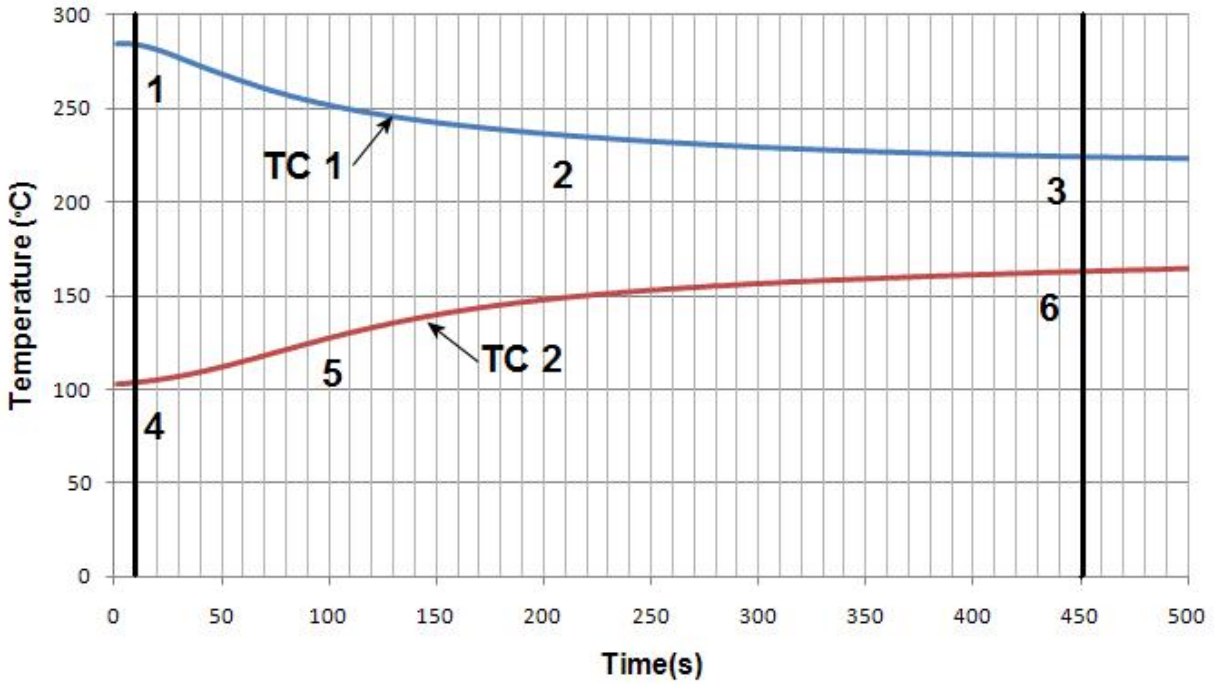

Figure 5-3 Typical measured temperature histories inside the chill during a test.

Referring to Figure 5-3, several pertinent aspects can be seen. Referring to TC1 (2 mm below the interface) it can be observed that the temperature starts to cool from point “1” to point “2” with a decreasing rate of cooling. Between point “2” to point “3” the cooling rate in the chill becomes constant and slower. The measured temperature history using TC2 in the chill is quite different from that measured by TC1 and is reflective of further distance away from the hot interface. The maximum temperature measured at this position is 173°C and the rate of increase is seen to change from the beginning of the test, point “4” to point “5” and then from point “5” to point “6”, the rate of increase decreases to a lower more constant value. Referring to the measured temperature histories in the chill, it can be seen that three distinct stages exist during a

test, namely: First, the recorded temperature values from time equal 0 to 25 seconds where the temperature is seen to increase with time for both thermocouples TC1 and TC2. Second, the recorded temperature values between 25 seconds to approximately 450 seconds where TC1 is decreasing and TC2 is increasing. Third, and finally, after 450 seconds where the cooling rates of both thermocouples are similar.

5.2.2 Test Metal

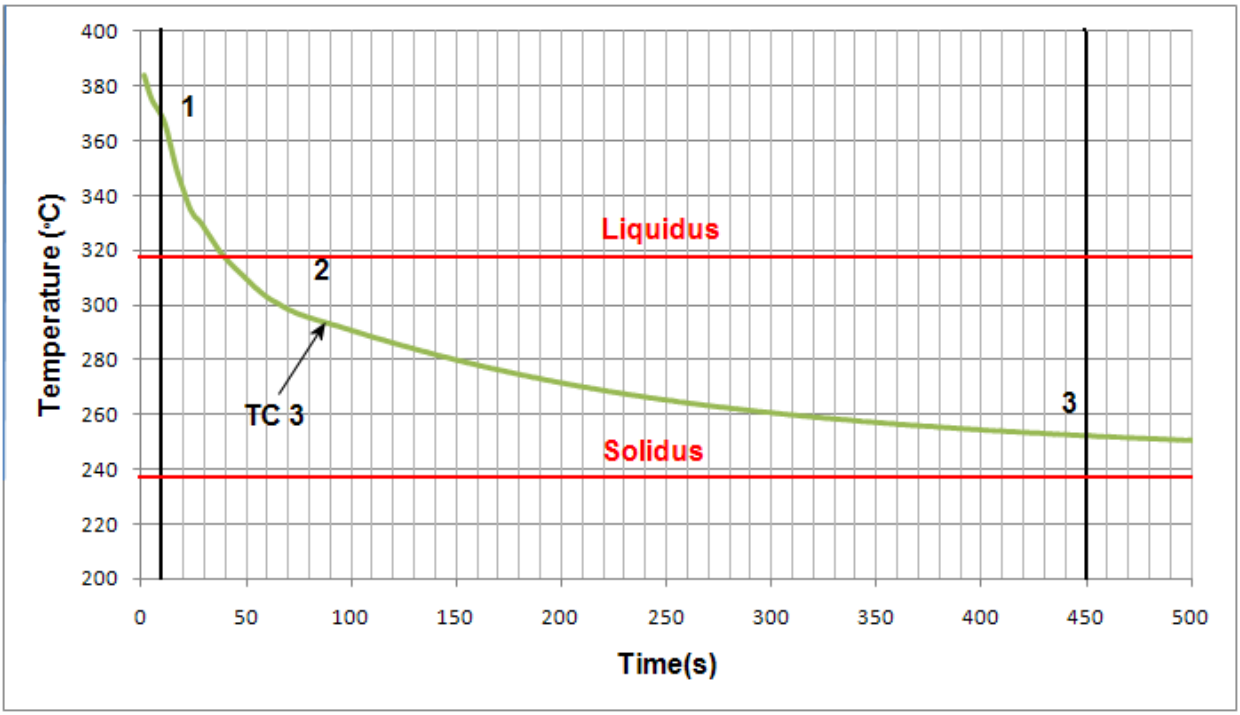

Figure 5-4 Typical measured temperature history inside the test metal during a test.

Figure 5-4 shows a typical measured temperature history in the test metal by TC3 at a position of 2 mm from the interface. Referring to Figure 5-4, at point "1", the temperature of the casting is close to 385 ºC. Quickly after point "1", the cooling rate for this thermocouple is very fast and just as solidification starts to occur (temp = 317°C) the rate of decrease in the temperature history slows down for a couple of seconds as solidification occurs and the latent heat is released. At point "2", the cooling rate slows down more and this slower cooling rate persists from point "2" to point "3". Referring to the temperature histories in the chill block shown in Figure 5-3 it can be seen at point "2" measured by TC1 and point "2" measured by

TC3 in Figure 5-4 the temperatures in both the chill block and test metal approach each other quickly. After this point, the temperatures in the chill block and test metal separate, which could be due to the formation of an air gap hence providing less heat transfer from the test metal to the chill. This also corresponds with the slower rate of heat extraction in the test metal.

5.2.3 IHC Result

Using the measured temperature history data in the chill block, the IHC model was used to calculate the surface heat flux history and surface temperature at the interface of the chill and test metal. After this was completed the heat transfer coefficient at the interface could be calculated. The calculated surface temperatures in both the test metal and chill block are shown in Figure 5-5. As the thermocouples are very close to the surface (2mm below the interface in the test metal and chill block), the modeled surface temperatures are close to the measured temperature histories by TC1 and TC3.

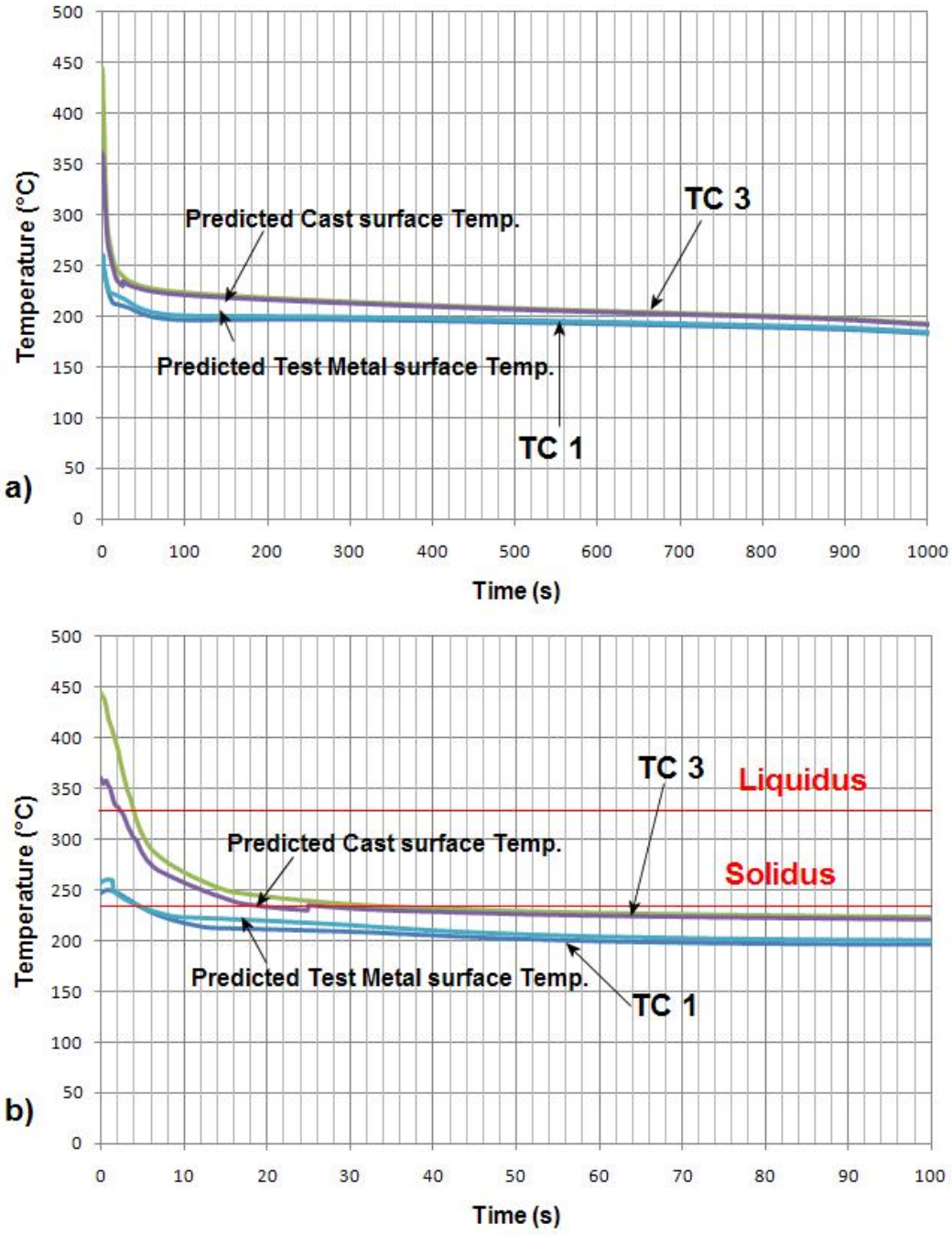

Figure 5-5 Typical recorded temperatures and the calculated surface temperatures a) the entire test period and b) a blow-up to 100 s.

Figure 5-6 shows the predicted heat flux at the interface between the test metal and chill block. Referring to Figure 5-6, it can be seen that the heat flux increases rapidly from time zero to point “1”. This can be explained because of good contact between the liquid metal and chill

block. At this point, point “1”, the contact between the molten metal and the chill will be maximum. The region between point ”1” and point “2” shows the heat flux values decrease because of imperfect contact between the chill and the casting metal. At this stage, small volumes of air gap are formed. At point “2”, the air gap formation at the chill-metal interface is completed and the solidified metal begins to separate from the chill surface which causes a rapid decrease of heat flux values. After point “3”, the heat flux values relatively remains constant during the experiment.

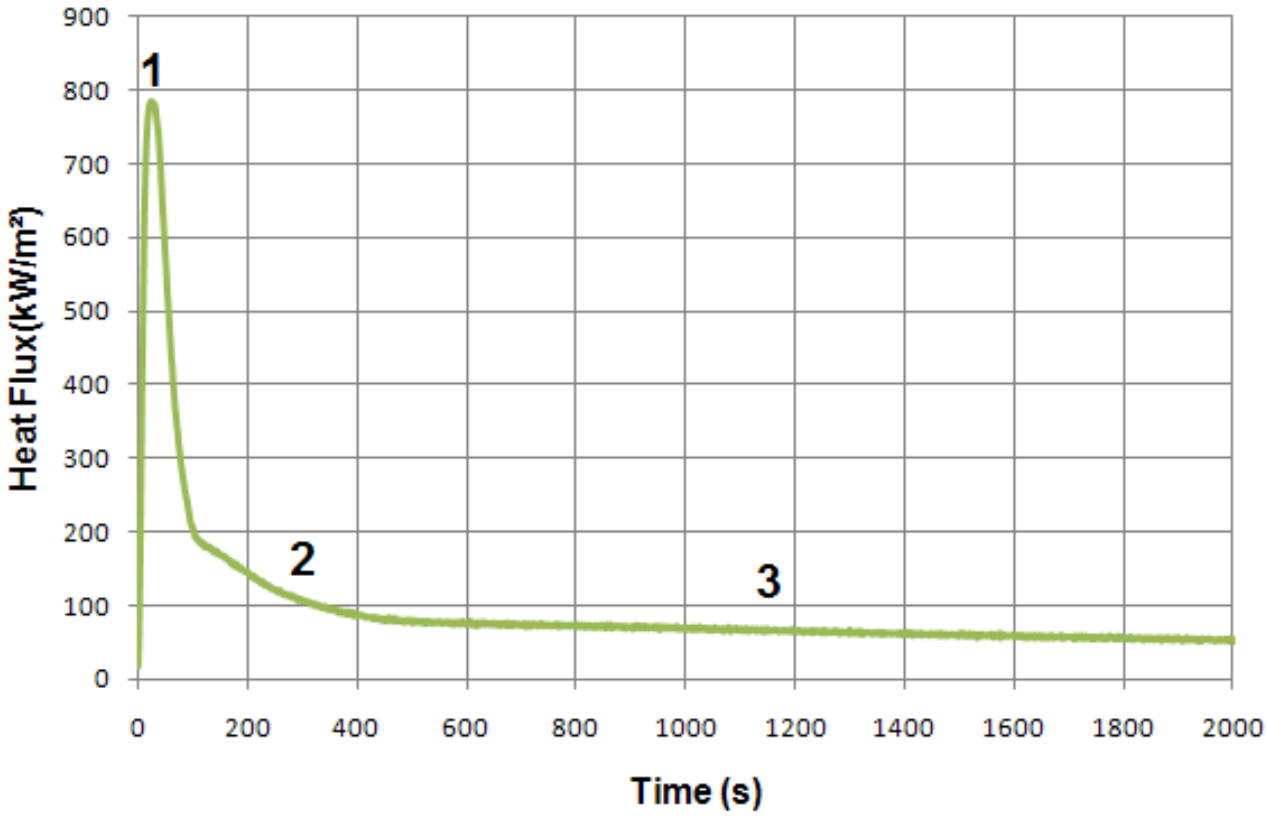

Figure 5-6 Typical predicted heat flux histories at the metal/chill interface.

5.2.4 Heat Transfer Coefficient (HTC)

After calculation of the heat flux values at the interface and surface temperatures, the heat transfer coefficient could be calculated and a typical result is shown in Figure 5-6. At point “1” the peak value in the HTC was achieved. From point “1” to point “2”, the HTC values decreases

rapidly which is followed by a small rise at point “3”. After the air gap forms at point “3”, the HTC values starts to decrease and remains relatively constant after point “4”.

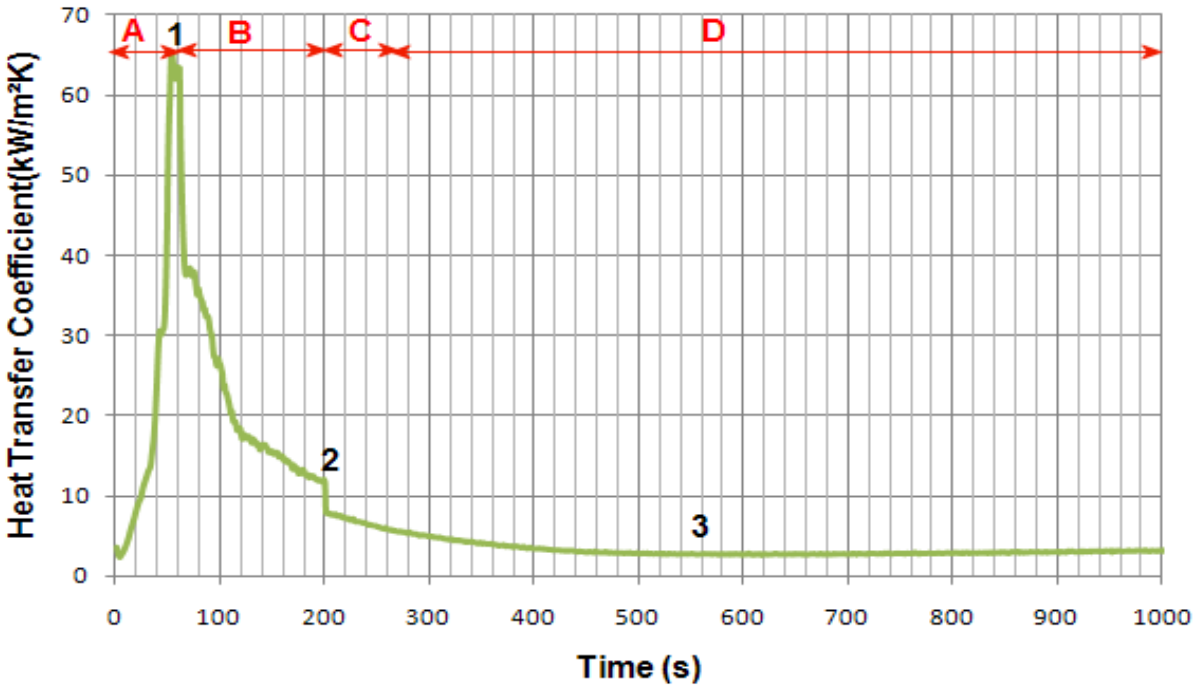

Figure 5-7 Typical calculated heat transfer coefficient history at the metal/mold interface.

5.2.4.1 Stages of Interfacial Heat Transfer

There are four different stages in studying heat flux and heat transfer coefficient at the metal/mold interface. In the first stage, stage “A”, the primary heat transfer mode is conduction through the liquid metal to the chill block. This stage occurs before solidification of the metal, when the molten metal is in near perfect contact with the chill surface. During cooling of the molten metal by the water cooled chill, a thin layer of solidified metal forms at the interface of the metal and chill (Stage “B”) and small air pockets start to form due to solidification shrinkage of the test metal away from the chill block. At the next stage, Stage ”C”, a complete air gap forms between the solidifying metal and the chill surface. In this stage, the dominant form of heat flux is conduction through the metal/mold air gap. The conductivity of air is three orders of magnitude lower than the conductivity of the metal (0.024 W/m.K for air versus 26 W/m.K for the metal). In the final stage, stage “D”, the air gap is formed completely, and heat transfer is in a steady state situation.

5.2.5 Effect of Superheat

The effect of superheat was investigated by running two tests with different amount of starting superheat (30° and 100°C). Figure 5-8 and Figure 5-9 show the predicted heat flux and heat transfer coefficient for two different starting superheats. As can be seen in Figure 5-8, the peak heat transfer coefficients for the test run at 100 ºC superheat is much higher than the peak heat transfer coefficient for the 30 ºC superheat experiment at 65 kW/m²K and 92 kW/m²K respectively. After the peak value, surface temperatures of the casting part and the chill part approach each other, an air gap forms and the heat transfer coefficient decreases rapidly. As the size of the air gap stabilizes, the heat transfer coefficient reduces rapidly and eventually reaches a steady state of 4300 W/m²K for both tests.

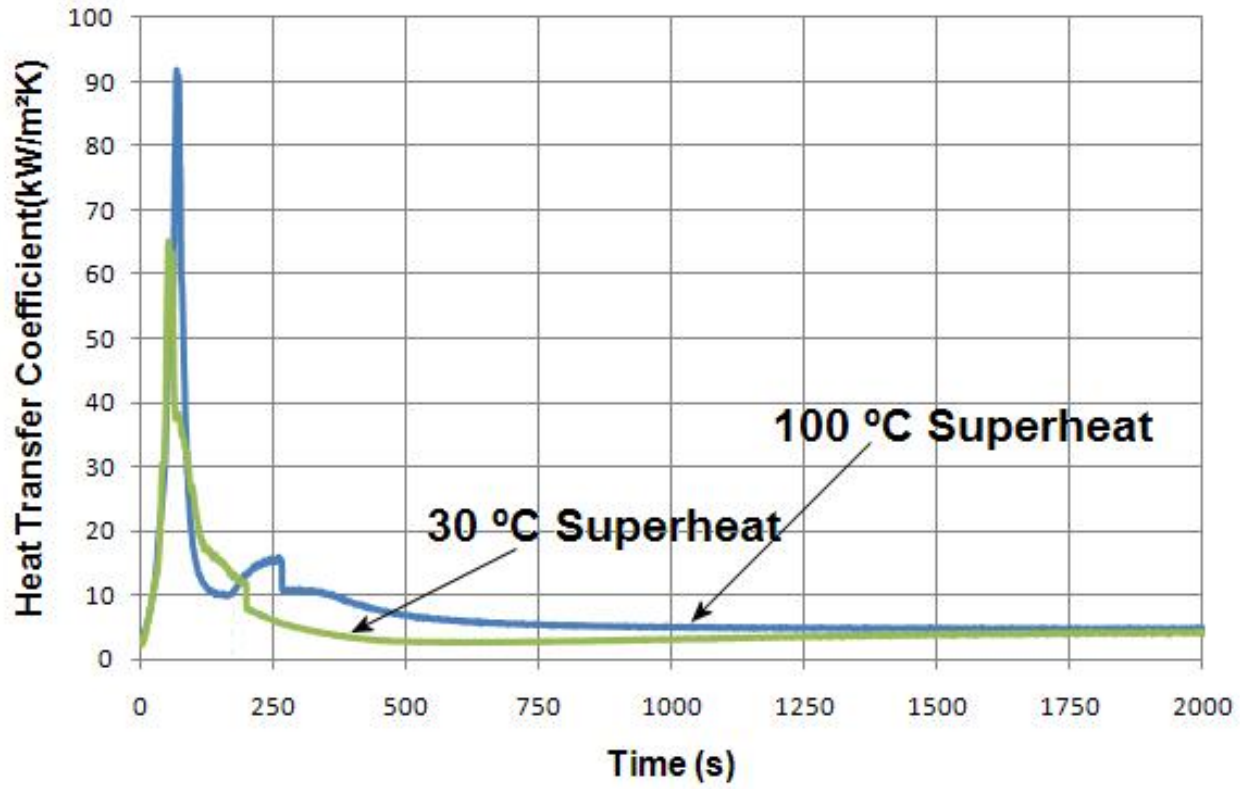

Figure 5-8 Comparison of HTC for 30 ºC and 100 ºC cast superheat and roughness of 43.4µm.

Figure 5-8 shows the calculated HTC values for both 30 ºC and 100 ºC. Four stages of heat transfer can be observed from the curves. Stage “A” is followed by a fast decrease in the HTC values. The starting air gap formation, stage ”B”, is around 200 seconds for the 30 ºC superheat case and 250 seconds for the 100 ºC superheat. Stage “C”, which is the complete air

gap formation, occurred later for the 100 ºC superheat because of the larger amount of heat, required to be removed in the higher superheat case. By comparing the results of the 30 ºC and 100 ºC superheat cases, it can be found out that the HTC values for the 30 ºC superheat experiment are less than the HTC values of 100 ºC superheat experiment for stages of “A”, ”B”, and “D” . At stage “D”, both curves show a similar constant HTC values of 4000-4500 W/m²K.

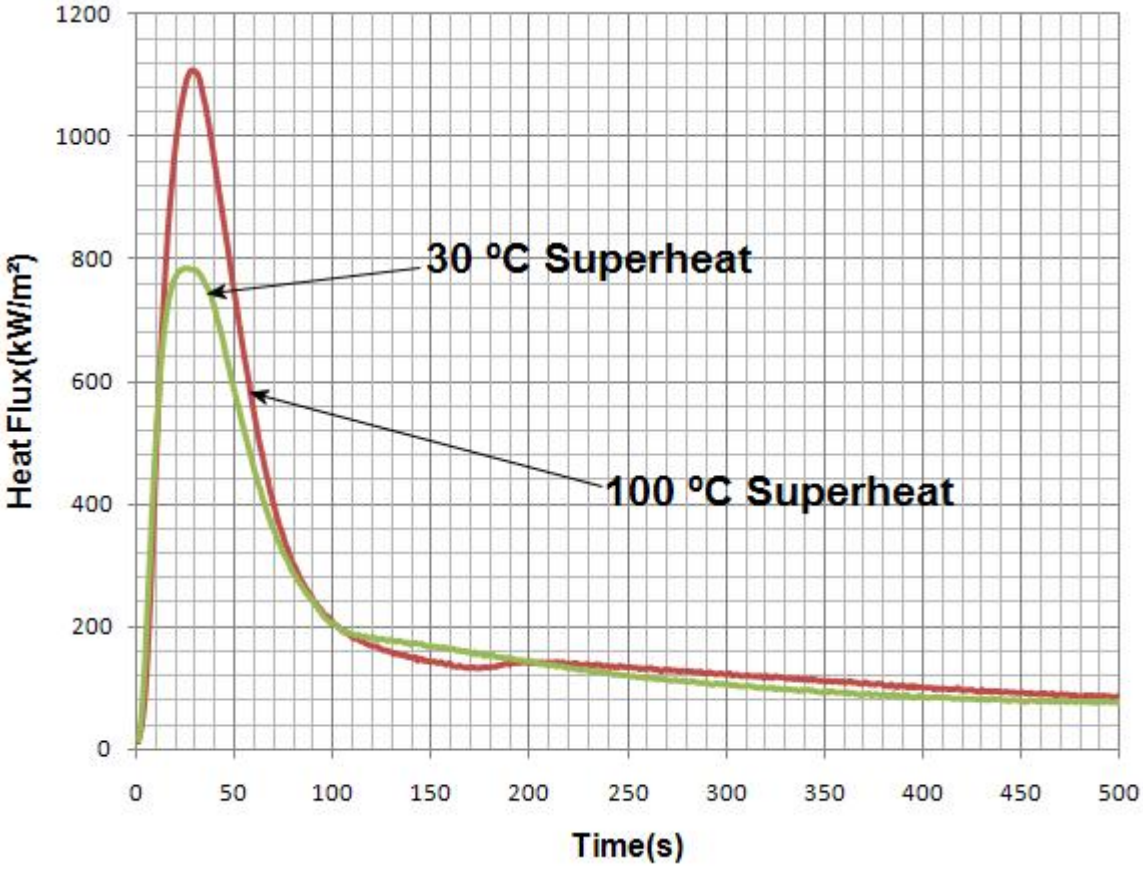

Figure 5-9 Comparison of heat flux for 30 ºC and 100 ºC cast superheat and roughness of 43.4µm.

Figure 5-9 shows a comparison of the calculated heat flux for 30 ºC and 100 ºC cast superheat. By increasing the cast superheat from 30 ºC to 100 ºC, the maximum heat flux is increased from 785 kW/m² to 1107 kW/m².

Figure 5-10 illustrates the calculated HTC values and liquid fraction vs. cast surface temperature. It is shown that the 100 ºC cast superheat has the maximum heat transfer coefficient in the solidification area and for both curves, the final stage of air gap formation, stage “C” is occurred at the solidus temperature of the alloy.

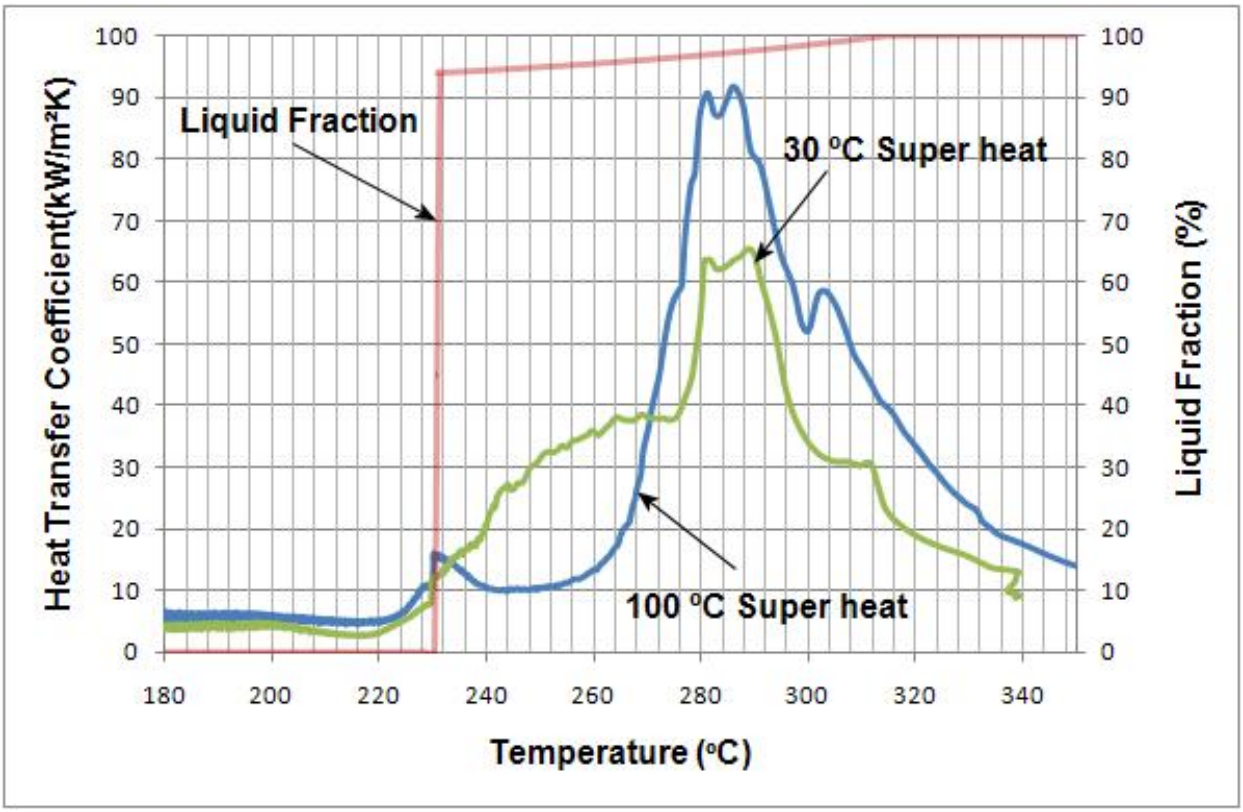

Figure 5-10 Calculated HTC values vs. cast surface temperature flux for 30 ºC and 100 ºC cast superheat and roughness of 43.4µm.

As shown in Figure 5-11, the average and peak HTC increase by increasing the cast superheat. The average value for each test is calculated from time zero to the final air gap formation time.

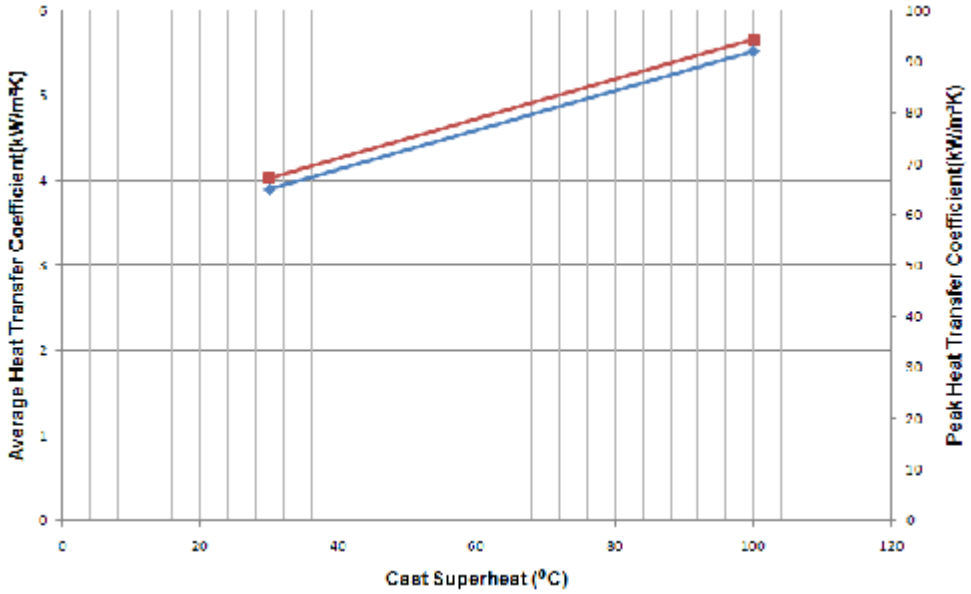

Figure 5-11 Effect of cast superheat on the peak and average heat transfer coefficient during solidification for 30 ºC and 100 ºC cast superheat and roughness of 43.4µm.

Figure 5-12 shows a comparison of the average heat flux of the current study with Carletti et al's experiment [8].

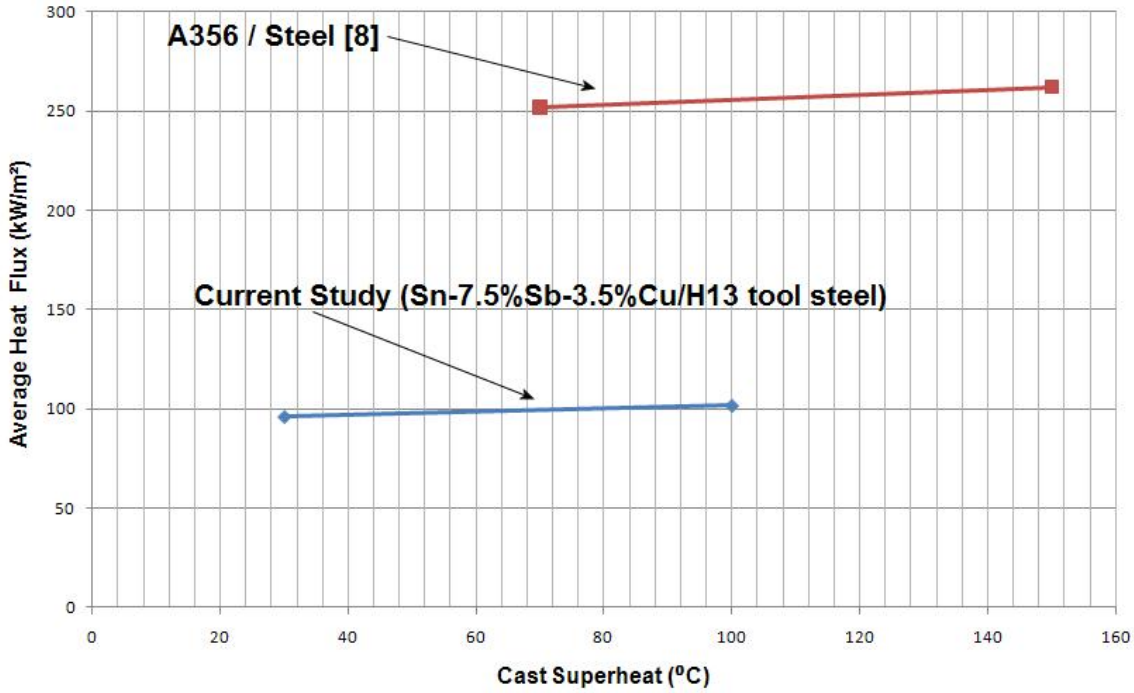

Figure 5-12 Comparison of the average heat flux from the current study with Carletti et al's experiment.

5.2.6 Effect of the Chill Surface Roughness

Figure 5-13 shows the comparison of the calculated HTC values for different surface roughness of R_A =0.1µm and R_A =43.1µm. The maximum or peak value of the HTC curves for R_A =0.1µm and R_A =43.4µm corresponds to values of 142 kW/m²K and 92 kW/m²K respectively. As shown, a much higher peak HTC is seen for the chill surface with the smoother surface. After these peaks, the heat transfer coefficient decreases rapidly due to the air gap formation. At later times point "1" for the lower roughness and point "2" for the higher roughness there is a further step change in the HTC as a complete air gap is formed. At this stage, the HTC values drop very fast. This stage occurred later for the R_A =0.1µm. By comparing the results of the R_A =0.1µm and R_A =43.4µm cases, it can be seen that the HTC values of R_A =43.4µm experiment are less than the HTC values of R_A =0.1µm experiment for the stages of "A", "B", and "D" .

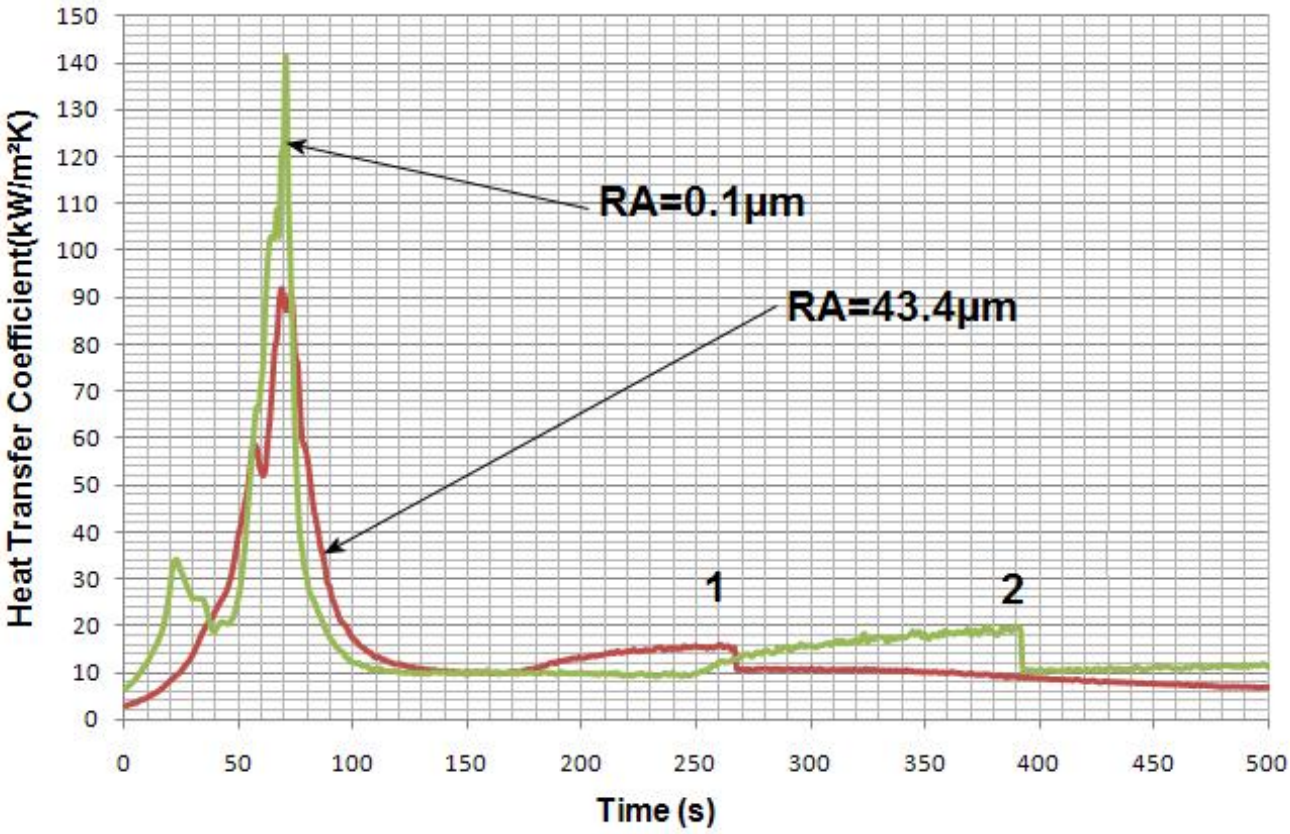

Figure 5-13 Comparison of HTC for R_A =0.1µm and R_A =43.4µm chill surface roughness with 100 ºC cast superheat.

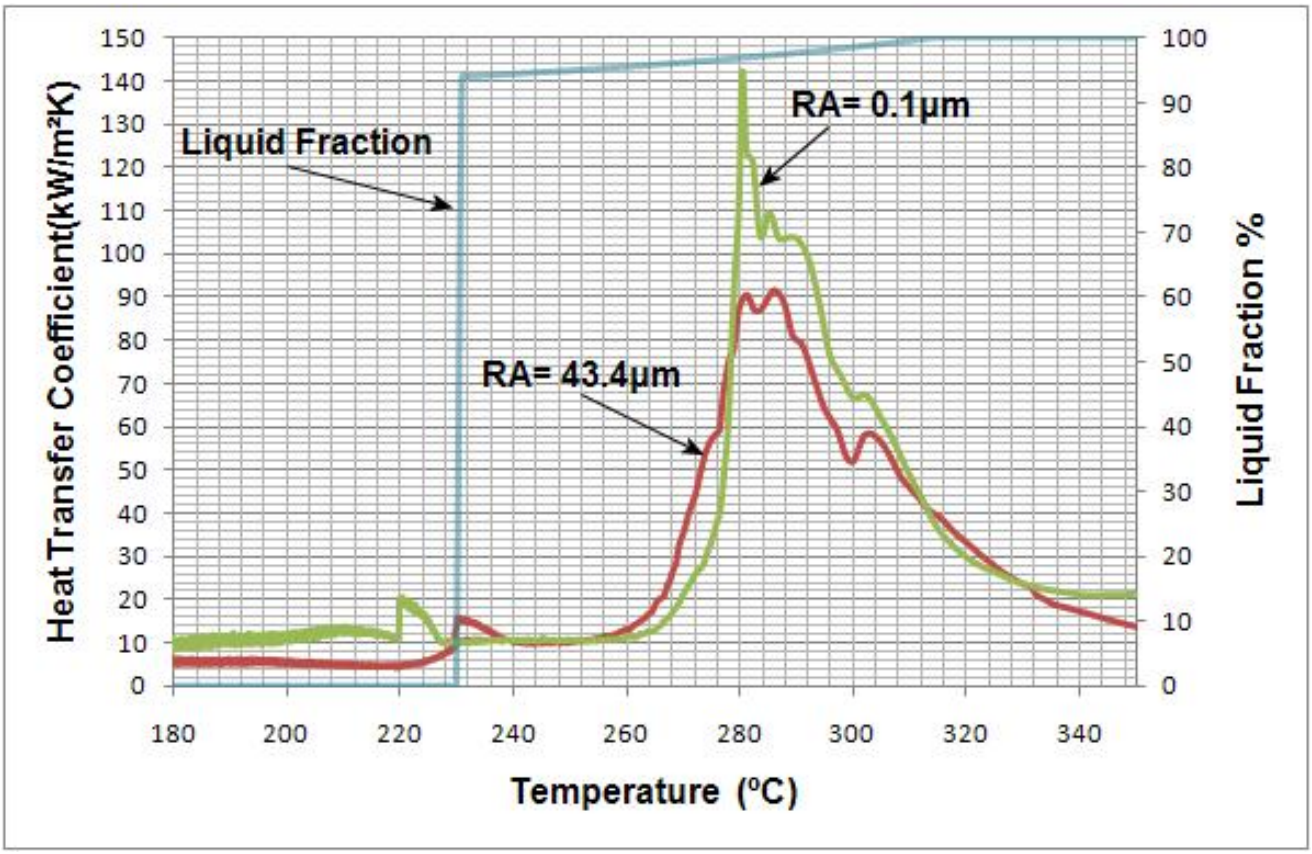

Figure 5-14 Calculated HTC values vs. cast surface temperature for R_A =0.1µm and R_A =43.4µm chill surface roughness with 100 ºC cast superheat.

Figure 5-14 illustrates the calculated HTC values and liquid fraction vs. cast surface temperature. It is shown that the R_A =0.1µm has the maximum heat transfer coefficient during solidification. For both curves, the final stage of air gap formation, stage "C" occurred after the solidus temperature of the alloy.

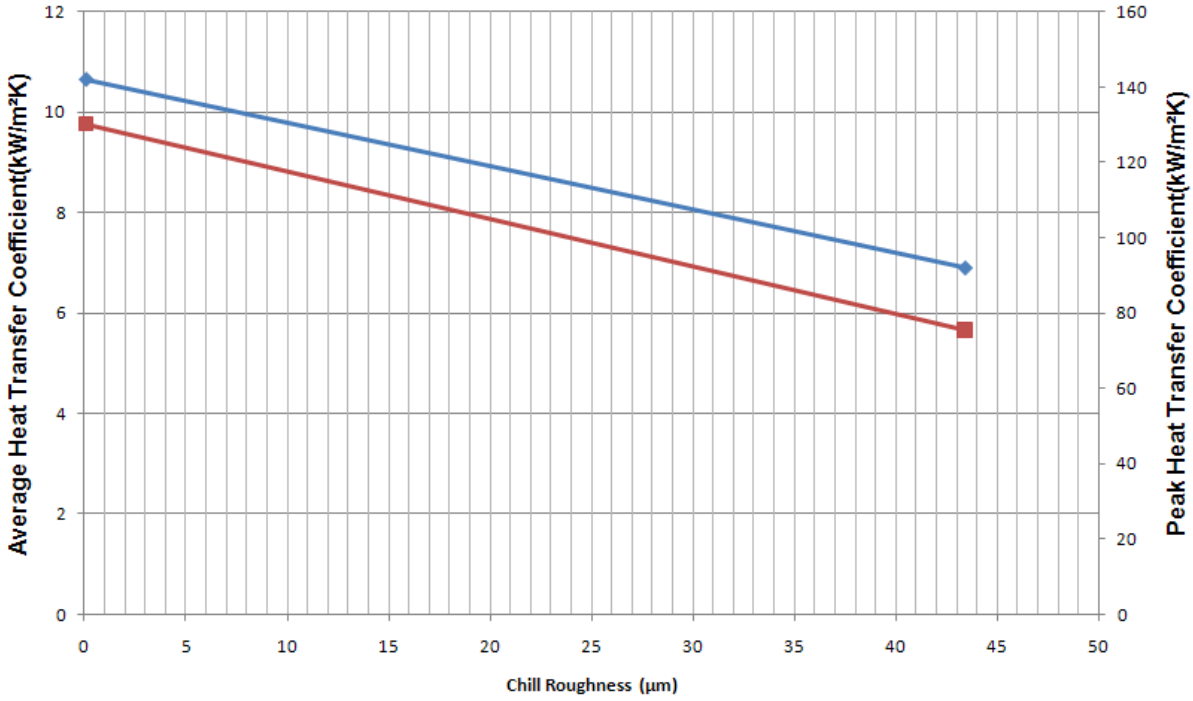

Figure 5-15 Effect of surface roughness on the peak heat transfer coefficient and average HTC during solidification.

Figure 5-15 shows the average HTC and maximum HTC increase by decreasing the chill surface roughness. Figure 5-16 shows a comparison of the average flux of current study with Carletti et al's experiment for a superheat of 150 ºC.

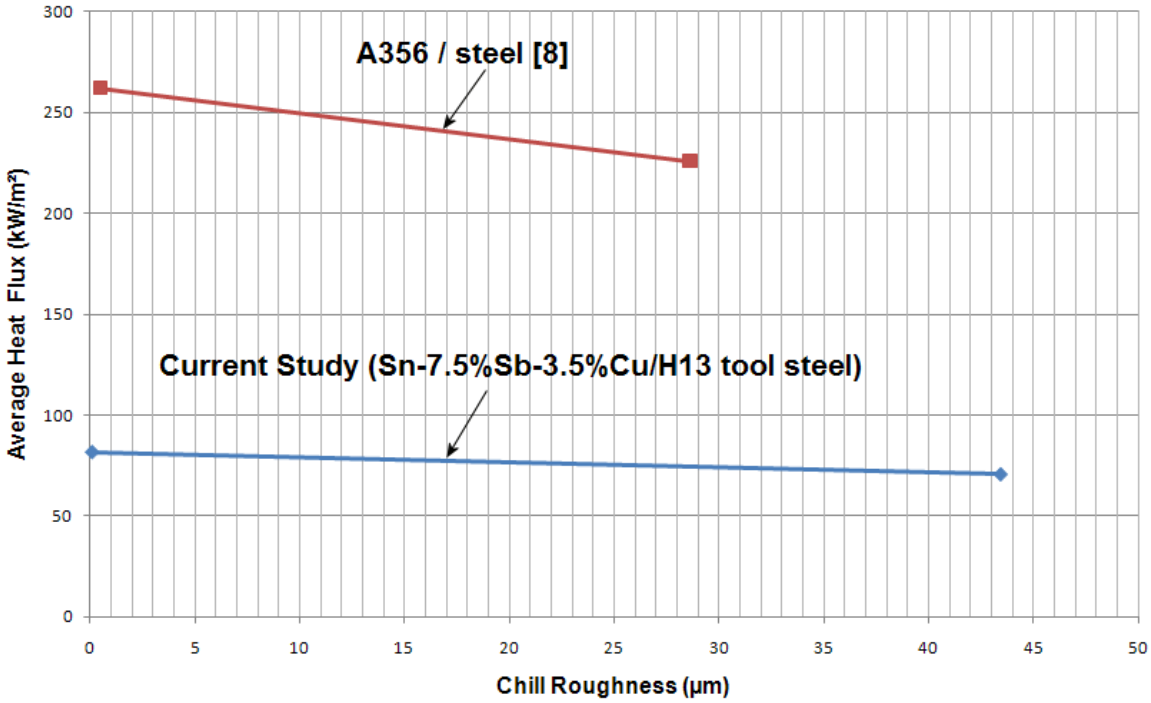

Figure 5-16 Comparison of the average flux of current study with Carletti et al's experiment at superheat of 150 ºC.

Chapter 6 Summary and Conclusions

Accurate knowledge of the heat transfer coefficient during casting (between a molten and/or semi-solid material and the mold) is critical to be able to develop representative mathematical models for casting process such as Twin Roll Casting (TRC). In this project, an experimental apparatus was developed to enable to measurement of the heat transfer coefficient (HTC) at the interface between a liquid metal as it solidifies against a chill surface.

The research involved the design and building of the experimental apparatus which consisted of a cylinder and piston surrounded by a heater to melt the metal samples. Although the system was designed to apply pressure to the interface between the chill and solidifying metal unfortunately this part of the experimental apparatus was never successful as leakage of molten metal around the sides of the piston occurred. Using the measured temperature time history, the interfacial heat transfer was calculated by using an inverse heat conduction method in conjunction with the known thermo-physical properties of the chill and solidifying metal. The apparatus was tested successfully using Sn-7.5%Sb-3.5%Cu alloy as the casting metal solidifying against a H13 tool steel chill block. In addition, the effect of different values of chill roughness and test metal superheat were investigated on the heat transfer coefficient.

6.1 Conclusions

The most important results from this work include:

- The experimental apparatus is well designed and it was confirmed by experimental measurements that the assumption of 1-D heat transfer from the test metal to the chill block is valid. Repeatability of the tests is good and test results vary within ~7% from test to test
- Implicit and explicit numerical inverse heat conduction codes were developed, validated and employed to model the metal-mold interface heat flux and heat transfer coefficient.
- Peak heat flux and heat transfer coefficient values were found to take place during the initial moments of casting solidification within 1-5 seconds after solidification at solid fractions of 2%. After this initial solidification a rapid

decrease in heat transfer was noted which coincided with the formation of an air gap at the interface.

- Melt superheat had a significant effect of the measured heat transfer and caused the peak HTC to increase 42%. In addition, the peak heat flux was found to increase about 41%. The effect superheat on the average heat transfer during solidification was to increase it by about 40%. This is consistent with other work show in the literature for other alloy systems.
- Peak values for HTC significantly higher than reported for other alloy systems could be due to the high cooling rate the chill and very fast solidification of the test metal which could cause the inverse code to analyze the data at that period with less accuracy.
- Chill surface roughness also had an effect of the measured heat transfer and caused the peak HTC to increase 58%. In addition, the average heat flux was found to increase 15%. The effect superheat on the average heat transfer during solidification was to increase it by 58%. This is consistent with other work show in the literature for other alloy systems.

6.2 Future work

The versatility of the designed apparatus allows the investigation of many different factors on the interfacial heat flux and heat transfer coefficient values that occur between a solidifying metal against a chill simulating what occurs during a variety of casting processes such had TRC. Future work should include investigating the following factors of the heat transfer between a solidifying metal and chill:

- Effect of interface pressure
- Effect of test metal length (weight).
- Effect of different chill blocks and test metals
- Effects of lubricants and surface coatings on the chill block

Bibliography

1 NSERC Magnesium Network. Disponivel em: <http://www.magnet.ubc.ca/. [Online]>.

2 D. Liang and C. B. Cowley. "The Twin-Roll Strip Casting of Magnesium", **Journal of the Minerals, Metals and Materials Society**, Vol. 56, pp. 26-28, (2004).

3 J. W. Woolley and K. A. Woodbury. "The Interfacial Heat Transfer Coefficient of Metal Castings – A Literature Review", **American Foundry Society**, (2006).

4 T. S. Prasanna Kumar and K. Narayan. "Heat Flux Transient at the Casting/Chill during solidification of Aluminium Base Alloys", **Metallurgical Transaction B**, Vol. 22B, pp. 717–729, (1991).

5 W. D. Griffiths. "The Heat Transfer Coefficient during the Unidirectional Solidification of an Al-Si Alloy Casting", **Metallurgical and Materials Transaction B**, Vol. 30B, pp. 473-482, (1999).

6 K. Ho and R. D. Pehlke. "Mechanisms of Heat Transfer at a Metal-Mold Interface", **AFS Transactions**, Vol. 92, pp. 587-598, (1984).

7 K. Ho and R. D. Pehlke. "Metal-Mold interfacial heat transfer", **Metallurgical Transaction B**, Vol. 16B, pp. 585-594, (1985).

8 H. G. Carletti. "Determination of Metal-Mold Heat Transfer Coefficient for Aluminium Alloys", **Thesis. University of Toronto**, pp. 5, (2006).

9 D. G. R. Sharma and M. Krishnan. "Simulation of Heat Transfer at Casting Metal-Mold Interface", **AFS Transactions**, Vol. 99, pp. 429-438, (1991).

10 S. A. Argyropoulos and H. Carletti. "Comparisons of the Effects of Air and Helium on Heat Transfer at the Metal-Mold Interface", **METALLURGICAL AND MATERIALS TRANSACTIONS B**, Vol. 39B, pp. 457-468, (2008).

11 Y. Nishida and W. Droste. "The Air-Gap Formation Process at the Casting-Mold Interface and the Heat Transfer Mechanism through the Gap", **Metallurgical Transaction B**, Vol. 17B, pp. 833-844, (1986).

12 M. Trovant and S. Argyropoulos. "Finding Boundary Conditions: A Coupling Strategy for the Modeling of Metal Casting Processes: Part I. Experimental Study and Correlation

Development", **Metallurgical and Materials Transactions B**, Vol. 31B, pp. 75-86, (2000).

13 M. Trovant and S. Argyropoulos. "Finding boundary conditions: a coupling strategy for the modeling of metal casting processes", **Metall. Transaction B**, Vol. 31B, pp. 75-86, (2000).

14 J. V. Beck. "Criteria for Comparison of Methods of Solution of the Inverse Heat Conduction Problem", **Nuclear Engineering Design**, Vol. 53, pp. 11-22, (1980).

15 J. V. Beck, B. Blackwell and C. R. J. S. Clair. "Inverse Heat Conduction: Ill-posed Problems", **John Wiley**, (1985).

16 J. V. Beck. "Transient Sensitivity Coefficients for the Thermal Contact Conductance", **International Journal of Heat and Mass Transfer**, Vol. 10, pp. 1615-1616, (1967).

17 J. V. Beck. "Determination of Optimum Transient Experiments for Thermal Contact Conductance", Vol. 12, pp. 621-633, (1969).

18 D. Li and M. A. Wells. "Effect of subsurface thermocouple installation on the discrepancy of the measured thermal history and predicted surface heatflux during a quench operation", **Metallurgical and Materials Transactions B**, Vol. 36B, pp. 343-354, (2005).

19 M. A. Martorano and J. D. T. Capocchi. "Heat Transfer Coefficient at the Metal-Mold Interface in the Unidirectional Solidification of Cu-8%Sn Alloys", **International Journal of Heat and Mass Transfer**, pp. 2541-2552, (2000).

20 D. O'Mahoney, D. J. Browne and M. Hussey. "Effect of Experimental Uncertainty on the Accuracy and Stability of a New Inverse Method for Heat Transfer in Solidification", **Proceeding of the 35th National Heat Transfer Conference**, pp. 1165-1173, (2001).

21 V. Sahai. "Predicting Interfacial Contact Conductance and Gap Formation of Investment Cast Alloy 718", **Journal of Thermophysics and Heat Transfer**, Vol. 12, pp. 562-566, (1998).

22 P. Schmidt and I. L. Svensson. **Solidification and Heat Transfer in Permanent Mould Casting**. Proceedings of the 7th International Conference of Numerical Methods Problems. Swansea, United Kingdom: Pineridge Press Ltd. 1991. p. 236-247.

23 P. Schmidt. "Heat Transfer during filling in die casting processes", **Material Science and Engineering**, Vol. A173, pp. 271-274, (1993).

24 Y. Nisida and H. Matsubara. "Effects of pressure on Heat Transfer at the Metal Mold Casting Interface", **The British Foundaryman**, Vol. 69, pp. 274278, (1976).

25 J. Isaac, G. P. Reddy and G. K. Sharma. "Variation of heat transfer coefficients during solidification of castings in metallic molds", **The British Foundryman**, Vol. 78, pp. 465-468, (1985).

26 I. L. Ferreira, J. E. Spinelli and B. Nestler. "Influences of solute content, melt superheat and growth direction on the transient metal/mold interfacial heat transfer coefficient during solidification of Sn–Pb alloys", **Materials Chemistry and Physics**, Vol. 111, pp. 444–454, (2008).

27 E. N. Souza, N. Cheung and C. A. Santos. "The variation of the metal/mold heat transfer coefficient along the cross section of cylindrical shaped castings", **Inverse Problems in Science and Engineering**, Vol. 14, pp. 467–481, (2008).

28 J. E. Spinelli and I. Leão Ferreira. "Evaluation of heat transfer coefficients during upward and downward transient directional solidification of Al–Si alloys", **Struct Multidisc Optim**, pp. 241–248, (2006).

29 M. Krishnan and D. G. R. Sharma. "Determination of Heat Transfer Coefficient Between Casting and Chill in Unidirectional Heat Flow", **AFS Transactions**, Vol. 10, pp. 769-774, (1994).

30 A. Assar. "On the terface heat transfer coefficient for cylindrical ingot casting in a metal mould", **Journal of Material Science**, Vol. 11, pp. 601-606, (1992).

31 C. A. Muojekwu, I. V. Samarasekera and J. K. Brimaco. "Heat Transfer and Microstructure during the early Stages of Metal Solidification", **Metallurgical and Materials Transaction B**, Vol. 26B, pp. 361-382, (1995).

32 J. A. Sekhar and G. J. Abbaschian. "Effect of Pressure on Metal-Die Heat Transfer Coefficient during Solidification", **Materials Science and Engineering**, Vol. 40, pp. 105 - 110, (1979).

33 N. Akar, H. Mehmet ahin and N. Yalçin. "EXPERIMENTAL STUDY ON THE EFFECT OF LIQUID METAL SUPERHEAT AND CASTING HEIGHT ON INTERFACIAL HEAT TRANSFER COEFFICIENT", **Experimental Heat Transfer**, Vol. 21, pp. 83–98, (2008).

34 M. A. T. and N. A. El-Mahallawy. "Effect of MElt super heat and chill material on interface heat-transfer coefficient in end-chill Al and Al-Cu alloy casting"", **Journal of Material Science**, Vol. 27, pp. 3467-3473, (1992).

35 M. Krishnan and D. G. R. Sharma. "The Effect of Alloy Properties on Heat Flow Across the Casting/Mold Interface", **Scripta Metallurgy and Materialia**, pp. 447-451, (1993).

36 B. Coates and S. A. Argyropoulos. "The Effects of Surface Roughness and Metal Temperature on the Heat-Transfer Coefficient at the Metal Mold Interface", **METALLURGICAL AND MATERIALS TRANSACTIONS B**, Vol. 38B, pp. 243-255, (2007).

37 N. A. El-Mahallawy and A. M. Assar. "Effect of melt superheat on heat transfer coefficient for aluminium solidifying against copper chill", **Journal of Materials Science**, Vol. 26, pp. 1729-1733, (1991).

38 M. Bamberger and M. M. Stupel. "Influence of Different Chill Materials on Heat Flux and Dentritic Arm Spacing of A356 Aluminium Alloy Casting", **Giessereiforschung**, Vol. 38, pp. 77-80, (1986).

39 E. S. Tillman and J. T. B. "Influence of thermal contact resistance on the solidification rate of long freezing range alloys", **AFS Cast Metals Research Journal**, Vol. 8, pp. 1-6, (1972).

40 R. C. Sun. "Simulation and Study of Surface conductance for heat flow in the early stage of casting", **AFS Cast Metals Researcch Journal**, Vol. 6, pp. 105-110, (1970).

41 K. Ho and R. D. Pehlke. "Transient Methods for Determination of Metal-Mold Interfacial Heat Transfer", **AFS Transactions**, Vol. 91, pp. 689-698, (1983).

42 T. X. Hou and R. D. Pehlke. "Determination of Mold-Metal Interfacial Heat Transfer and Simulation of Solidification of an Aluminum-13% Silicon Casting", **AFS Transactions**, Vol. 96, pp. 129-136, (1988).

43 M. A. Taha, N. A. El-Mahallawy and M. T. El-Mestekawi. "Estimation of Air Gap and Heat Transfer Coefficient at Different Faces of Al and Al-Si Castings Solidifying in Permanent Mould", **Material Science and Technology**, Vol. 17, pp. 1093-1101, (2001).

44 M. Trovant and S. Argyropoulos. "Finding Boundary Conditions: A Coupling Strategy for the Modeling of Metal Casting Processes: Part II. Numerical Study and Analysis", **Metallurgical and Materials Transactions B**, Vol. 31B, pp. 87-96, (2000b).

45 M. C. Lukens, T.-X. Hou and R. D. Pehlke. "Mold/Metal Gap formation of Al-14% Si Alloy Horizontal Cylinders Cast chromite Molding Sand", **AFS Transactions**, Vol. 99, pp. 445-449, (1991).

46 J. H. Kuo and F. L. Hsu. "Effects of Mold Coating and Mold Material on the Heat Transfer Coefficient at the Casting/Mold Interface for Permanent Mold Casting of A356 Aluminum Alloy", **International Conference on Solidification Science and Processing**, pp. 201-212, (2001).

47 C. A. Santos, J. M. V. Quaresma and A. Garcia. "Determination of Transient Interfacial Heat Transfer Coefficients in Chill Mold Castings", **Journal of Alloys and Compounds**, Vol. 319, pp. 174-186, (2001).

48 M. Prates and H. Biloni. "Variables Affecting the Nature of the Chill Zone", **Metallurgical Transactions A**, Vol. 3A, pp. 1501-1510, (1972).

49 L. J. D. Sully. "The Thermal Interface Between Casting and Chill Molds", **AFS Rransactions**, Vol. 84, pp. 735-744, (1976).

50 F. Chiesa. "Measurment of the Thermal Conductance at the Mold/Metal Interface of Permanent Molds", **AFS Transactions**, Vol. 98, pp. 193-200, (1990).

51 A. M. Assar. "Mould surface roughness and interfacial heat transfer using heat flow model", **Materials Science and Technology**, Vol. 13, pp. 702-704, (1997).

52 F. Michel, P. R. Louchez and F. H. Samuel. "Heat Transfer Coefficient During Solidification of Al-Si Alloys: Effects of Mold Temperature, Coating Type and Thickness", **AFS Transactions**, Vol. 103, pp. 275-283, (1995).

53 R. Venkataramani and C. Ravindran. "Effects of Coating Thicknesses and Pouring Temperature on Thermal Response in LFC", **AFS Transactions**, Vol. 104, (1996).

54 K. Narayan Prabhu, B. Chowdary and N. Venkataraman. "Casting/Mold Thermal Contact Heat Transfer during Solidification of Al-Cu-Si Alloy (LM 21) Plates in Thick and Thin Molds", **Journal of Materials Engineering and Performance**, Vol. 14, pp. 604-609, (2005).

55 I. S. Cho and C. P. Hong. "Evaluation of Heat-Transfer Coefficients at the Casting/Die Interface in Squeeze Casting", **International Journal of Cast Metals Research**, Vol. 9, pp. 227-232, (1996).

56 M. Carroll, C. Walsh and M. M. Makhlouf. "Determination of Effective Interfacial Heat Transfer Coefficient between Metal Moulds and Al Alloy Castings", **AFS Transactions**, Vol. 107, pp. 307-314, (1999).

57 R.-J. Weng, J.-H. Kuo and C.-H. Wu. "Effects of Solid Fraction and Operating Pressure on the Heat Transfer Coefficient at the Casting/Mold Interface for AZ91D Magnesium Alloy", **AFS Transactions**, (2005).

58 J. A. Sekhar, G. J. Abbaschian and R. Mehrabian. "Effect of Pressure on Metal-Die Heat Transfer Coefficient during Solidification", **Materials Science and Engineering**, Vol. 40, pp. 105 - 110, (1979).

59 M. A. Gafur, H. Nasrul and K. Narayan Prabhu. "Effect of Chill Thickness and Superheat on Casting/Chill Interfacial Heat Transfer during Solidification of Commercially Pure Aluminum", **Journal of Materials Processing Technology**, Vol. 133, pp. 257-265, (2003).

60 M. I. R. I. L. G. R. P. Tavares. "Roll-Strip Interfacial Heat Fluxes in Twin-Roll Casting of Low-Carbon Steels and Their Effects on Strip Microstructure", **ISIJ International**, Vol. 38, n. 12, pp. 1353-1361, (1998).

61 M. I. J. S. K. R. P. T. R. I. L. Guthrie. "Measurements, Simulation, and Analyses of Instantaneous Heat Fluxes from Solidifying Steels to the Surfaces of Twin Roll Casters and of Aluminum to Plasma-Coated Metal Substrates", **Metallurgical and Materials Transactions B**, Vol. 31B, pp. 1031-1047, (2000).

62 R. P. T. R. I. L. Guthrie. "Mathematical and physical modeling of steel flow and solidification in twin-roll/horizontal belt thin-strip casting", **Applied Mathematical Modeling**, Vol. 22, pp. 851-872, (1998).

63 C. O. Hlady, J. K. Brimacombe and I. V. Samarasekera. "Heat Transfer in the Hot Rolling of Metals", **METALLURGICAL AND MATERIALS TRANSACTIONS B**, Vol. 26B, pp. 1019-1027, (1995 October).

64 R. Steiner. **ASM Handbook Volume 1:** Properties and Selection: Irons, Steels, and High-Performance Alloys. [S.l.]: American Society for Metals , v. I.

65 Y. Plevachuk, **Journal of Materials Science: Materials in Electronics**, (2010).

66 CONAX Technologies. Disponivel em: <http://www.conaxbuffalo.com/details.aspx?cid=PG&pid=PG>.

67 B. Giordanengo. "Thermal Conductivity of Liquid. Metals and Metallic Alloys", **J. Non-Cryst. Solids**, pp. 250-252, (1999).

68 D. Samborsky. UNIVERSAL TESTING MACHINES, MSU SUMMARY. Disponivel em: <http://www.coe.montana.edu/composites/documents/Equipment%20July%202008.pdf>.

69 MTS. Disponivel em: <http://www.mts.com/407/product_literature/profile4.htm>.

70 N. Instruments. Disponivel em: <http://zone.ni.com/devzone/cda/tut/p/id/3638>.

Appendix A: Calculations of Thermocouple 1 Position Inside the Chill Part

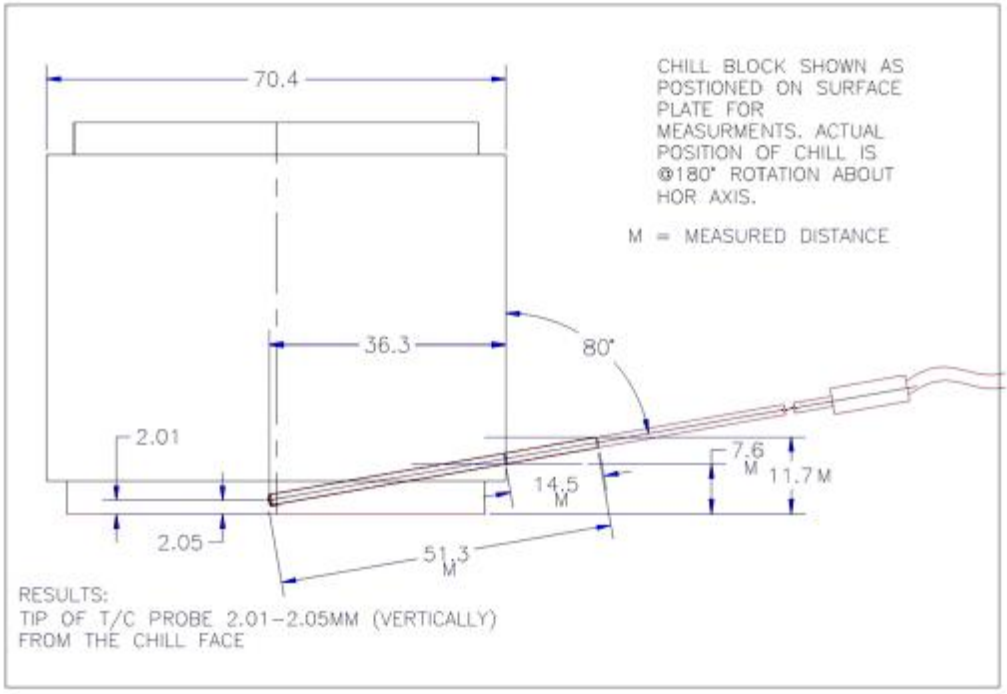

Figure 1 Location of Thermocouple 1, inside the chill part

Position of the thermocouple 1 and thermocouple 2 are very critical because of the sensitivity of the inverse code to the positions of the thermocouples. After drilling a hole to put the thermocouple 1(TC1) at 2 mm below the interface it was necessary to double check the exact position of the hole. As it is shown in Figure 1, it was measured that the angle of the position is exactly 10° with the depth of 36.8mm.

By considering the diameter of the thermocouple, which is 1.5mm, we have:

$$\sin 10 * 51.3mm = 8.908mm$$

$$11.7mm - 8.908mm = 2.792mm$$

$$2.792mm - \left(\frac{1.5}{2}\right) = 2.042mm$$

Appendix B: Complementary Sketches and Dimensions of the Apparatus

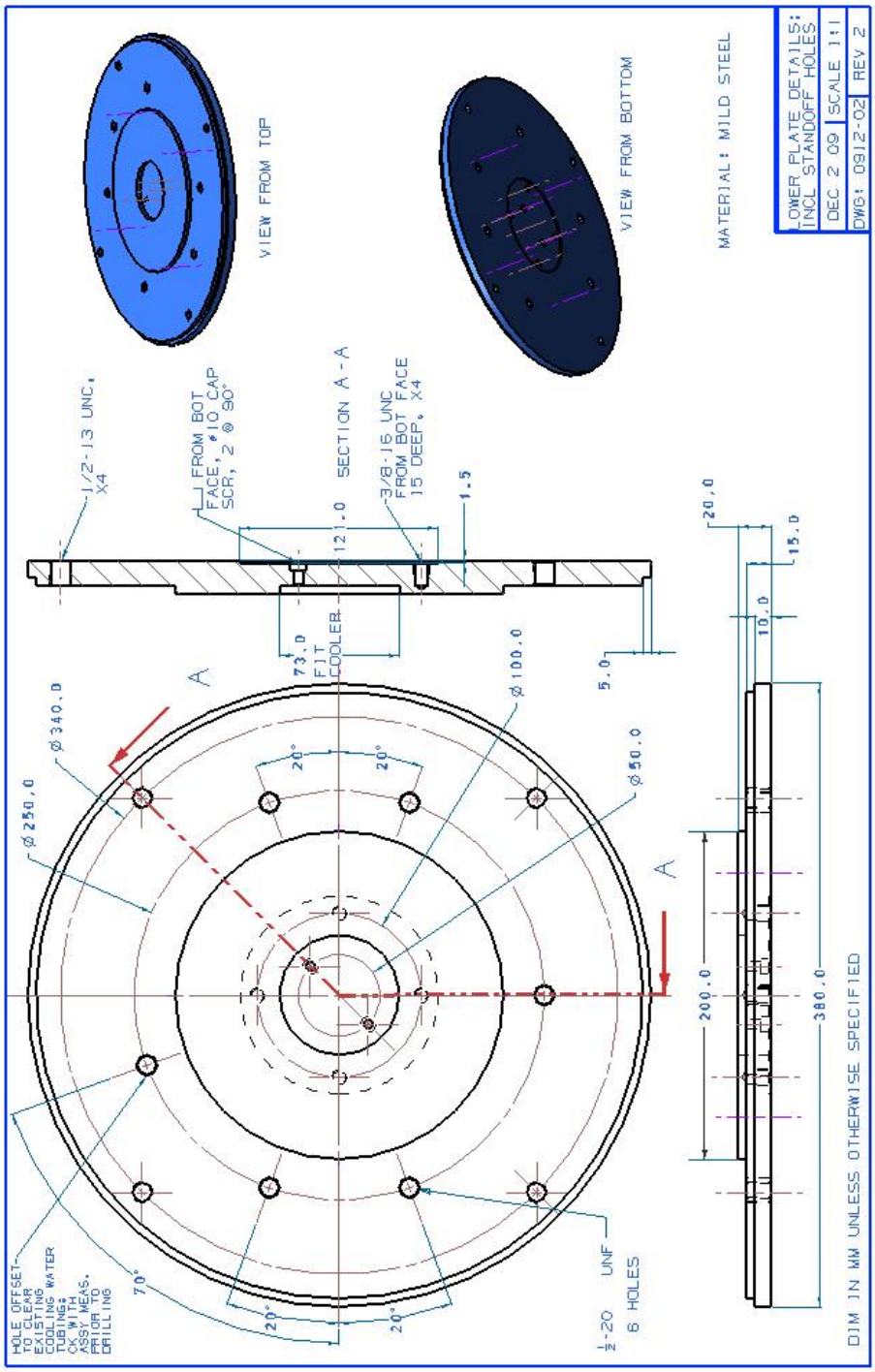

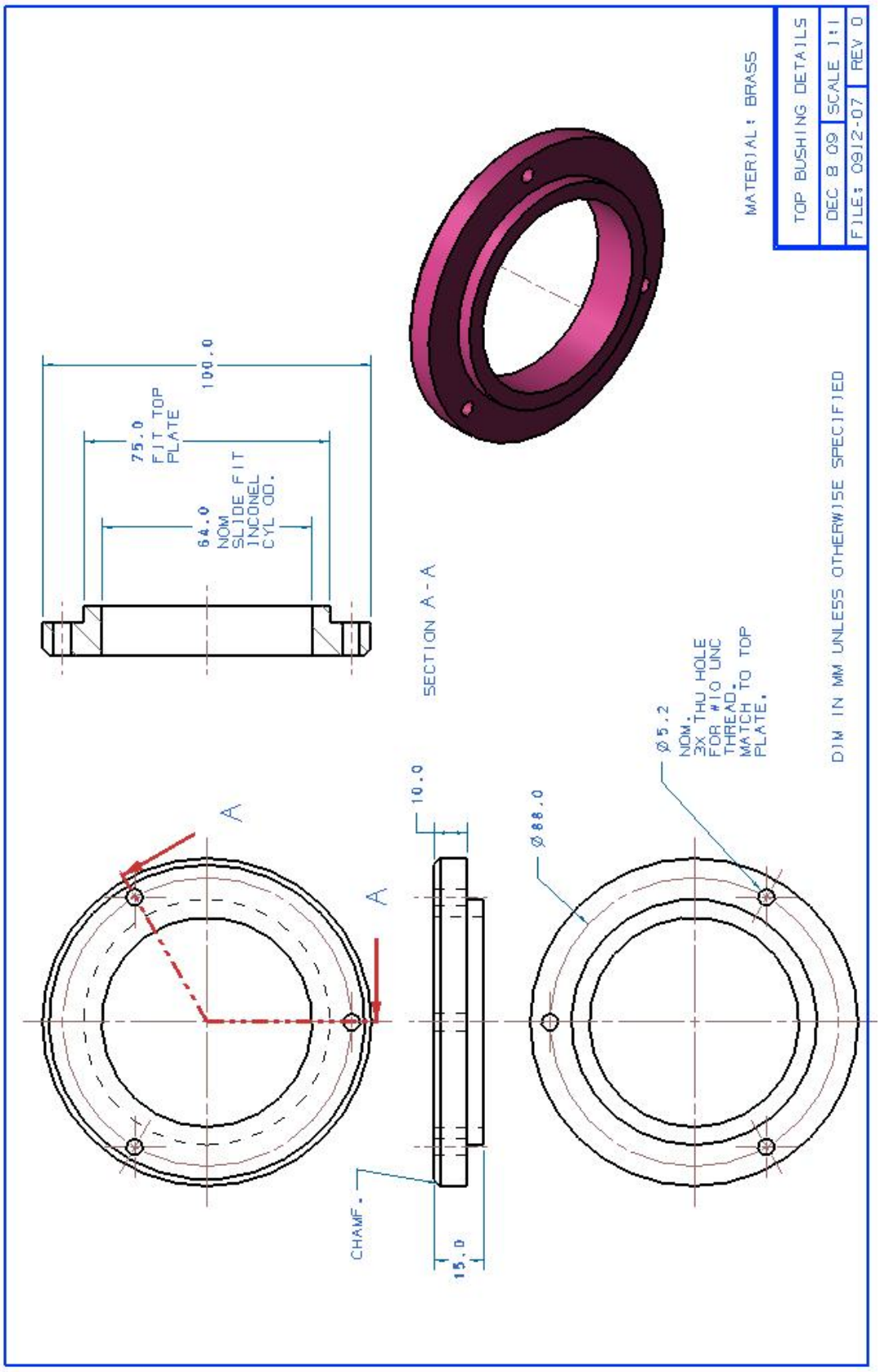
TOP BUSHING DETAILS
DEC 8 09
SCALE 1:1
FILE: 0912-07
REV 0
MATERIAL: BRASS
DIM IN MM UNLESS OTHERWISE SPECIFIED
100.0
75.0
FIT TOP PLATE
64.0
NOM SLIDE FIT INCONEL CYL OD.
SECTION A-A
A
A
10.0
Ø88.0
Ø5.2
NOM.
3X THU HOLE
FOR #10 UNC
THREAD.
MATCH TO TOP
PLATE.
CHAMF.
15.0

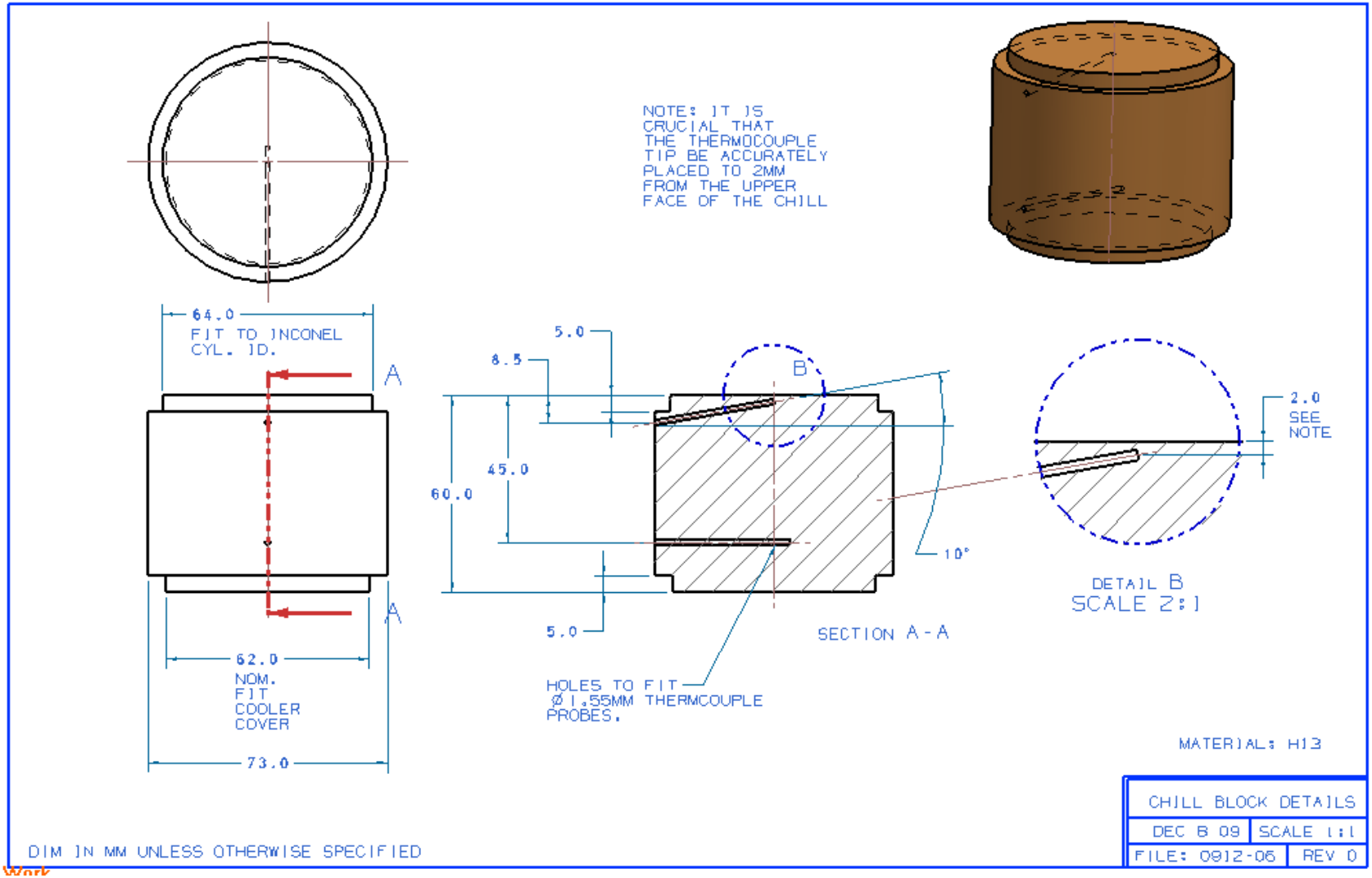
NOTE: IT IS CRUCIAL THAT THE THERMOCOUPLE TIP BE ACCURATELY PLACED TO 2MM FROM THE UPPER FACE OF THE CHILL
64.0
FIT TO INCONEL CYL. ID.
A
A
62.0
NOM. FIT COOLER COVER
73.0
5.0
8.5
45.0
60.0
5.0
B
10°
SECTION A-A
HOLES TO FIT Ø1.55MM THERMCOUPLE PROBES.
2.0
SEE NOTE
DETAIL B
SCALE 2:1
MATERIAL: H13
DIM IN MM UNLESS OTHERWISE SPECIFIED
CHILL BLOCK DETAILS
DEC 8 09
SCALE 1:1
FILE: 0912-06
REV 0

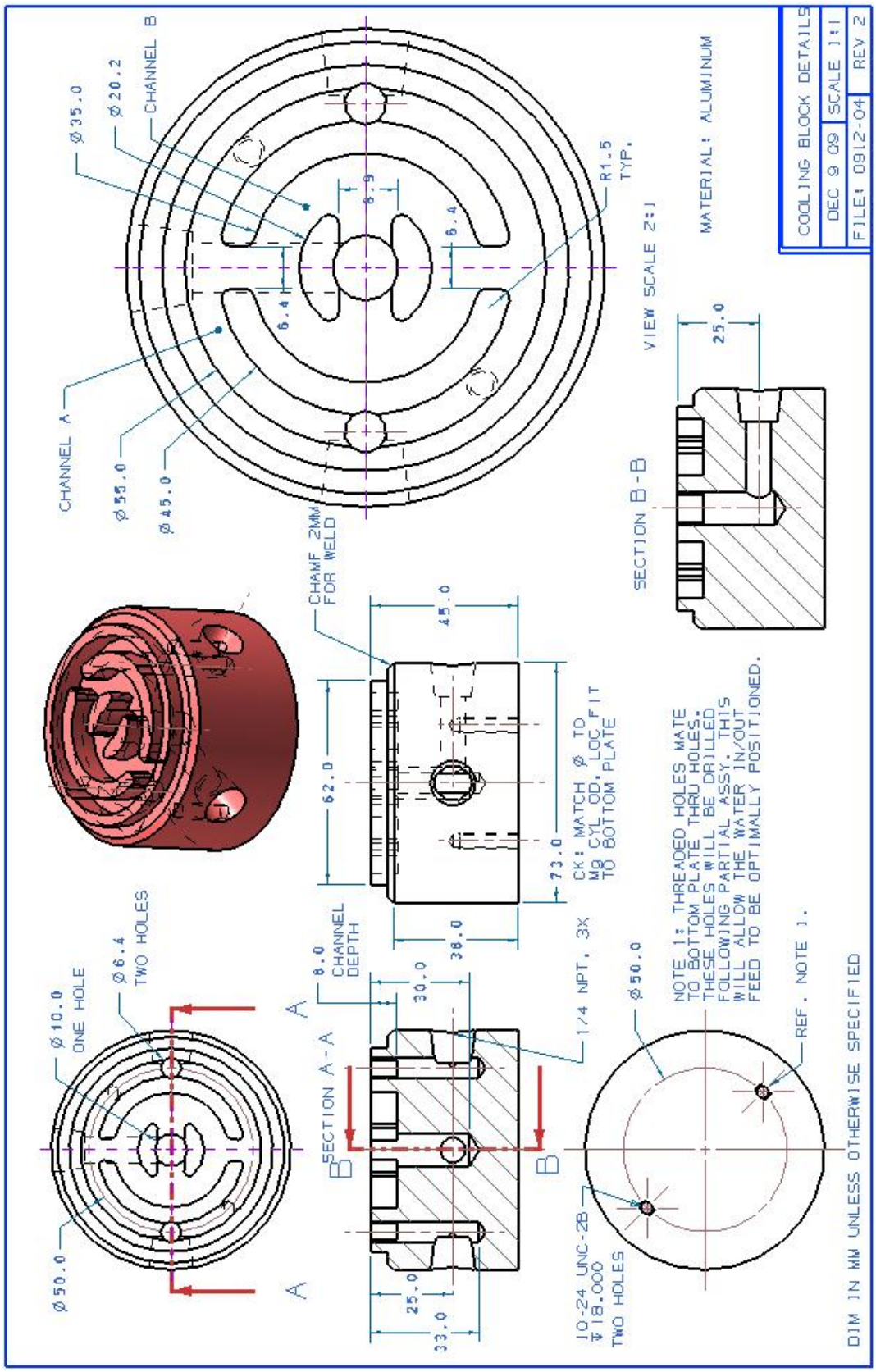
COOLING BLOCK DETAILS
DEC 9 09
SCALE 1:1
FILE: 0912-04
REV 2
MATERIAL: ALUMINUM
CHANNEL A
CHANNEL B
Ø35.0
Ø20.2
Ø55.0
Ø45.0
6.4
6.4
6.9
R1.5 TYP.
VIEW SCALE 2:1
SECTION B-B
25.0
CHAMF 2MM FOR WELD
62.0
45.0
73.0
38.0
8.0 CHANNEL DEPTH
30.0
SECTION A-A
1/4 NPT, 3X
CK: MATCH Ø TO Mø CYL OD, LOC FIT TO BOTTOM PLATE
Ø10.0 ONE HOLE
Ø6.4 TWO HOLES
Ø50.0
25.0
33.0
Ø50.0
NOTE 1: THREADED HOLES MATE TO BOTTOM PLATE THRU HOLES. THESE HOLES WILL BE DRILLED FOLLOWING PARTIAL ASSY. THIS WILL ALLOW THE WATER IN/OUT FEED TO BE OPTIMALLY POSITIONED.
REF. NOTE 1.
10-24 UNC-2B ↧18.000 TWO HOLES
DIM IN MM UNLESS OTHERWISE SPECIFIED

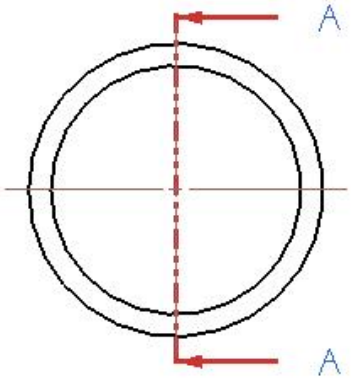

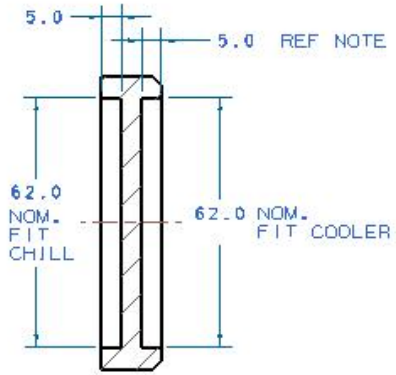

SECTION A-A

NOTE: SET DEPTH SO THAT THE LARGER FLAT SURFACE OF THE COVER CONTACTS THE UPPER FACE OF THE COOLER CHANNELS.

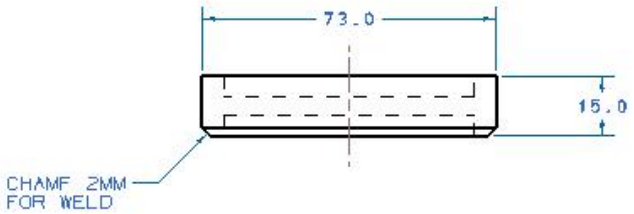

MATERIAL: ALUMINUM

DIM IN MM UNLESS OTHERWISE SPECIFIED

TOP PLATE DETAILS	
DEC 8 09	SCALE 1:1
FILE: 0912-05	REV 0

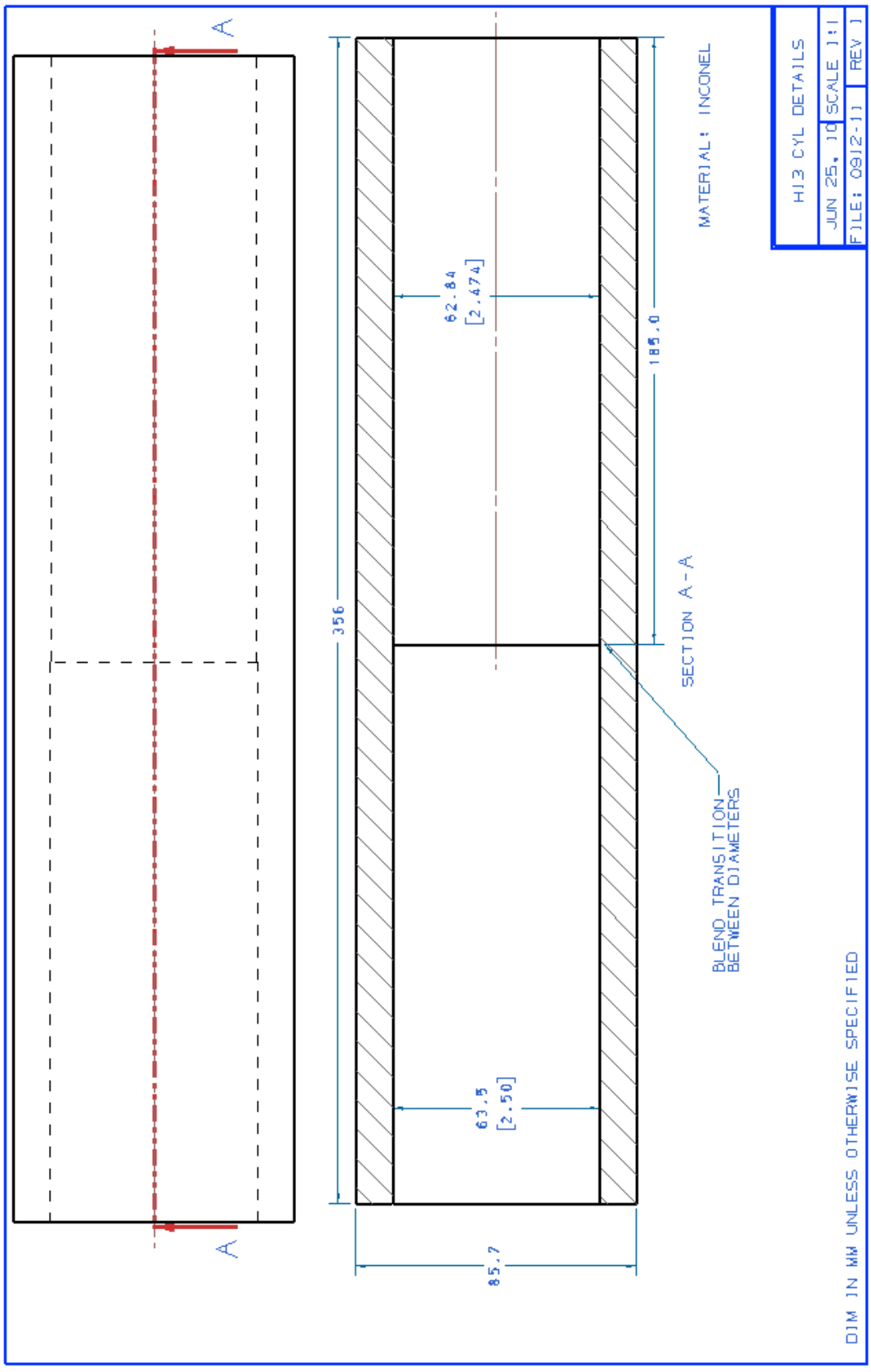
A
A
356
62.84
[2.474]
185.0
63.5
[2.50]
85.7
SECTION A-A
MATERIAL: INCONEL
BLEND TRANSITION
BETWEEN DIAMETERS
H13 CYL DETAILS
JUN 25, 10
SCALE 1:1
FILE: 0912-11
REV 1
DIM IN MM UNLESS OTHERWISE SPECIFIED

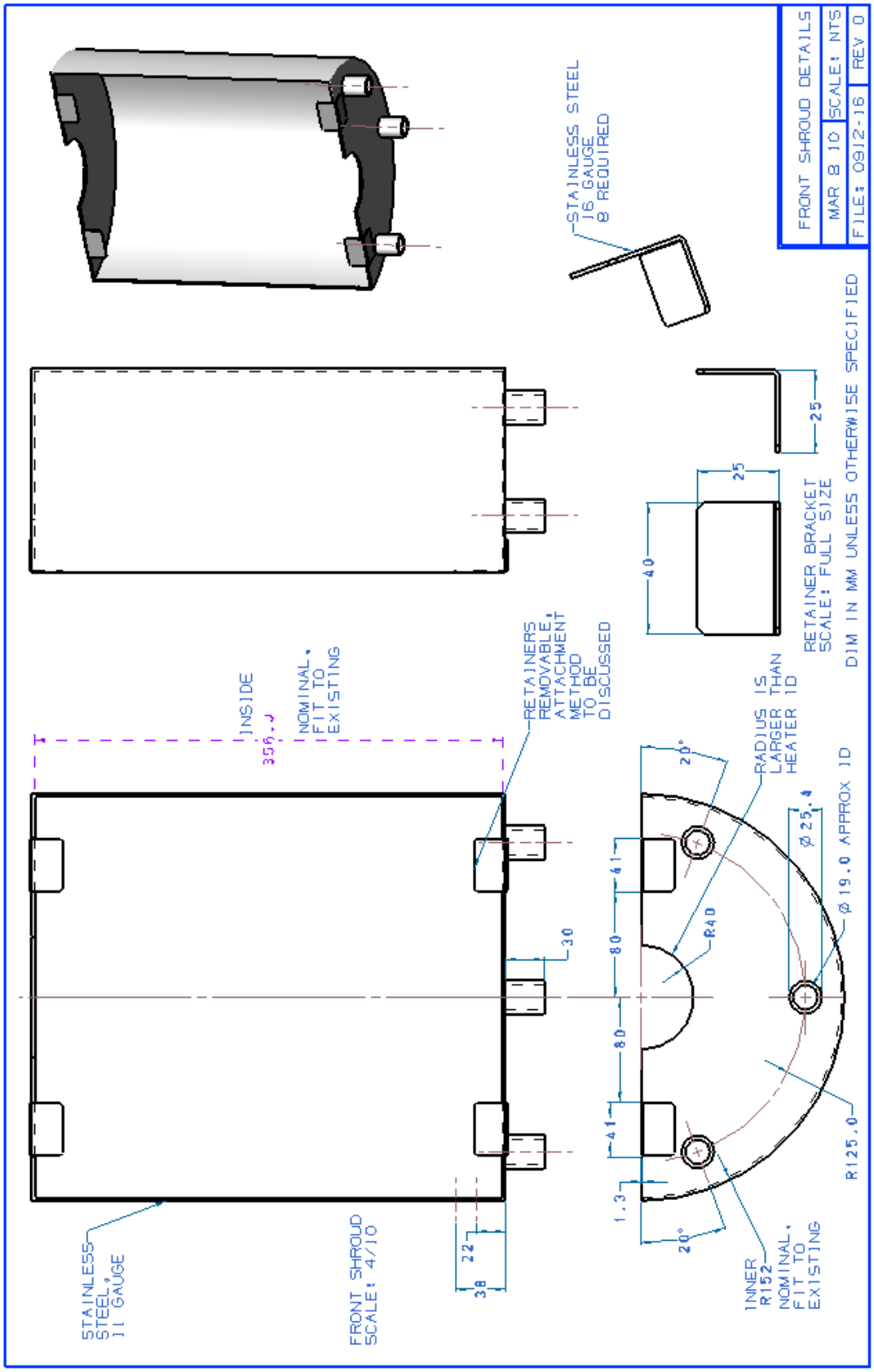
FRONT SHROUD DETAILS
MAR 8 10
SCALE: NTS
FILE: 0912-16
REV 0
STAINLESS STEEL 16 GAUGE 8 REQUIRED
DIM IN MM UNLESS OTHERWISE SPECIFIED
RETAINER BRACKET SCALE: FULL SIZE
25
40
INSIDE 356.0 NOMINAL, FIT TO EXISTING
RETAINERS REMOVABLE, ATTACHMENT METHOD TO BE DISCUSSED
RADIUS IS LARGER THAN HEATER ID
Ø19.0 APPROX ID
Ø25.4
R40
R125.0
INNER R152 NOMINAL, FIT TO EXISTING
STAINLESS STEEL, 11 GAUGE
FRONT SHROUD SCALE: 4/10
30
22
38
41
80
80
41
1.3
20°
20°

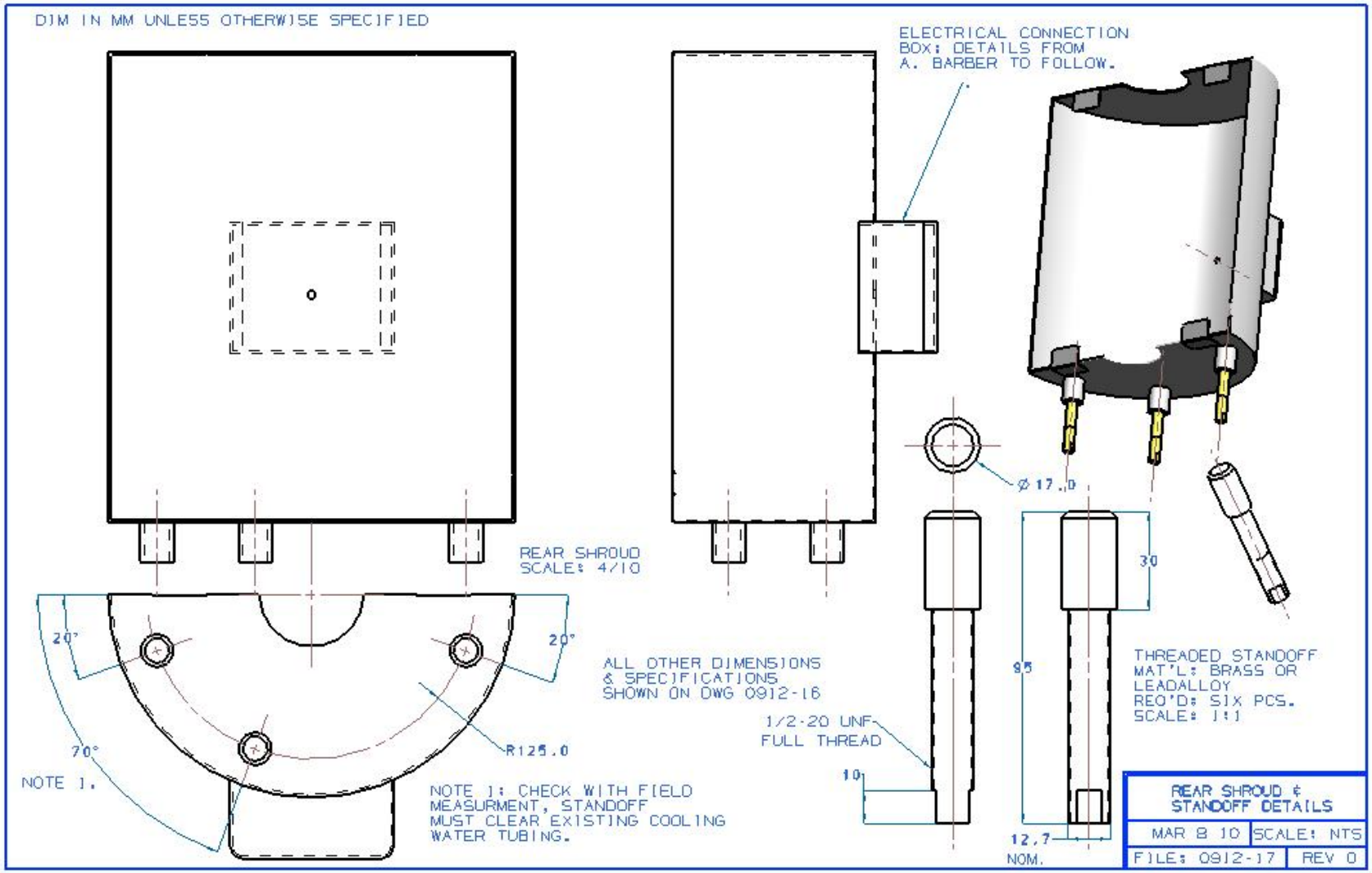
DIM IN MM UNLESS OTHERWISE SPECIFIED
ELECTRICAL CONNECTION BOX: DETAILS FROM A. BARBER TO FOLLOW.
REAR SHROUD SCALE: 4/10
20°
20°
70°
R125.0
NOTE 1.
NOTE 1: CHECK WITH FIELD MEASURMENT, STANDOFF MUST CLEAR EXISTING COOLING WATER TUBING.
ALL OTHER DIMENSIONS & SPECIFICATIONS SHOWN ON DWG 0912-16
1/2-20 UNF FULL THREAD
10
Ø 17.0
30
95
12.7 NOM.
THREADED STANDOFF
MAT'L: BRASS OR LEADALLOY
REQ'D: SIX PCS.
SCALE: 1:1
REAR SHROUD & STANDOFF DETAILS
MAR 8 10
SCALE: NTS
FILE: 0912-17
REV 0

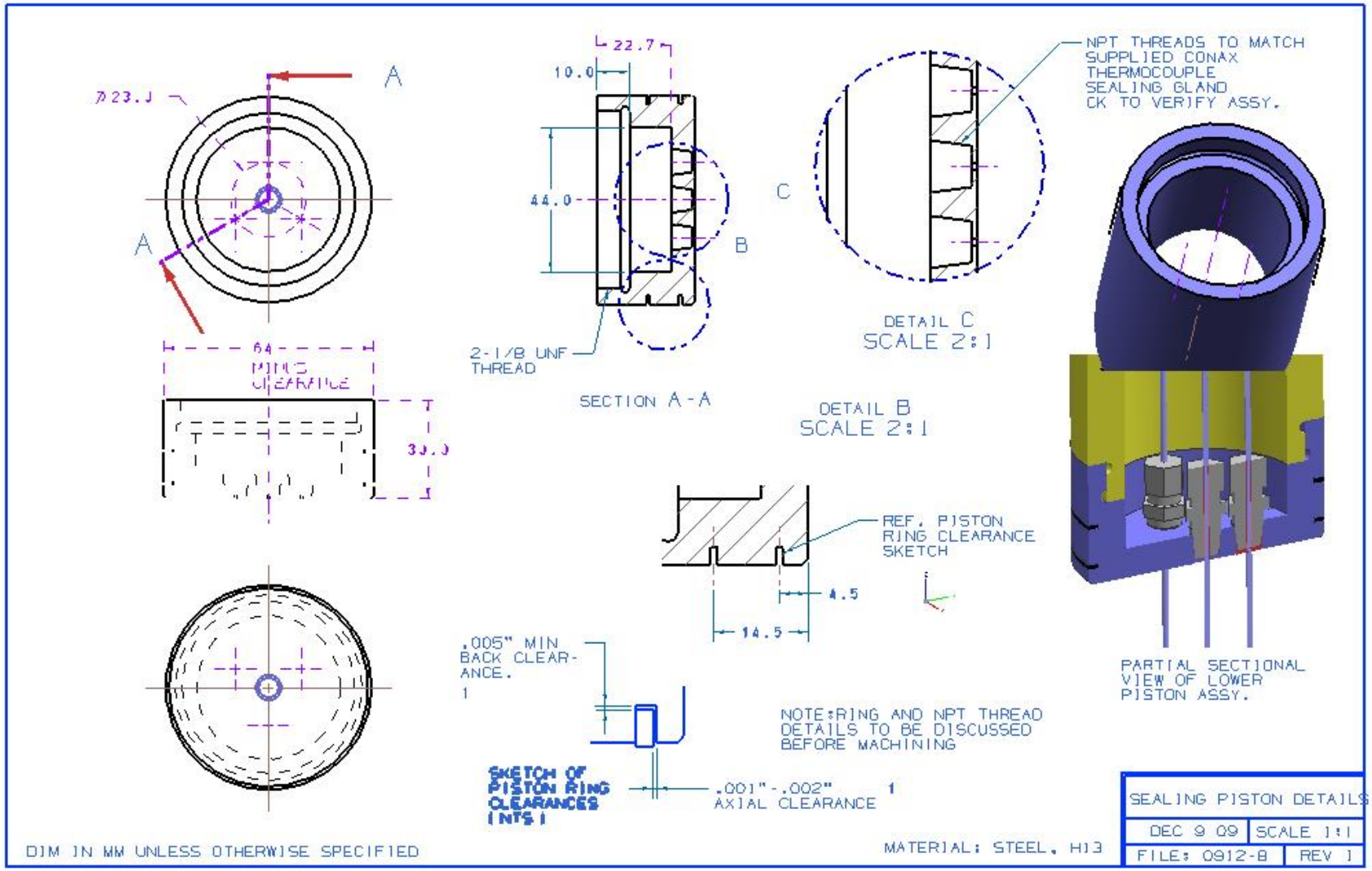
Ø23.J
A
A
64
MIN'D
CLEARANCE
3J.J
22.7
10.0
44.0
B
2-1/8 UNF
THREAD
SECTION A-A
C
DETAIL C
SCALE 2:1
NPT THREADS TO MATCH
SUPPLIED CONAX
THERMOCOUPLE
SEALING GLAND
CK TO VERIFY ASSY.
DETAIL B
SCALE 2:1
REF. PISTON
RING CLEARANCE
SKETCH
4.5
14.5
.005" MIN
BACK CLEAR-
ANCE.
1
SKETCH OF
PISTON RING
CLEARANCES
(NTS)
.001"-.002"
AXIAL CLEARANCE
1
NOTE:RING AND NPT THREAD
DETAILS TO BE DISCUSSED
BEFORE MACHINING
PARTIAL SECTIONAL
VIEW OF LOWER
PISTON ASSY.
DIM IN MM UNLESS OTHERWISE SPECIFIED
MATERIAL: STEEL, H13
SEALING PISTON DETAILS
DEC 9 09
SCALE 1:1
FILE: 0912-8
REV 1

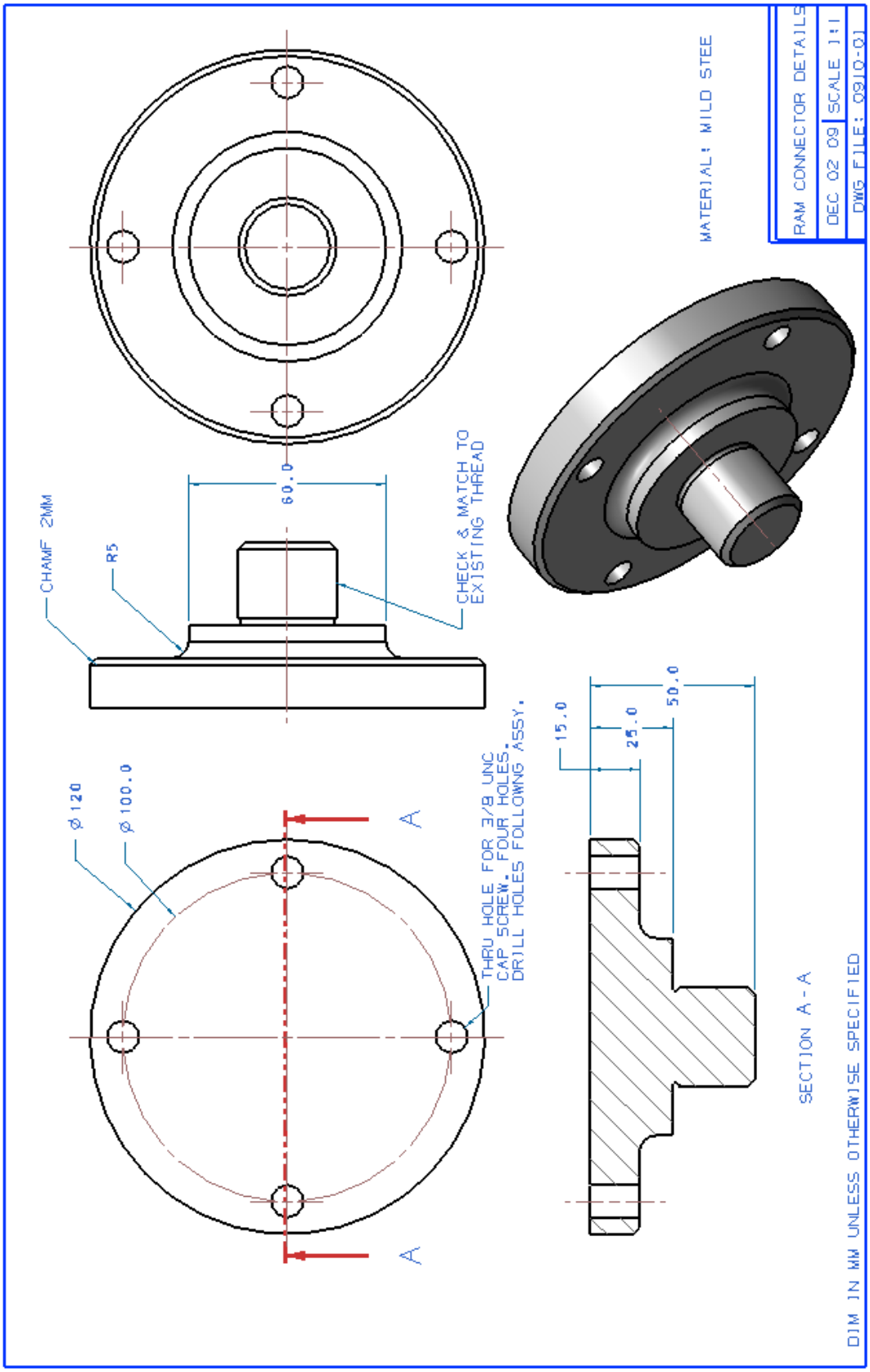
RAM CONNECTOR DETAILS
DEC 02 09 SCALE 1:1
DWG FILE: 0910-01
MATERIAL: MILD STEE
CHAMF 2MM
R5
60.0
CHECK & MATCH TO EXISTING THREAD
Ø120
Ø100.0
A
A
THRU HOLE FOR 3/8 UNC CAP SCREW. FOUR HOLES. DRILL HOLES FOLLOWING ASSY.
15.0
25.0
50.0
SECTION A-A
DIM IN MM UNLESS OTHERWISE SPECIFIED

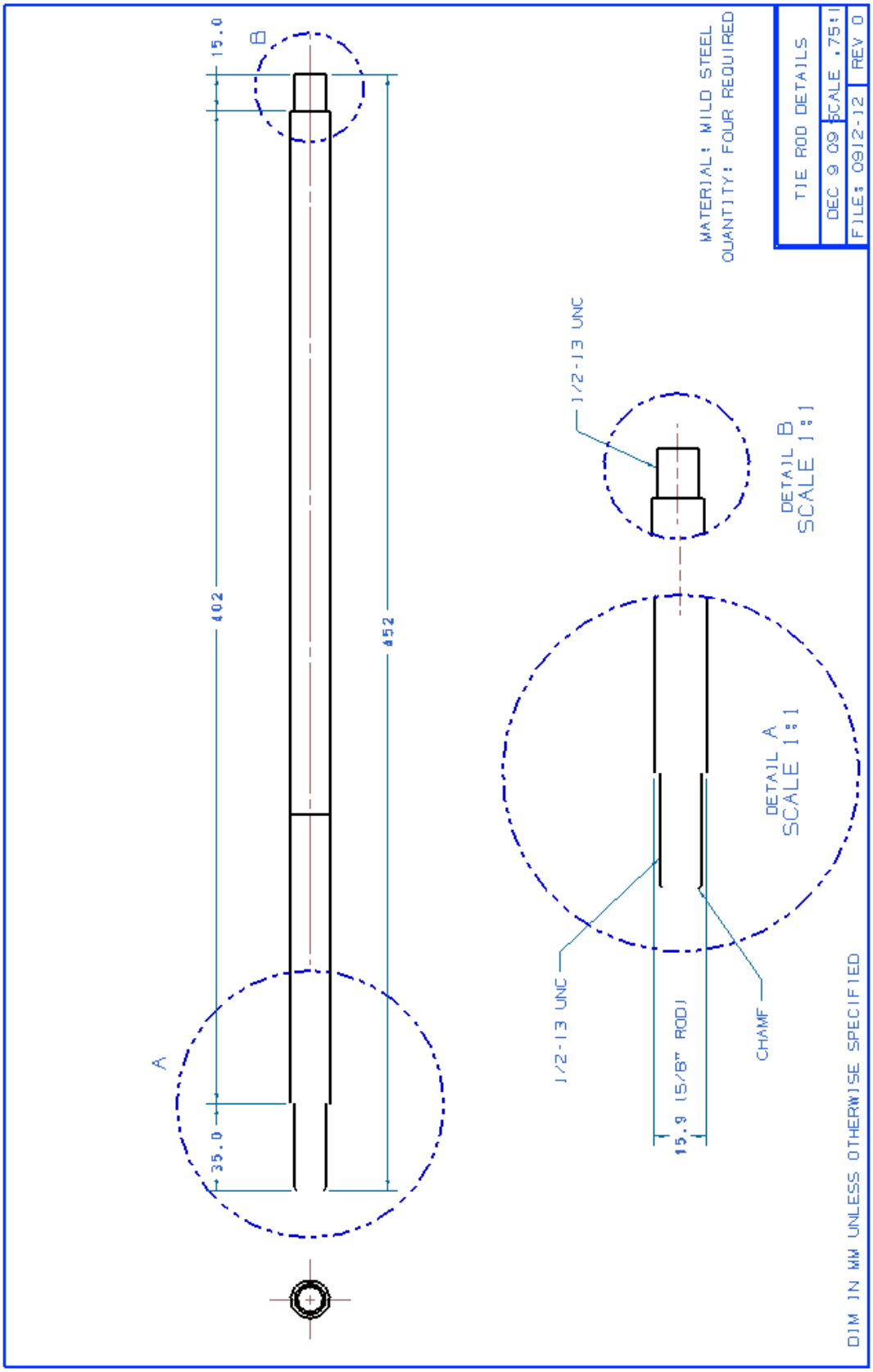
TIE ROD DETAILS
DEC 9 09
SCALE .75:1
FILE: 0912-12
REV 0
MATERIAL: MILD STEEL
QUANTITY: FOUR REQUIRED
DIM IN MM UNLESS OTHERWISE SPECIFIED
15.0
B
402
452
35.0
A
1/2-13 UNC
DETAIL B
SCALE 1:1
DETAIL A
SCALE 1:1
1/2-13 UNC
15.9 (5/8" ROD)
CHAMF

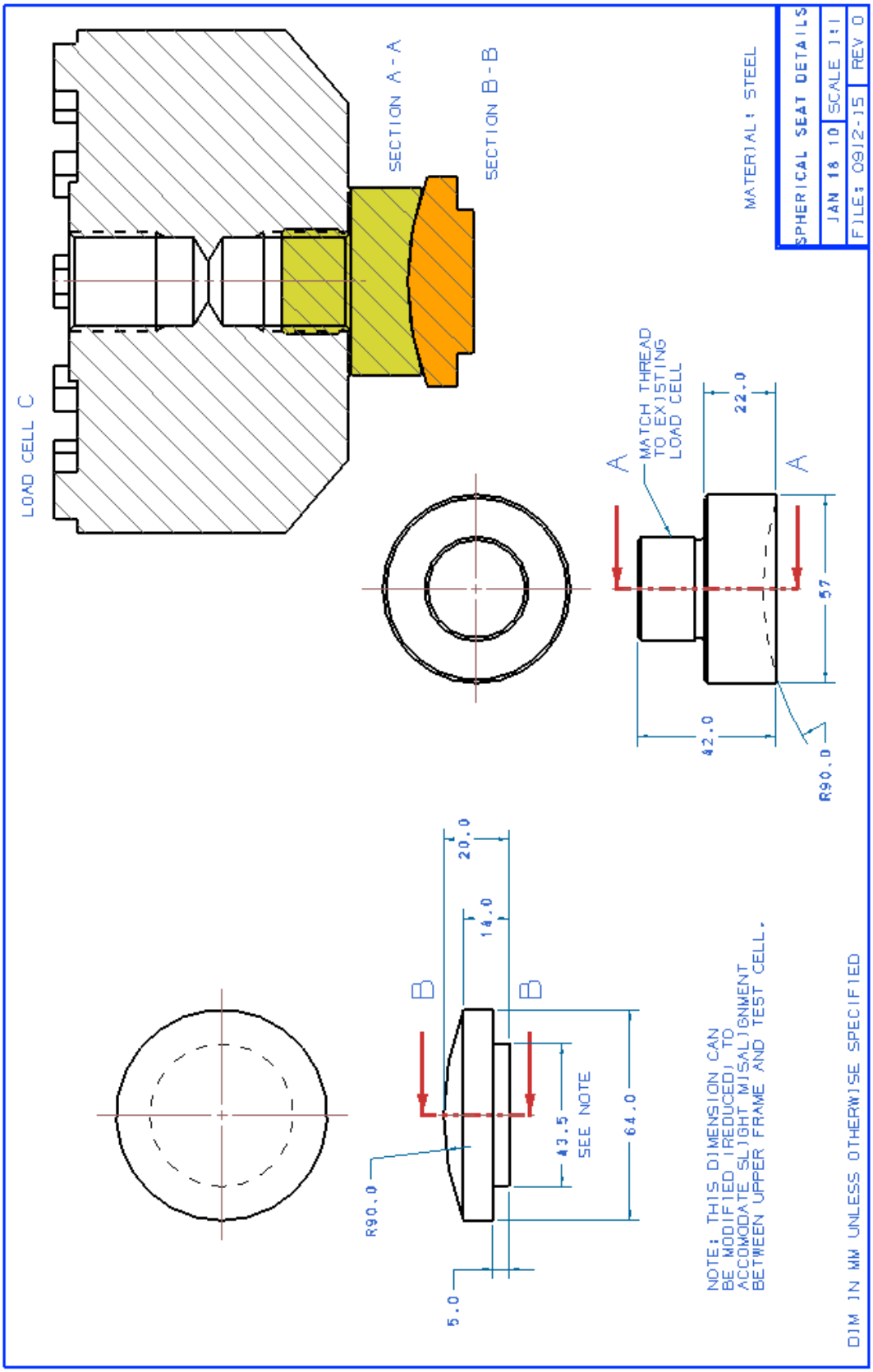
SPHERICAL SEAT DETAILS
JAN 16 10
SCALE 1:1
FILE: 0912-15
REV 0
MATERIAL: STEEL
LOAD CELL C
SECTION A-A
SECTION B-B
A
MATCH THREAD
TO EXISTING
LOAD CELL
22.0
57
42.0
R90.0
B
20.0
14.0
43.5
SEE NOTE
64.0
R90.0
5.0
NOTE: THIS DIMENSION CAN
BE MODIFIED IREDUCED) TO
ACCOMODATE SLIGHT MISALIGNMENT
BETWEEN UPPER FRAME AND TEST CELL.
DIM IN MM UNLESS OTHERWISE SPECIFIED

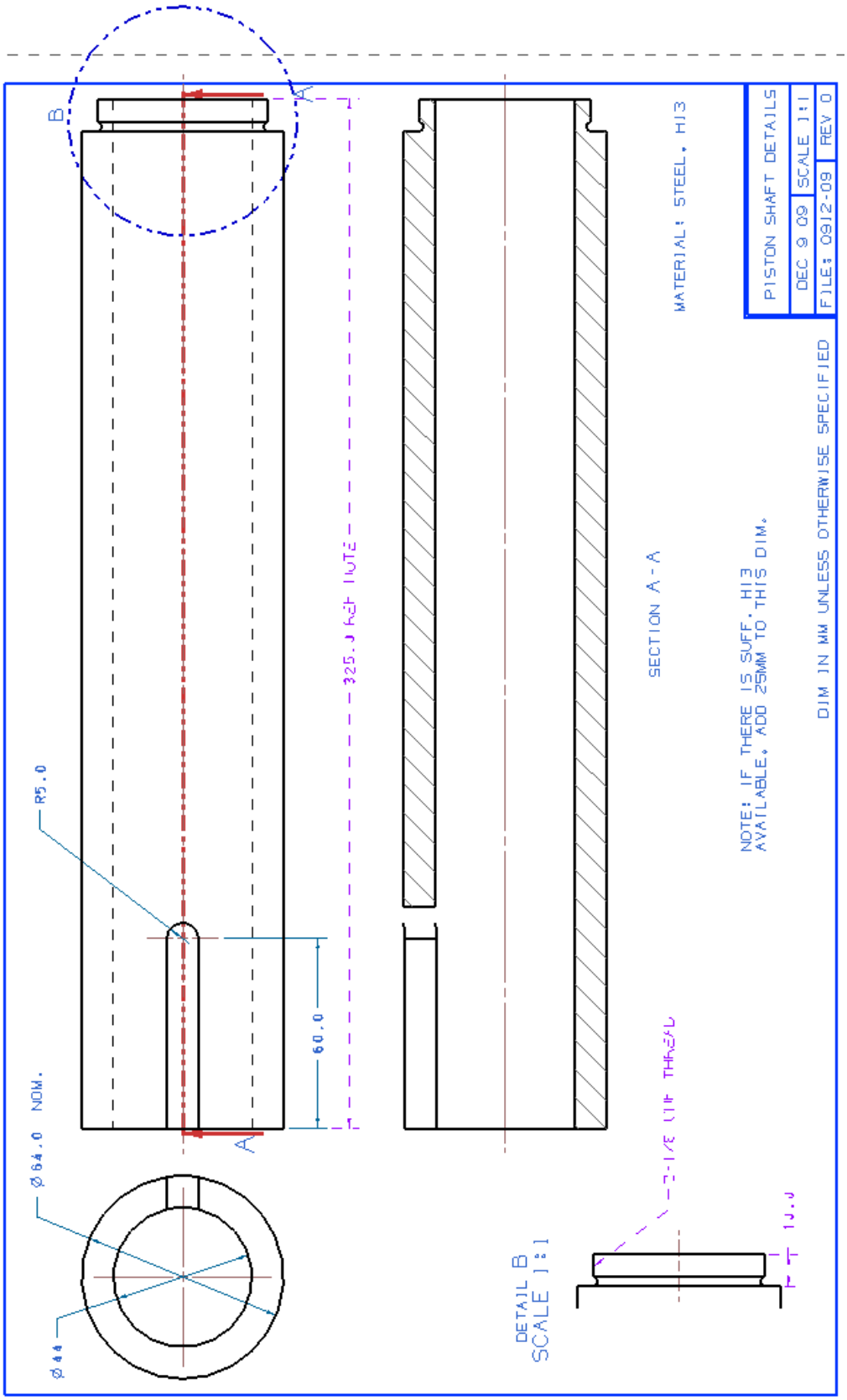
B
A
325.0 REF NOTE
R5.0
60.0
Ø64.0 NOM.
Ø44
SECTION A-A
MATERIAL: STEEL, H13
NOTE: IF THERE IS SUFF. H13
AVAILABLE, ADD 25MM TO THIS DIM.
DETAIL B
SCALE 1:1
PISTON SHAFT DETAILS
DEC 9 09
SCALE 1:1
FILE: 0912-09
REV 0
DIM IN MM UNLESS OTHERWISE SPECIFIED

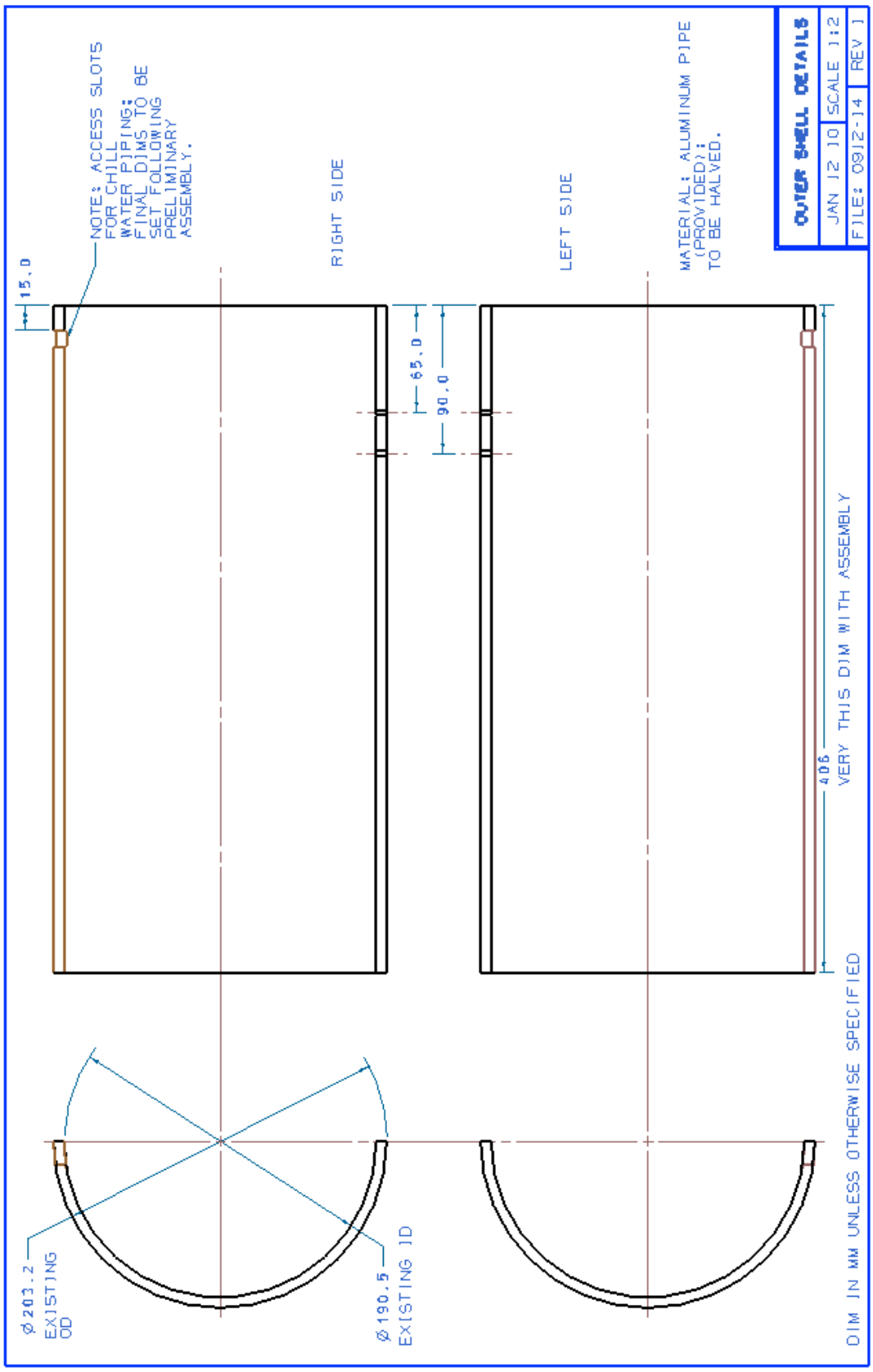
OUTER SHELL DETAILS
JAN 12 10
SCALE 1:2
FILE: 0912-14
REV 1
NOTE: ACCESS SLOTS FOR CHILL WATER PIPING; FINAL DIMS TO BE SET FOLLOWING PRELIMINARY ASSEMBLY.
MATERIAL: ALUMINUM PIPE (PROVIDED); TO BE HALVED.
RIGHT SIDE
LEFT SIDE
15.0
65.0
90.0
406
VERY THIS DIM WITH ASSEMBLY
Ø203.2 EXISTING OD
Ø190.5 EXISTING ID
DIM IN MM UNLESS OTHERWISE SPECIFIED

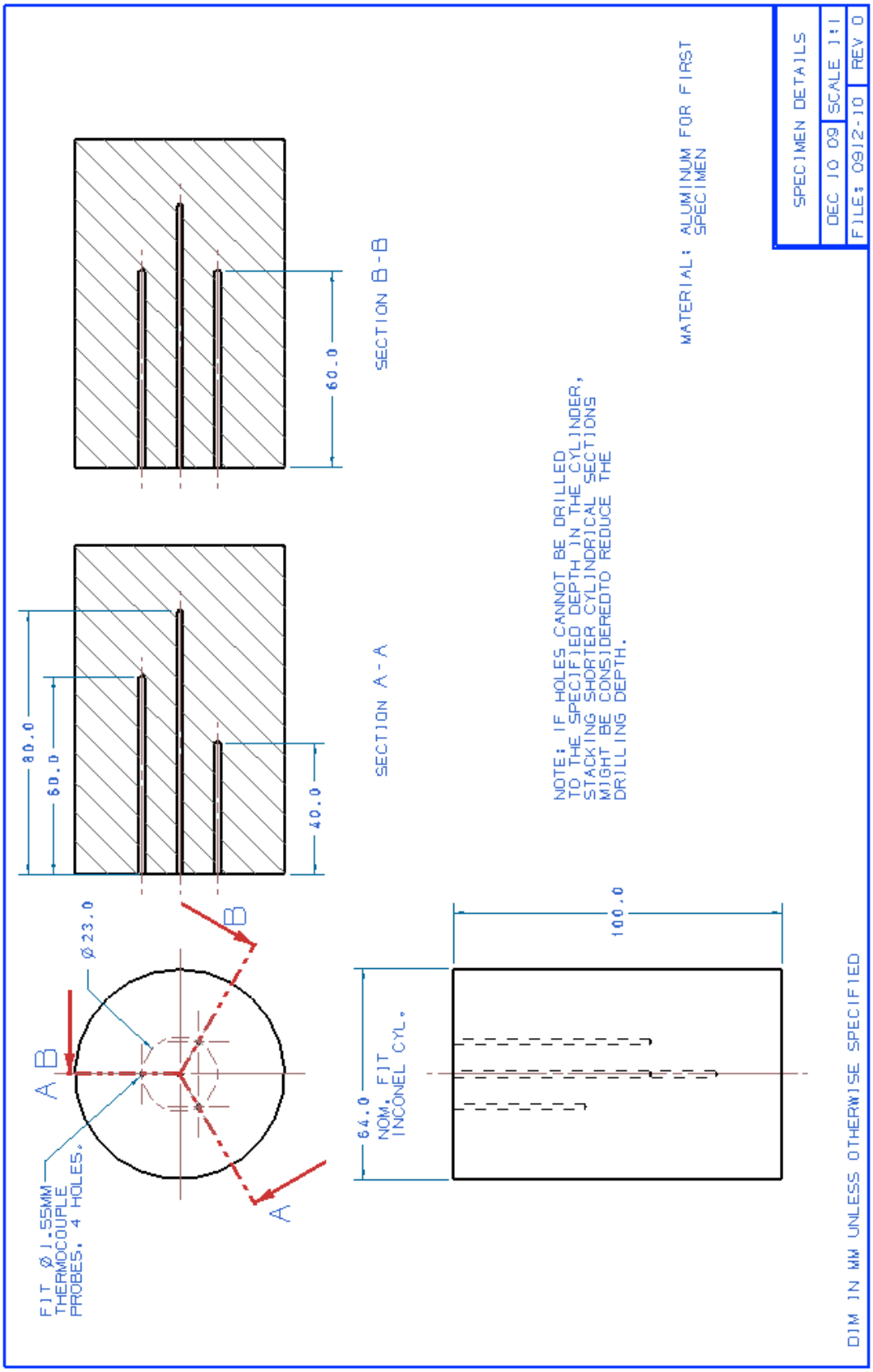
SPECIMEN DETAILS
DEC 10 09
SCALE 1:1
FILE: 0912-10
REV 0
MATERIAL: ALUMINUM FOR FIRST SPECIMEN
NOTE: IF HOLES CANNOT BE DRILLED TO THE SPECIFIED DEPTH IN THE CYLINDER, STACKING SHORTER CYLINDRICAL SECTIONS MIGHT BE CONSIDERED TO REDUCE THE DRILLING DEPTH.
SECTION B-B
SECTION A-A
60.0
80.0
60.0
40.0
100.0
64.0
NOM. FIT
INCONEL CYL.
Ø23.0
A
B
A
B
FIT Ø1.55MM
THERMOCOUPLE
PROBES, 4 HOLES.
DIM IN MM UNLESS OTHERWISE SPECIFIED

Appendix C: Wiedemann-Franz Relation

$$l = \left(\frac{k_B^2 p^2}{3e^2} - S^2 \right) s\,T$$

$\frac{k_B^2 p^2}{3e^2} \approx 2.44 \times 10^{-8} W\Omega K^{-2}$, S is the absolute thermo-power. For tin alloys Giordanengo et al [67] show that the thermo-power is almost null and thus

$$l = \frac{k_B^2 p^2}{3e^2} s\,T$$

For homogenous solution with a dominant element (in the present case Sn) we use a CALPHAD type model

$$l^j\left(T, \underline{\underline{x}}\right) = l^{Sn}(T) + \sum_i k_i c_i$$

Where k_i describes the effect of the solutes i and Ci is the composition of the solute in Wt. %.

For a semi-solid (in a solid-liquid equilibria region) the thermal conductivity can be expressed as

$$l(T) = \left(1 + A_{mix}\right) f^L l_L(T) + \left(1 - f^L\right) l_L(T)$$

f^L is the liquid and solid fraction and A_{mix} is a constant value parameter describing the effect of liquid convection upon the thermal conductivity.

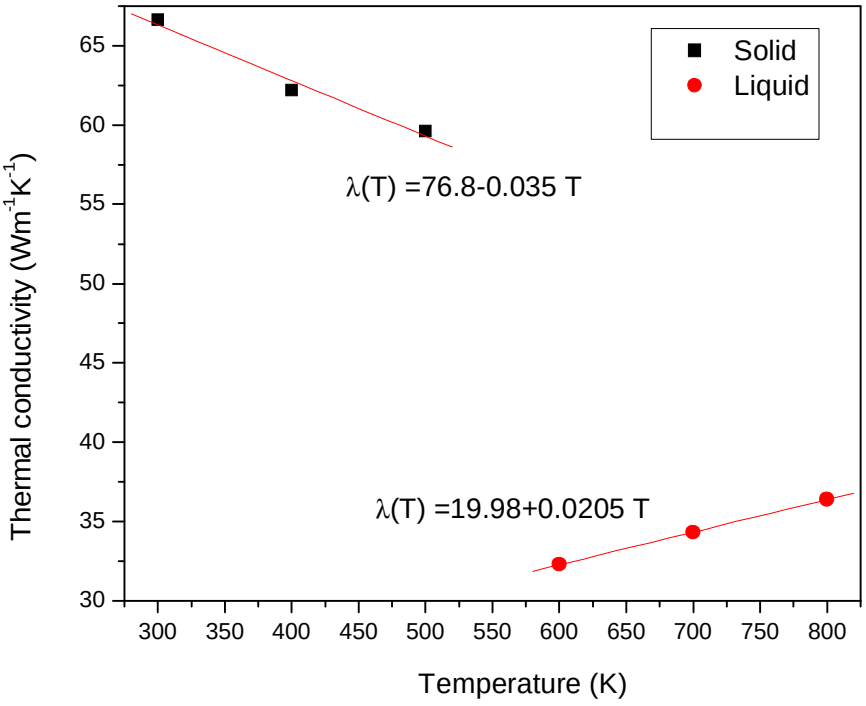

Figure 2 Pure Sn

Appendix D: Load cell, Servo Hydraulic Universal Testing Machine, MTS 407 Controller, and Data Acquisition System

A load cell is a transducer that is used to convert a force into electrical signal. This conversion is indirect and happens in two stages. Through a mechanical arrangement, the force being sensed deforms a strain gauge. The strain gauge converts the deformation (strain) to electrical signals. A load cell usually consists of four strain gauges in a Wheatstone bridge configuration. Load cells of one strain gauge (quarter bridge) or two strain gauges (half bridge) are also available. The electrical signal output is typically in the order of a few millivolts and requires amplification by an instrumentation amplifier before it can be used. The output of the transducer is plugged into an algorithm to calculate the force applied to the transducer.

Servo Hydraulic Universal Testing Machine[68]

Instron1350 computer controlled servo hydraulic universal testing machine is mainly used to execute the tension, compression, bending, flexural etc. The oil cylinder is at the bottom of the load frame. Tension space is at the upside and compression and bending spaces are between lower crosshead and working table. It is adopting oil hydraulic power to push the piston in the oil cylinder to provide loading force. The lower crosshead is driven by the motor and gear inside it to realize the adjustment of testing space. The leading screws are fixed into the machine seat. Table 1 illustrates the specification of Instron 1350.

Table 13 Specification of Instron 1350[68]

	Model	SN	
Frame	8500R-C1910 1350-0017	C1910	
Actuator	3308-004		±98 KN static
Stroke			±50 mm
Servovalve	3320 403 (Moog A076-585)	113	5 GPM
Load Cell	3116-135	2133	±98 KN static
Grips	2718-019		
Column Clearance			457 mm
Maximum Clearance with grips			533 mm
Electronics	8500 Plus	C2179	V37.0 / V37.37 /V37.1/V37.1/V37.1 (upgraded 1998)

MTS 407 Controller [69]

The MTS Model 407 Controller, shown in Figure , is a digitally supervised PIDF servo controller that provides complete control of a single channel or station in a mechanical testing system. This includes ac and dc transducer conditioning, basic function generation (with the capability to accept externally generated command signals), servo valve drive signal generation, and hydraulic pressure control. In addition, multiple 407 Controllers can be interconnected to accommodate multiple-channel testing and can be quickly configured to accommodate a variety of tests.

Figure 3 MTS 407 Controller[69]

The 407 Controller provides complete control of the test system hydraulics. The 407 can be used to control a hydraulic power supply and/or a hydraulic service manifold to apply low and high hydraulic pressure to the test system. The 407 can be used with either solenoid controlled (on/off) or proportional type hydraulic service manifolds. It is also compatible with hydraulic power supplies that have either 24 Vdc or line voltage control circuitry. In multiple Controller configurations, the 407 provides first-on/last-off control of the hydraulic power supply in addition to control of a local hydraulic service manifold.

Data Acquisition System[70]

A data acquisition system has two main part: a) The hardware components to receive the sensor signal and b) Software to collect and analyze these measurements. The data acquisition hardware which was employed for this study consisted a 2.0 GHz PC with a plug-in DAQ device, and a national instrument SCXI (DAQ) system.

There are different parts in a SCXI DAQ system with different application in the data gathering process. The SCXI-1303 32-channel isothermal terminal block is a shielded board with screw terminals that connect to the SCXI-1102/B/C and the SCXI-1100 modules. The SCXI-1303 has a high-accuracy thermistor, cold-junction temperature sensor, and an isothermal

copper plane to minimize the temperature gradients across the screw terminals when you measure with thermocouples. The terminal block has 78 screw terminals for easy connection. Thirty-two pairs of screw terminals connect to the 32 differential inputs of the SCXI modules. One pair of terminals connects to the module's chassis ground pins. Three terminals connect to the SCXI module OUTPUT and AOREF pins and to the SCXI bus guard. All of the other terminals—OUT0+, OUT0–, OUT1+, OUT1–, OUT2+, OUT2–, OUT3+, OUT3–, and AIREF—are reserved for future use. The terminal block has a pull up resistor connected between CH+ and +5 V and a bias resistor connected between CH– and chassis ground. These resistors help you detect open thermocouples by detecting saturation of the module amplifier output

Appendix E: Explicit Code

```
clc;
clear all;
%====================================Thermophysical Properties of
Chill=======================
ro=7800;%(kg/m3);
cp=460;%(J/kg K);
alfa=k/(ro*cp);

%============================Problem parameters===============
epsilon=0.01;
delx=5e-4;%m
delt=0.1;%s
F0=alfa*delt/(delx^2);
x=0.0450;%m TC2 position
x3=0.002;%m TC3 position
node=floor(x/delx);%total node number
C=zeros(node-1,1);

Temp=zeros(node-1,1);
Temp2=zeros(node-1,1);

Temp(:,1)=T0;
Temp2(:,1)=T0;
r=4;% future time steps

error=0;
G=0;

for i=1 : node
    X(i)=i;
end;
%===============Reading Temperatures==============
 aa = xlsread('C:\Documents and Settings\mehraram\Desktop\Tin
Tests\data.xlsx',2);
 aa=aa+273;
 b = xlsread('C:\Documents and Settings\mehraram\Desktop\Tin
Tests\data.xlsx',1);
 b=b+273;
 Termocouple_casting=xlsread('C:\Documents and
Settings\mehraram\Desktop\Tin Tests\data.xlsx',3);
```

```
 TC_boundary=aa;
 TC1=b;
 t=length(b);
 T_casting=zeros(t-r,1);
 q_temp=zeros(1,t);
 q_temp2=zeros(1,t);
 q_temp(:)=150000;%guess
 %======= Producing a time matrix to plot the thermocouple measured
times

 time(1)=delt;

 for i=2 : t-r;
     time(i)=time(i-1)+delt;
 end;

   plot(time(:),TC_boundary(:),'-o','LineWidth',1.5,...
                'Color','red',...
                'MarkerEdgeColor','k',...
                'MarkerFaceColor',[0.803921569 0.784313725
0.694117647],...
                'MarkerSize',3)
 h = title('Measured Temperatures by Thermocouple 2');
 set(h,'Interpreter','none')

 xlabel('Time (s)'),
 ylabel('Temperature (K)');
 %============================= Temp profiles ====================

A=zeros(node-1,node-1);
Tt1=zeros(node,1);
Tt=zeros(node,1);
Tt(:,1)=T0;
%========== Matrix A Formation ==============
for i=2 : node-2

        A(i,i-1)=-1*F0;
        A(i,i)= (1+2*F0);
        A(i,i+1)=-1*F0;

end;

=================Thomas elements================

     AA=zeros(node-1,1);
```

```
     AA(:)=1+2*F0;
     BB=zeros(node-1,1);
     BB(:)=-1*F0;
     CC=zeros(node-1,1);
     CC(:)=-1*F0;
     BB(1)=-2*F0;
A_inv=inv(A);
q_error=1;
n=0;
Temp(:,1)=T0;
q_temp1=150000;

for h=1 : t-r
q_error=1;
Temp(:,1)=T0;
Temp2(:,1)=T0;
count=0;
n=n+1
while q_error>0.05
%=================Solvine the equation [A][T]=[C] ====================
%===============Solving for q+ep

Temp(:,1)=T;
Temp2(:,1)=T;
count=count+1;
q_temp2=q_temp1*(1+epsilon);
movaghat(count)=q_temp(1);
movaghat2(count)=q_temp2;

C=zeros(node-1,1);

for i=2 : h+r
    C(:,1)=Temp(:,i-1);
    qq=((2*q_temp1*delx*F0)/k);
    C(1,1)=C(1,1)+qq;
    C(node-1,1)=C(node-1,1)+TC_boundary(i)*F0;

    Temp(:,i)=A_inv*C;
end;

for i=2 : h+r

    C(:,1)=Temp2(:,i-1);
    qq=((2*q_temp2*delx*F0)/k);
    C(1,1)=C(1,1)+qq;
```

```
    C(node-1,1)=C(node-1,1)+TC_boundary(i)*F0;

    Temp2(:,i)=A_inv*C;
end;

error=0;
G=0;
for i=1 : r
%=================Calculatin sensitivity coefficient================
    fi(i)=(Temp2(3,i+h-1)-Temp(3,i+h-1) )/(epsilon*q_temp1);
    error=((TC1(i+h-1)-Temp(3,i+h-1))*fi(i))+error;
    G=fi(i)^2+G;
end;
%=================Calqulating delq ================================
delq= error/G;
movaghat3(count)=delq;
q_error= delq/q_temp(1);
q_temp1=q_temp1+delq;
%================= checking the error ==============================

end;
Temp_chill(h)=Temp(1,h);
q(h,1)=q_temp1;

end;

%================ Calculation of interface temperature at casting side

for i=1 : t-r
    T_casting(i)=((-q(i)*x3)/(k_casting))+Termocouple_casting(i);
end;

%================ Heat transfer Coefficient ===============
h=0;

for i=1 : t-r

    h(i)=q(i)/(T_casting(i)-Temp_chill(i));
end;

%================= del q ==========

 figure(1)
 hold on;
 plot(time(:),q(:),'-o','LineWidth',1.1,...
```

```
                'Color','b',...
                'MarkerEdgeColor','b',...
                'MarkerFaceColor',[0.803921569  0.784313725
0.694117647],...
                'MarkerSize',1)

plot(X(2),b(1),'-o','LineWidth',1.5,...
                'Color','red',...
                'MarkerEdgeColor','k',...
                'MarkerFaceColor',[0.803921569  0.784313725
0.694117647],...
                'MarkerSize',3)

 Tt=Tt1;
 Tt(node,1)=TC2(1);
 Tt1=(A*Tt)+q;
 q(node,1)=TC2(3);

 figure(1)
 hold on;
 plot(X(:),Tt1(:),'-o','LineWidth',1.5,...
                'Color','red',...
                'MarkerEdgeColor','k',...
                'MarkerFaceColor',[0.803921569  0.784313725
0.694117647],...
                'MarkerSize',3)

plot(X(2),b(1),'-o','LineWidth',1.5,...
                'Color','red',...
                'MarkerEdgeColor','k',...
                'MarkerFaceColor',[0.803921569  0.784313725
0.694117647],...
                'MarkerSize',3)

C=zeros(node-1,1);
error=0;
    for i=h+1 : 10+h
                C(:,1)=Temp(:,i-1);
                qq=((2*Q*delx*F0)/k);
                C(1,1)=C(1,1)+qq;
                C(node-1,1)=C(node-1,1)+TC_boundary(i)*F0;

                Temp(:,i)=A_inv*C;
    end;
    for j=1+h : r+2+h
```

```
        %==================Calculatin sensitivity
coefficient================
        error=((TC1(h+1)-Temp(5,j))^2)+error;

    end;
```